



Run Run Shaw Library

香港城市大學  
City University of Hong Kong

### **Copyright Warning**

Use of this thesis/dissertation/project is for the purpose of private study or scholarly research only. ***Users must comply with the Copyright Ordinance.***

Anyone who consults this thesis/dissertation/project is understood to recognise that its copyright rests with its author and that no part of it may be reproduced without the author's prior written consent.

CITY UNIVERSITY OF HONG KONG  
香港城市大學

Seasonal Prediction of Summertime Rainfall in South  
China using Multi-Model Ensemble Products

利用多模式集合數據於華南地區作夏季降雨預測

Submitted to  
School of Energy and Environment  
能源及環境學院  
in Partial Fulfillment of the Requirements  
for the Degree of Master of Philosophy  
哲學碩士學位

by

Tung Ying Lut  
董應律

August 2013  
二零一三年八月

## **Abstract**

General circulation model (GCM)-based dynamical forecast systems are commonly used for seasonal predictions. Some large-scale dynamical variables such as the mean sea level pressure, upper air temperature, zonal wind, etc., are well predicted. However, GCMs show very low skills in predicting some variables such as the local-scale precipitation. In order to interpolate the large-scale climate information from GCMs to the regional scale, downscaling techniques based on either dynamical or statistical models need to be used.

This research addresses this issue by using statistical schemes to downscale GCM-based seasonal forecast outputs for local-scale rainfall prediction over South China (SC) in boreal summer. Hindcast experiments from 11 global models and their multi-model ensemble (MME) average were considered. Singular value decomposition analysis based on observed data showed that the precipitation variation over SC is strongly related to that in the mean sea level pressure (SLP) over Southeast Asia, the western north Pacific and Indian Oceans. Hence, SLP was chosen as the predictor for predicting the SC station-scale rainfall variations.

A statistical downscaling scheme based on the “perfect prognosis” approach (PP), was first developed and evaluated. Based on the relationship between the observed SLP and observed station-scale precipitation using SVD analysis, a statistical scheme was constructed. Station-scale precipitation is then

predicted by replacing observations with model outputs for SLP, in the precipitation SVD reconstruction. Downscaling based on hindcast data of SLP from 11 GCMs and their MME average indicated that PP-based downscaling has difficulties in improving the rainfall prediction in central SC. In general, rainfall prediction based on PP downscaling outperforms the direct model output (DMO) at western SC for most model except BCC and NCEP. The exceptional models show improvement in eastern SC. However, the improvement of the PP-based downscaling is limited since the scheme is unable to correct systematic biases of GCMs.

A similar SVD analysis was then repeated to obtain a statistical relationship between model SLP and the observed station precipitation. Results showed that there is also strong covariability between model hindcast SLP and observed station precipitation. Hence another downscaling approach, namely model output statistics (MOS), was adopted for predicting the SC station-interpolated precipitation with model SLP as predictors.

Compared with DMO, the improvement of rainfall prediction based on the MOS-type downscaling is limited in two distinct geographical locations. For first group of models (labelled as Type 1), improvement is mainly found in western SC near Guangxi. For second group of models (labelled as Type 2), improvement is mainly seen in the eastern coastal area. Further analysis revealed that dynamical models have difficulties in capturing the regional circulation details in SLP over SC, leading to erroneous prediction in some locations. The statistical method is able to map the large-scale circulation patterns to station-

scale rainfall variations, thereby correcting some of the biases over land. To conclude, statistical downscaling helps to increase the prediction skill where DMO performs poorly.

### **Acknowledgements**

I would like to express my heartfelt gratitude to my supervisor, Dr Francis Tam, for his kind guidance, continuous support and enlightening suggestions. This dissertation could not have been written so soon without his patient by spending lots of time with me. Thanks are extended to Prof. Jonny Chan and Dr. Wen Zhou for providing me constructive criticisms and insightful feedbacks.

I greatly enjoy doing my research in School of Energy and Environment (SEE). I am very grateful to have met Mr. Ray Lee, Mr. Christopher Holst, Mr. Kunhui Ye, Ms. Glory Kwok, and Ms. Andie Au-yeung in our group meetings to exchange the opinion about my work. Thanks are also given to Mr. Kin Sik Liu, Mr. Kelvin Chan, Mr. Koon Chuen Szeto, Mr. Hoffman Cheung, Mr. Richard Li, Mr. Eric Chow, Mr. Marco Leung, Mr. Weiwen Wang, Ms. Xiuzhen Li, Mr. Chung Sing Lai, Dr. Judy Huang, Ms. Camilla Cheng, Mr. Samson Chiu, and Ms. Kit Ying Fung for their kindness and help at different stages of my work and study. Administrative work by Ms. Ada Au, Ms. Katie Chan, Ms. Michelle Wong, Ms. Po Ming Lee, Ms. Yee Ting Lee, Ms. Ming Wai Yu, Chu, Ms. Alice Wong of SEE and Ms. Stephanie Chan of School of Graduate Studies are much appreciated.

Throughout my study, I am also benefited from valuable comments by Dr. Micheal Leung, Dr. Wey Yang Teoh, Dr. Nicky Lam, Dr. Carol Lin, Dr. Patrick Lee, and Dr. Kenneth Chu of City University of Hong Kong. Discussions

with Dr. Soo-Jin Sohn, Dr. Jung-Lien Chu are constructive for improving my work. The author is a recipient of Research Studentship provided by the City University of Hong Kong. This dissertation is dedicated to my family and Ms. Pammy Li. I am indebted to my parents, friends for their encouragement and understanding.

## Table of Contents

<b>Table of Contents .....</b>	<b>vi</b>
<b>List of Acronyms .....</b>	<b>viii</b>
<b>List of Tables .....</b>	<b>x</b>
<b>List of Figures.....</b>	<b>xi</b>
<b>Chapter 1    Introduction .....</b>	<b>1</b>
1.1      Background .....	1
1.2      Objectives .....	3
1.3      Overview of thesis chapters .....	4
<b>Chapter 2    Literature review.....</b>	<b>5</b>
2.1      Overview of the SC rainfall variability .....	5
2.2      Seasonal predictions using GCMs.....	12
2.3      Multi-Model Ensemble (MME) for seasonal predictions .....	14
2.4      Overview of downscaling.....	14
2.5      Predictors for prediction .....	20
2.6      Research motivations .....	20
<b>Chapter 3    Observations and model data.....</b>	<b>22</b>
3.1      Study period and observational global datasets .....	22
3.2      Experiments based on model hindcast data.....	23
3.3      Station rainfall data .....	25
3.4      Linear trend .....	26
3.5      Spatial interpolation of model rainfall output .....	27

<b>Chapter 4</b>	<b>Methodology .....</b>	<b>29</b>
4.1	Empirical orthogonal function analysis .....	30
4.2	Statistical downscaling approach.....	31
4.3	“Leave-one-out” cross validation .....	32
<b>Chapter 5</b>	<b>Spacetime Characteristics of SC summer rainfall variability</b>	<b>33</b>
5.1	EOF analysis of SC rainfall variability .....	33
5.2	Anomalous large-scale circulation associated with the leading EOFs based on linear regression .....	37
5.3	Composite circulation anomalies based on EOF analysis .....	41
5.4	Anomalous moisture flux divergence and wind divergence.....	43
5.5	SVD analysis based on station rainfall and SLP/Z500. ....	47
5.5.1	SLP.....	48
5.5.2	Z500 .....	55
5.6	The impact of EOF truncation .....	60
<b>Chapter 6</b>	<b>SC rainfall prediction based on direct model output and statistical downscaling .....</b>	<b>62</b>
6.1	SC rainfall predictions based on direct model output .....	63
6.2	Prediction based on statistical downscaling (PP).....	65
6.3	SVD analysis based on observed SC rainfall and model SLP. ....	71
6.4	Predictions based on statistical downscaling (MOS) .....	83
6.5	Improvement in seasonal rainfall variation prediction .....	87
<b>Chapter 7</b>	<b>Summary and discussions .....</b>	<b>98</b>
<b>Bibliography.....</b>		<b>105</b>

**List of Acronyms**

<b>AMIP-II</b>	<b>Atmospheric Model Intercomparison Project</b>
<b>APCC</b>	<b>Asia-Pacific Economic Cooperation Climate Center</b>
<b>APEC</b>	<b>Asia-Pacific Economic Cooperation</b>
<b>AO</b>	<b>Arctic Oscillation</b>
<b>BCC</b>	<b>Beijing Climate Center</b>
<b>BMRC</b>	<b>Bureau of Meteorological Research Centre</b>
<b>CFS</b>	<b>NCEP Coupled Forecast System</b>
<b>CMAP</b>	<b>Climate Prediction Center Merged Analysis of Precipitation</b>
<b>CPC</b>	<b>Climate Prediction Center</b>
<b>CWB</b>	<b>Central Weather Bureau</b>
<b>DEMETER</b>	<b>Development of a European multi-model ensemble system for seasonal</b>
<b>DMI</b>	<b>Dipole mode index</b>
<b>DMO</b>	<b>Direct model output</b>
<b>EASM</b>	<b>East Asian summer monsoon</b>
<b>ENSO</b>	<b>El Niño/Southern Oscillation</b>
<b>EOF</b>	<b>Empirical orthogonal functions</b>
<b>GCM</b>	<b>General circulation models</b>
<b>GCPS</b>	<b>Global Climate Prediction System</b>
<b>GDAPS</b>	<b>Global Data Assimilation and Prediction System</b>
<b>GDP</b>	<b>Gross domestic product</b>
<b>IOD</b>	<b>Indian Ocean dipole</b>
<b>JJA</b>	<b>June, July and August</b>
<b>KMA</b>	<b>Korea Meteorological Administration</b>
<b>MCA</b>	<b>Maximum covariance analysis</b>
<b>METRI AGCM</b>	<b>Meteorological Research Institute Atmospheric General Circulation Model</b>
<b>MME</b>	<b>Multi-model ensembles</b>
<b>MSC</b>	<b>Meteorological Service of Canada</b>

<b>MSC-GM2</b>	Meteorological Service of Canada – second generation general circulation model
<b>MSC-GM3</b>	Meteorological Service of Canada – third generation general circulation model
<b>MSC-SEF</b>	Meteorological Service of Canada – multilevel spectral primitive-equations model
<b>MOS</b>	<b>Model output statistics</b>
<b>NCAR</b>	National Center for Atmospheric Research
<b>NCEP</b>	National Centers for Environment Prediction
<b>NCEP-DOE</b>	National Centers for Environmental Prediction – Department of Energy
<b>NIMR</b>	Nation Institute of Meteorological Research
<b>PC</b>	Principal components
<b>PMME</b>	Operational Multi-model ensembles prediction system
<b>PNU</b>	Pusan National University
<b>POAMA</b>	Predictive ocean-atmosphere model for Australia
<b>PP</b>	Perfect prognosis
<b>SC</b>	South China
<b>SCS</b>	South China Sea
<b>SLP</b>	Sea level pressure
<b>SMIP/HFP</b>	Seasonal Model Intercomparison Project / Historical Forecast Project SST Sea surface temperature
<b>SNU</b>	Seoul National University
<b>SSTA</b>	Sea surface temperature anomaly
<b>SVD</b>	Singular value decomposition
<b>WNPMI</b>	Western north Pacific monsoon index
<b>WNPSM</b>	Western north Pacific summer monsoon
<b>Z500</b>	Geopotential height at 500hPa

**List of Tables**

<b>Table 3-1.</b>	<b>Description of the model hindcast experiments used in this study.....</b>	<b>23</b>
<b>Table 5-1.</b>	<b>Correlation coefficient between time expansion coefficient of the leading SVD modes and climate indices for (a) rainfall and (b) SLP.....</b>	<b>53</b>
<b>Table 5-2.</b>	<b>Same as Table 5-1 except for Z500.....</b>	<b>58</b>
<b>Table 6-1.</b>	<b>Summary of the Type 1 and Type 2 model.....</b>	<b>87</b>

List of Figures

<b>Figure 2-1.</b>	Composite difference of summer rainfall (1979-1996) between strong and weak monsoon year respect to the WNPMI. Shading denotes region of difference at 95% confidence level. (From Wang et al., 2001) .....	8
<b>Figure 2-2.</b>	Schematic diagrams showing the major circulation anomalies associated with a stong WNPSM. The lower-level (upper-level) circulation anomalies are denoted by solid (dashed) lines. (From Wang et al., 2001) .....	8
<b>Figure 2-3.</b>	Circulation patterns at 850hPa in JJA over South Asia during positive IOD. (From Li and Mu, 2001) .....	10
<b>Figure 2-4.</b>	Schematic diagram of the effects of boundary condition anomalies on large-scale atmospheric circulation. (From Shukla and Kinter 2006) .....	12
<b>Figure 2-5.</b>	Conceptualization of downscaling of GCM products. (Ed Maurer, 2009) .....	15
<b>Figure 2-6.</b>	Leading SVD mode spatial patterns of (a) the observed station precipitation in northern Taiwan and (b) the observed Z500 in East Asia during JJA. (c) Normalized expansion coefficients corresponding to precipitation and Z500. Leading SVD mode spatial patterns of (a) the observed station precipitation in northern Taiwan and (b) the observed SLP in East Asia during JJA. (c) Normalized expansion coefficients corresponding to precipitation and SLP. (From Chu et al., 2008).....	19
<b>Figure 3-1.</b>	Geographical locations of the 89 stations in SC.....	26

<b>Figure 3-2.</b>	An example illustrating the variability of SC rainfall. (a) The original anomalous rainfall for a particular station. (b) Same as (a) except with the linear trend removed. ....	27
<b>Figure 4-1.</b>	Flowchart of the research procedure. ....	30
<b>Figure 5-1.</b>	Station precipitation (without units; normalized their corresponding square root of eigenvalue) corresponding to the (a) 1 <sup>st</sup> , (b) 2 <sup>nd</sup> and (c) 3 <sup>rd</sup> leading EOF. Upper right shows the percentage of explained variance for each EOF.....	34
<b>Figure 5-2.</b>	Normalized PC time series for (a) 1 <sup>st</sup> , (b) 2 <sup>nd</sup> and (c) 3 <sup>rd</sup> EOF mode. ....	36
<b>Figure 5-3.</b>	Regression of (a) 850hPa wind (see scale arrow in upper right; units: $\text{ms}^{-1}$ ) and SLP (contours in interval of 0.05 hPa, with negative values denoted by dashed lines), and (b) Z500 (contours in interval of 0.01 hPa), based on the leading normalized PC time series of SC rainfall. Shading (arrows) denotes either SLP (850 wind) or Z500 signals significant at the 90% level. ....	37
<b>Figure 5-4.</b>	Same as Figure 5-3 except for regression based on PC2.....	39
<b>Figure 5-5.</b>	Same as Figure 5-3 except for regression based on PC3.....	40
<b>Figure 5-6.</b>	Composite maps for (a) SLP (contours in interval of 10 hPa) and (b) Z500 (contours in interval of 2.5 hPa) of the 2 <sup>nd</sup> EOF. Shading denotes SLP and Z500 signals significant at the 90% level.....	42
<b>Figure 5-7.</b>	Regression map of moisture flux divergent component (arrows) and its divergence (shading) based on (a) PC1, (b) PC2 and (c) PC3. ....	45

<b>Figure 5-8.</b> The dimensionless leading singular vector for (a) observed station precipitation and (b) SLP from observations based on SVD analysis. The fraction of squared covariance between two field explained by the leading mode is shown on upper right. (c) Normalized time series of the expansion coefficient for precipitation (solid line), SLP (dashed line). Upper left shows the correlation coefficient between SLP and SC rainfall.	48
<b>Figure 5-9.</b> Same as Figure 5-8, except for the 2 <sup>nd</sup> singular vector.....	50
<b>Figure 5-10.</b> Same as Figure 5-8, except for the 3 <sup>rd</sup> singular vector.....	52
<b>Figure 5-11.</b> Same as Figure 5-8, except based on Z500 from observations.	
.....	55
<b>Figure 5-12.</b> Same as Figure 5-11, except for the 2 <sup>nd</sup> singular vector.....	57
<b>Figure 5-14.</b> The dimensionless leading singular vector for (a) station precipitation and (b) SLP based on SVD analysis with EOF truncation.....	60
<b>Figure 6-1.</b> Correlation coefficients between the JJA precipitation (exceeded 90% significance level) at station locations based on observations and the interpolated DMO of precipitation from (a) BCC (b) CWB (c) GCPS (d) GDAPS (e) MSC-GM2 (f) MSC-GM3 (g) MSC-SEF (h) NCEP (i) NIMR (j) PNU (k) POAMA, and (l) the MME average. The correlation coefficient averaged over all stations is provided in the bottom right corner.	63
<b>Figure 6-2.</b> Same as Figure 6-1, except for predictions based on PP-type statistical downscaling.....	67
<b>Figure 6-3.</b> Difference between Figures 6-1 and 6-2. ....	69

- Figure 6-4.** The leading singular vector for precipitation, based on SVD analysis between observed station precipitation and model SLP from (a) BCC, (b) CWB, (c) GCPS, (d) GDAPS, (e) MSC-GM2, (f) MSC-GM3, (g) MSC-SEF, (h) NCEP, (i) NIMR, (j) PNU, (k) POAMA, and (l) the MME average. Upper right of each panel shows the fraction of squared covariance between station precipitation and model SLP explained by this SVD mode. .... 72
- Figure 6-5.** Same as Figure 6-4 except for singular vectors for model SLP. .... 73
- Figure 6-6.** Normalized time series of the expansion coefficient for precipitation (solid line) and model SLP (dashed line) from (a) BCC, (b) CWB, (c) GCPS, (d) GDAPS, (e) MSC-GM2, (f) MSC-GM3, (g) MSC-SEF, (h) NCEP, (i) NIMR, (j) PNU, (k) POAMA, and (l) the MME average, corresponding to the leading SVD mode. Upper right of each panel shows the correlation between the two time series. .... 75
- Figure 6-7.** Same as Figure 6-4, except for the 2<sup>nd</sup> SVD mode. .... 76
- Figure 6-8.** Same as Figure 6-5, except for the 2<sup>nd</sup> SVD mode. .... 77
- Figure 6-9.** Same as Figure 6-6, except for the 2<sup>nd</sup> SVD mode. .... 78
- Figure 6-10.** Same as Figure 6-4, except for the 3<sup>rd</sup> SVD mode.... 79
- Figure 6-11.** Same as Figure 6-5, except for the 3<sup>rd</sup> SVD mode..... 80
- Figure 6-12.** Same as Figure 6-6, except for the 3<sup>rd</sup> SVD mode..... 81
- Figure 6-13.** Same as Figure 6-1 except for predictions based on MOS-type statistical downscaling. .... 83

<b>Figure 6-14.</b> Difference between Figures 6-1 and 6-13.....	85
<b>Figure 6-15.</b> Difference between the temporal correlation coefficients (a,b) and the MSSS (c,d) for DMO and MOS-type downscaled precipitation for Type 1, and Type 2 model ensemble average, respectively.....	88
<b>Figure 6-16.</b> Geographical locations of the selected stations comprising Zone 1 (squares) and Zone 2 (triangles).....	89
<b>Figure 6-17.</b> Correlation coefficient for precipitation prediction average over (a) Zone 1, and (b) Zone 2, for different models, the MME average as well as Type 1 and Type 2 ensemble averages based on DMO (blue) and MOS-type statistical downscaling (red).....	90
<b>Figure 6-18.</b> Regression coefficients of the JJA mean (a,b) rainfall (units: mm/day), and (c,d) SLP (contours, in interval of 0.05 hPa) from (a,c) observations and (b,d) Type 1 model ensemble average based on the leading PC of the observed SC station rainfall .....	92
<b>Figure 6-19.</b> Same as Figure 6-16, except for the second PC.....	94
<b>Figure 6-20.</b> Same as Figure 6-16 except for regression coefficients based on the third PC for the observations and the Type 2 model ensemble average.....	96

## Chapter 1

### Introduction

#### **1.1 Background**

South China (SC) is one of the regions with the fastest economic growth in China. Its total gross domestic product (GDP) per capital has increased by 160% to US\$14000 in the past 15 years<sup>1</sup>. In addition, SC is facing a population explosion due to its fast development. However, its economy can be greatly affected by the occurrence of floods and droughts which can cause serious disasters. Since summer is the rain season for SC, predicting the summer precipitation is therefore of particular importance. If the summer precipitation can be well predicted, say a season ahead, a number of measures to remedy the loss due to floods or droughts can be prepared in advance.

General circulation models (GCMs) are numerical models that use a set of mathematical equations for simulating the Earth's climate. Nowadays, GCMs are widely applied for seasonal predictions. It is commonly accepted that the source of predictability is from the lower boundary of the atmosphere (i.e., conditions at the Earth's surface). In particular, the lower boundary conditions vary in a much slower rate compared to the day-to-day variations of weather, and can cause a persistent influence on the large-scale atmospheric circulation. Therefore, the large-scale atmospheric variables averaged over time can be predictable to a certain extent. Although GCMs can well simulate large-scale variables such as the sea level pressure, geopotential, etc., (air-sea-coupled

---

<sup>1</sup> Estimation based on data from the NBS China Statistical DataBase.

GCMs can also reproduce atmosphere-ocean coupled variability of the climate system), some variables such as rainfall, especially that over land, are difficult to capture. This is especially the case in monsoon regions, because of the complexity of the monsoon system. Also, local land-sea contrasts and topography are not fully represented in low-resolution models. Hence, obtaining accurate rainfall predictions from dynamical seasonal forecast systems in the monsoon region is still a big challenge.

In view of the relatively low spatial resolution of GCMs adopted for seasonal forecasts, some other methods are needed to enhance the resolution and accuracy of model products. Downscaling refers to methods to interpolate the large-scale climate information from GCMs onto the regional scale. Generally, there are two types of downscaling methods: dynamical downscaling and statistical downscaling. In dynamical downscaling, high-resolution simulations are obtained by using a regional climate model, which is driven by large-scale variables from GCMs (Giorgi et al., 1990; Mearns et al., 1995). The cost of improving the spatial resolution of prediction products, however, is the large computational demand for running a regional model using this method. Statistical downscaling, on the other hand, is commonly used since it requires less computational resources. In this method, the empirical relationship between a local climate variable (the predictand) and GCM outputs is first determined (the predictor) (Zorita and von Storch, 1999; Wilby et al., 2004). Forecasts of the local variable are then produced by projecting predictor values from GCMs based on the corresponding statistical relationship.

## ***1.2 Objectives***

The primary motivation for this study is to understand the predictability of the summertime rainfall over the SC area. In addition, the SC rainfall variability related to various recurrent large-scale circulation patterns in the tropical Indo-Pacific region will also be analyzed. The specific objectives of this study are:

1. To assess the skill of GCMs in predicting the summer rainfall over SC;
2. To develop a statistical downscaling scheme to predict the summer rainfall over SC; and
3. To assess and compare the skill of prediction results based on different statistical downscaling approaches.

The results obtained from this study can serve as a background for further studies on seasonal prediction over SC for different seasons and for locations outside SC.

### ***1.3 Overview of thesis chapters***

There are seven chapters in this thesis. Chapter 1 gives an introduction of this research. In Chapter 2, a literature review of relevant studies is provided. Data used and methodology are described in Chapter 3 and Chapter 4, respectively. In Chapter 5, rainfall variability in summertime SC is analyzed by using empirical orthogonal functions (EOF), and the possible linkages between SC rainfall and other large-scale circulation patterns are revealed. Chapter 6 describes the results from singular value decomposition (SVD) of station rainfall-large-scale circulation covariability, and gives an assessment of the prediction skill of station-scale rainfall in SC based on direct model outputs. The comparison between direct model outputs and two different statistical downscaling methods for rainfall prediction are presented. Finally, discussions, conclusion and suggestions for future studies can be found in Chapter 7.

## **Chapter 2**

### **Literature review**

SC summer rainfall is affected by many different recurrent climate modes, such as the anomalous western north Pacific summer monsoon (WNPSM) activity, Indian Ocean Dipole (IOD), movement of the subtropical ridge and the El Nino Southern Oscillation (ENSO). This chapter begins with an overview of the SC rainfall variability (section 2.1). Seasonal predictions using different dynamical models and the multi-model ensemble average are given in sections 2.2 and 2.3, respectively. In section 2.4, two different statistical downscaling schemes based on the perfect prognosis (PP) and the model output statistics (MOS) approaches are briefly introduced. Criteria for selecting different predictors for statistical downscaling of rainfall are presented in section 2.5. The last section states the research motivations of this study.

#### ***2.1 Overview of the SC rainfall variability***

Severe floods or droughts often occur in summer over SC. For instance, excessive rainfall occurred in the region during the summer of 1997. In fact, precipitation over SC exhibits complex space-time structures, and its interannual variability can be related to various climate modes recurrent in tropical (such as ENSO, WNPSM and IOD) as well as extratropical locations (e.g., the Arctic Oscillation).

El Nino refers to the warm sea surface temperature anomaly (SSTA) in the equatorial Pacific Ocean, whereas “Southern Oscillation” is the atmospheric component that is tied to El Nino. When ENSO occurs, positive SSTA in the

equatorial Pacific warms the lower troposphere and consequently affects the sea level pressure (SLP), which brings about large-scale circulation anomalies. Trenberth (1997) indicated that ENSO activity can be detected by monitoring SSTA over the ‘‘Nino 3 region’’ of 5°N-5°S, 90°-150°W. Wang (1995) described the El Nino onset and its evolution, and found that anomalous westerlies in the western equatorial Pacific are established in conjunction with the enhancement of the anomalous low-level cyclone over the Philippines Sea in boreal summer. ENSO can cause extreme weather (i.e. floods and droughts) in many regions of the world. In particular, the impact of ENSO on the precipitation in SC has been investigated by a number of researchers. Below-average rainfall over the region was found during the El Nino mature phase (Huang and Wu, 1989; Zhang et al., 1999; Feng and Hu, 2004). Such rainfall anomalies are caused by the intensified western Pacific subtropical high which covers SC (Zhang et al., 1999). In addition to the intensity, the location of the subtropical high is another factor that results in the anomalous rainfall in SC. Huang and Wu (1989) stated that the negative rainfall anomalies are due to the anomalous southward movement of the subtropical high. They also discovered that SSTA is negative in the western tropical Pacific, and convective activities are weak over the South China Sea (SCS) in the developing stage of ENSO in boreal summer.

Negative rainfall anomaly in SC is observed when the East Asian summer monsoon (EASM) intensifies (Zhang et al., 1996; Zhang et al., 1999). Ding et al. (2008) showed that the summer precipitation in SC has increased in recent decades, which can be attributed to the weakening of the EASM. They

also found that when the EASM is weak, stronger moisture convergence is found in the latitudinal range from Yangtze River (30°N) to SCS, supplying more abundant moisture in the region.

WNPSM is an oceanic monsoon driven primarily by the meridional gradients of SST (Murakami and Matsumoto 1994; Li and Wang 2005). WNPSM has three main characteristics: (1) a northwest-southeast oriented monsoon trough with heavy precipitation; (2) low-level southwesterlies; and (3) upper-tropospheric easterlies. Murakami and Matsumoto (1994) defined the western north Pacific region between 10°-20°N from 120° to 150°E as the core domain of the WNPSM. Wang and Lin (2002) further refined the definition of the WNPSM domain based on the onset, peak, and withdraw characters of climatological rainfall over WNPSM region.

Anomalous WNPSM is one major contributor to the summer SC rainfall variability. Wang et al. (2001) indicated that the summer rainfall increases from SC area to north Pacific during strong WNPSM (Figure 2-1). Figure 2-2 shows that the typical strong WNPSM circulation feature: alternative anomalous cyclone and anti-cyclone along 20°N and 35°N respectively, coupled with the increment of summer rainfall in SC area. Wang et al. (2001) also defined a index for WNPSM, namely the Western North Pacific Monsoon Index (WNPMI), which is the difference of 850hPa zonal wind between the southern domain of 5°-15°N, 100°-130°E and the northern domain of 20°-30°N, 110°-140°E. Finally, WNPSM was also found to be associated with ENSO activity. Wang et al. (2001)

discovered that a strong (weak) WNPSM tends to follow the occurrence of the mature phase of cold (warm) ENSO.

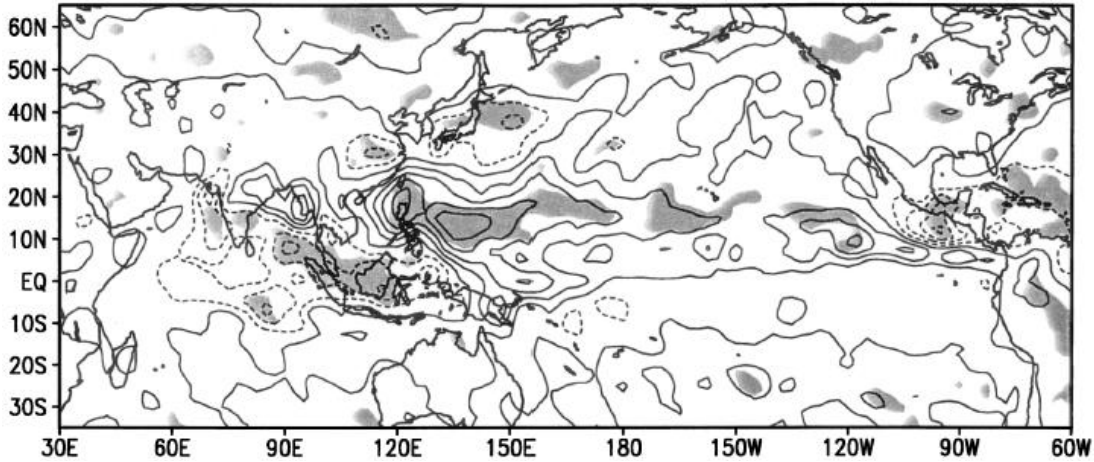


**Figure 2-1.** Composite difference of summer rainfall (1979-1996) between strong and weak monsoon year respect to the WNPMI. Shading denotes region of difference at 95% confidence level. (From Wang et al., 2001)

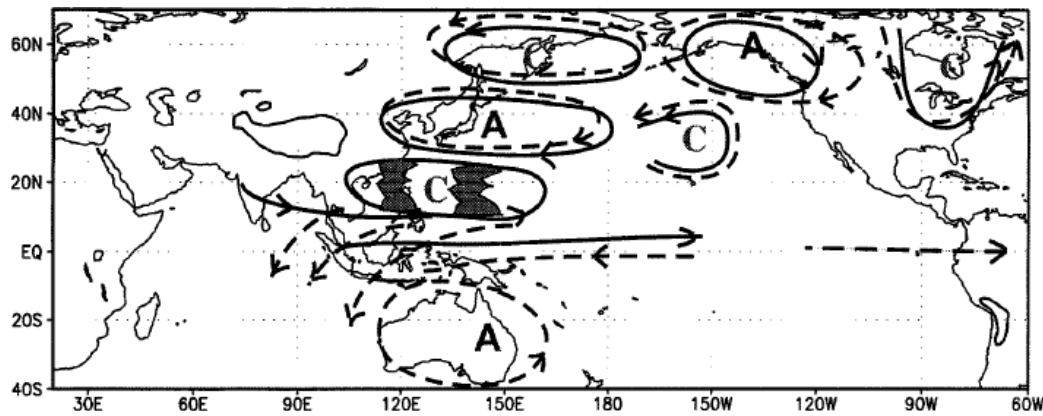


**Figure 2-2.** Schematic diagrams showing the major circulation anomalies associated with a strong WNPSM. The lower-level (upper-level) circulation anomalies are denoted by solid (dashed) lines. (From Wang et al., 2001)

Besides the aforementioned climate activities, those in the Indian Ocean such as IOD can also affect the variability of SC summer rainfall. The feature of IOD is that SSTA is robustly coupled to wind anomaly in the equatorial Indian Ocean (Saji et al., 1999; Saji and Yamagata 2003). IOD activity can be monitored by measuring the difference of SSTA between the western domain of 10S-10N, 50E-70E and the south eastern domain of 10S-0N, 90E-110E over the equatorial Indian Ocean. This difference is called the dipole mode index (DMI). Positive (negative) IOD is identified when the DMI value is positive (negative).

Guan and Yamagata (2003) used the National Centers for Environment Prediction (NCEP) National Center for Atmospheric Research (NCAR) reanalysis data from 1979 to 2001, and the Climate Prediction Center (CPC) Merged Analysis of Precipitation (CMAP) precipitation data from 1979 to 1999 to investigate the unusual summer of 1994 due to IOD events. Their results demonstrated that positive IOD is at least one plausible cause of surplus rainfall in SC, which is consistent with many studies (Xiao et al., 2002; Li and Mu, 2001; Ashok et al., 2001). This rainfall anomaly in SC accompanies an anomalous cyclonic circulation extending westward from the tropical western Pacific to the southern part of China. Xiao et al. (2002) found that the Walker circulation and the Indian summer monsoon tend to be weakened by the anomalous easterly in equatorial Indian Ocean when IOD was positive, while at the same time these features increase the summer precipitation in SC. Xiao et al. (2002) also pointed out that the East Asian trough appears to be weaker and the subtropical ridge extended more southward, leading to more precipitation in SC. Li and Mu (2001)

indicated that SC summer rainfall tends to increase when the anticyclone over the Tibet and the subtropical high are weakened during positive IOD. The typical anomalous circulation pattern at 850hPa during positive IOD in JJA is shown in Figure 2-3. During positive IOD, there is an accompanying anomalous low-level cyclone in SC, which can be conducive to more rainfall in the region. Finally, the Indian Ocean variability associated with ENSO was investigated by Zhong et al. (2005). They studied the causes of SSTA features in the equatorial Indian Ocean consistent with IOD during El Nino. In order to initiate IOD, it seems that ENSO needs to be developed early enough, for example before boreal summer.

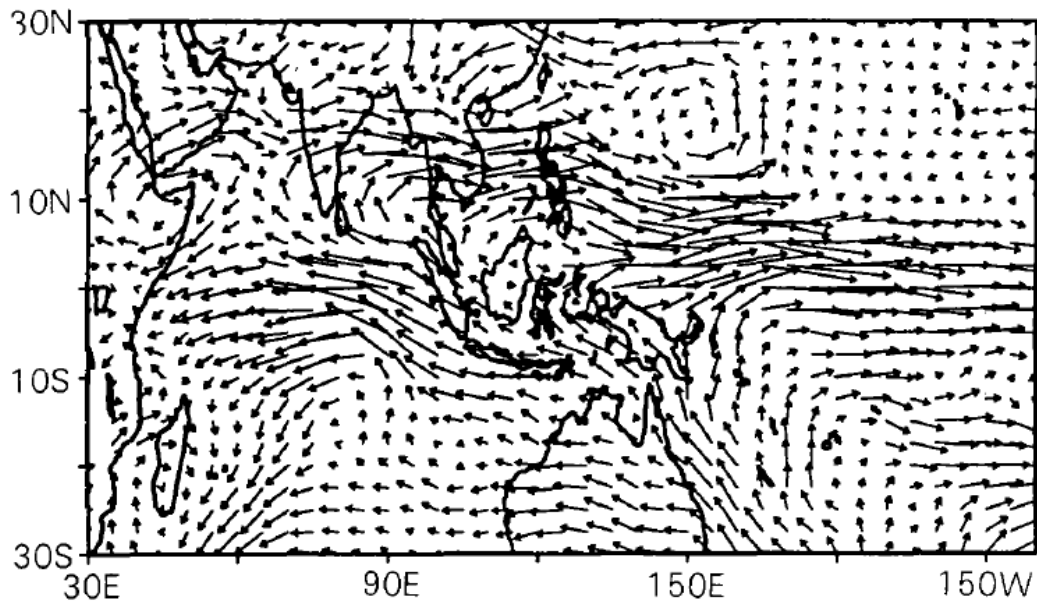


**Figure 2-3. Circulation patterns at 850hPa in JJA over South Asia during positive IOD. (From Li and Mu, 2001)**

The Arctic Oscillation (AO; Thompson and Wallace, 1998), also referred to as the Northern Hemisphere annular mode, is a large-scale mode of climate

variability with strong signatures over the north hemisphere extratropics. AO is characterized by westerlies in the Arctic at around 55°N, and can occur in the positive or negative phases. Positive AO leads to stronger than normal westerly wind that confines colder air in the polar region. In contrast, polar colder air is able to penetrate southward because of weakened westerlies in the negative phase of AO. AO is strongest in winter and it significantly affects mid- to high-latitude climate during the cold season.

Thompson and Wallace (2000) also noted that AO can influence the atmospheric circulation during the warm season as well. In recent years, many studies investigated the impact of AO on the rainfall variability over East Asia. Gong and Ho (2003) discovered a relationship between AO and EASM. They showed AO in May has the strongest connection to the summer rainfall in China. Gong and Ho (2003) also suggested the mechanism connecting the late spring AO activity and the summer rainfall. Gong et al. (2011) further investigated the impact of the connection between the spring AO activity and EASM on the western north Pacific circulation. Anomalous cyclonic circulation at 850 hPa in southeastern Asia and the western North Pacific occurs after the spring AO. The subtropical high is weaken by those anomalous circulations in such areas, leading to positive anomalous rainfall in the region of southern China to western north Pacific.

## 2.2 Seasonal predictions using GCMs

Many studies in the past decades showed that the sense of seasonal predictability lies in lower boundary conditions (e.g. SSTA, heat flux, moisture flux, etc.). Fennelly et al. (1985) conducted a sensitivity experiment to examine the effects of SSTA in the equatorial Pacific. Their results suggested that variations of the seasonal climate are predictable given that anomalies in the lower boundary are properly incorporated.

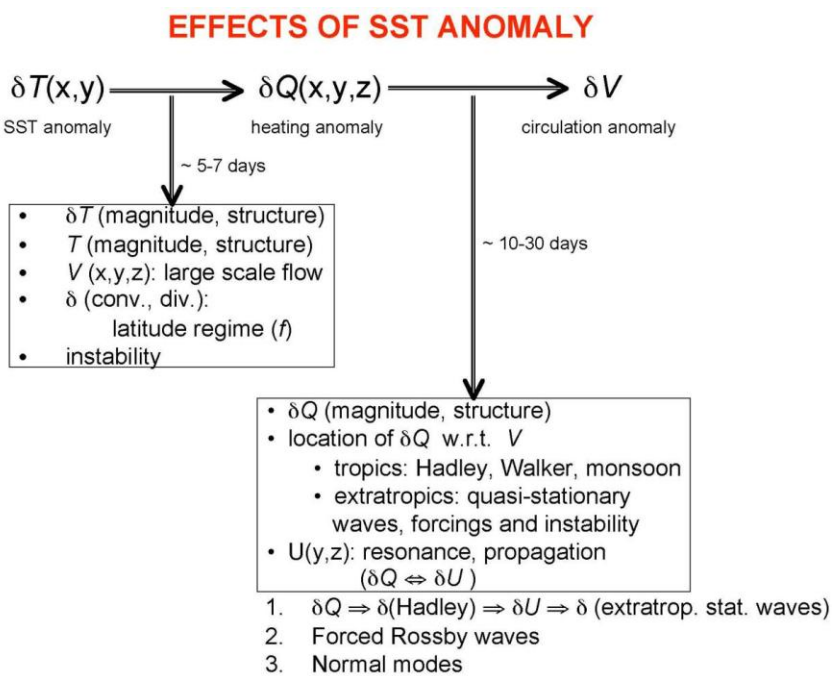


**Figure 2-4. Schematic diagram of the effects of boundary condition anomalies on large-scale atmospheric circulation. (From Shukla and Kinter 2006)**

Figure 2-4 illustrates how the boundary condition (say, SSTA) can affect the large-scale circulation via a complex mechanism. At the beginning, anomalous SST alters the sensible and latent fluxes from ocean to atmosphere,

changing the surface temperature and humidity, and consistently, the surface pressure gradient in the atmosphere. Then the surface pressure gradient changes the low-level atmospheric convergence. When the latter changes, the moisture flux convergence will be affected directly, especially in the tropics. This phenomenon plays a critical role in driving tropical convection, which in turn can affect the large-scale circulation. In other words, the boundary condition is important in driving climate variations. It is widely believed that atmospheric-GCM, with imposed lower boundary conditions, are able to simulate the large-scale atmospheric circulation. One good example is the skilful SLP prediction in the tropical Atlantic and Pacific (Rodwell, 1998).

In contrast, GCMs encounter difficulties in capturing the regional-scale climate signals, especially in the monsoon region. It is because the complexity of the monsoon system makes it hard to have skilful predictions. Kang et al. (2002) evaluated the prediction of summer monsoon rainfall variation from 10 GCMs over the Asian-Western Pacific region. They found that most of the models fail to reproduce the monsoon rainfall in the region from East China Sea to the mid Pacific in summer. Ajayamohan (2007) also found a similar result that GCMs have difficulties in simulating the rainband in SCS and the western north Pacific. Yang et al. (2008) found that the NCEP climate forecast system underestimates the strength of the monsoon circulation in Asian continent. Therefore, modifications of models or other additional post processing of model data (e.g. MME approach and downscaling) would be needed to achieve a more reliable regional-scale circulation prediction.

### **2.3 *Multi-Model Ensemble (MME) for seasonal predictions***

A single-model ensemble prediction is a prediction derived from the average of a number of predictions under different initial conditions using the same model, thus uncertainties in the initial condition are incorporated in the prediction. However, the single-model ensemble does not provide any reduction in the systematic and random component in the model errors (i.e. model dependent uncertainties), hence, the prediction skill is limited. Krishnamurti et al. (1999) and Doblas-Reyes et al. (2000) provided evidence that the prediction skill based on the MME approach is higher than that of individual models because of its taking into account model dependent uncertainties. Nowadays, the MME approach is used for seasonal predictions in a number of operational centers.

The MME hindcast experiment datasets at the Asia-Pacific Economic Cooperation (APEC) Climate Center (APCC) has been developed for seasonal predictions and were used in many studies. Sohn et al. (2011) studied the variability and predictability of East Asian winter climate and assessed the performance of the APCC MME. Min et al. (2009) developed an operational MME prediction system (PMME) based on the APCC MME. It was found that PMME have a skilful prediction in temperature and precipitation in tropics.

### **2.4 *Overview of downscaling***

GCMs often show difficulties in providing a skilful regional-scale simulation due to their coarse resolution. Grotch and McCracken (1991) indicated that erroneous temperature and precipitation predictions in finer spatial scales were produced using GCMs. In order to resolve finer-scale variability,

various methods of downscaling have been developed. Figure 2-5 shows the conceptualization of downscaling of coarse-resolution GCM products. Here, downscaling techniques are necessary to provide high-resolution information of variables such as the local-scale precipitation- which is usually not well-resolved in GCMs.

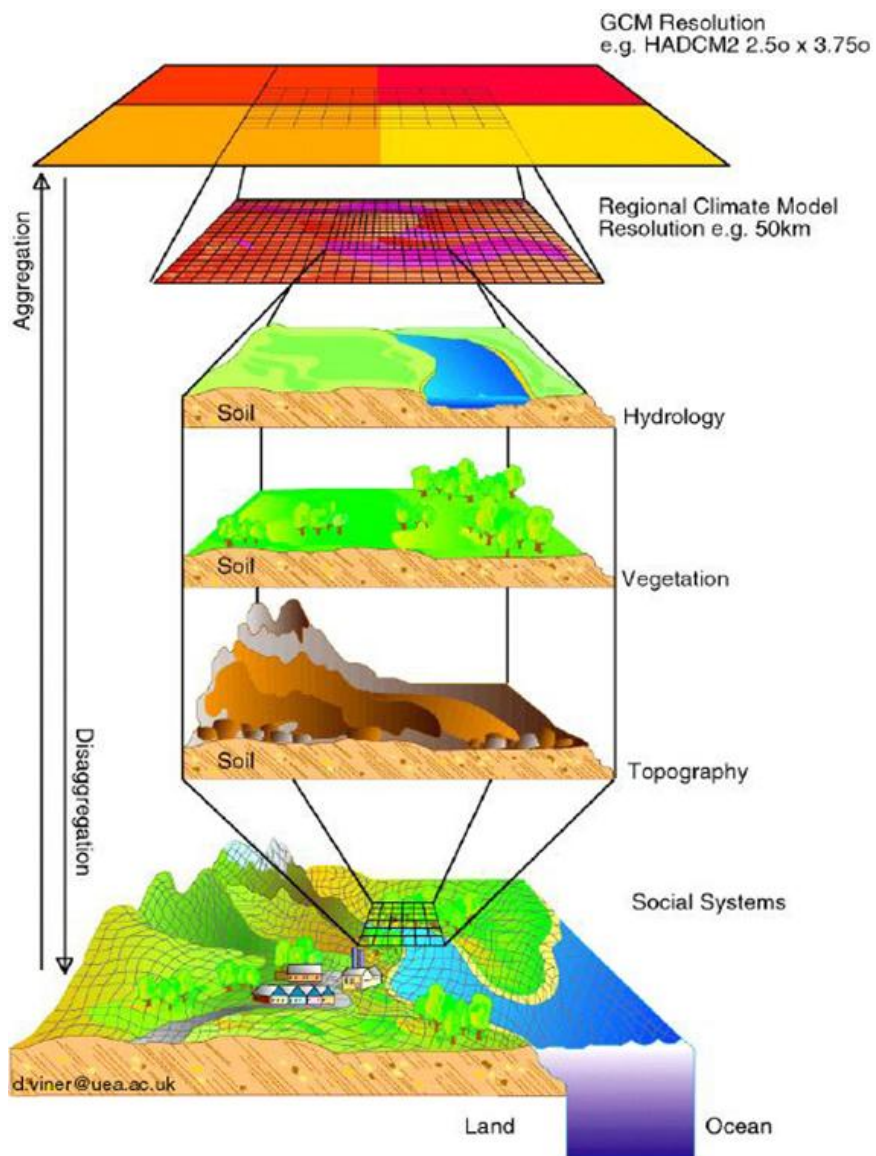


**Figure 2-5. Conceptualization of downscaling of GCM products. (Ed Maurer, 2009)**

Downscaling can be categorized into two major methods: dynamical and statistical. The former involves the use of (nested) limited area models with progressively higher spatial resolution that can account for more of the geographical features than in the GCM (Wilby and Wigley, 1997). The disadvantage of dynamical downscaling is that it requires a lot of storage space and computing resources. Also, this approach requires much time to obtain a higher resolution prediction for each individual model. Therefore, it is less flexibility and not readily transferred to other regions.

Statistical downscaling entails the extraction of information about statistical relationship between the large-scale climate variables and the local climate variables. Compared to the dynamical method, it requires less computational demand for obtaining local-scale information of meteorological variables. Perfect prognostic (PP) and model output statistics (MOS) are developed and commonly used in many studies. In the PP approach, a statistical relationship is developed by using observed large-scale atmospheric parameters (predictor) and observations of the predictand (Klein et al., 1959). Note that this method makes use of (stable) statistical relationships from observations and is independent of the GCM data. Only historical climatological data is used for developing a PP equation (Wilks 1995). Williams (1961) showed that there was a significant improvement of the 2-day forecasts in Utah using the PP statistical downscaling approach, while Shafer and Fuelberg (2008) developed a PP-based statistical downscaling scheme for forecasting warm-season lightning over

Florida. However, the PP scheme assumes a “perfect” forecast of the predictors by GCMs, and any model biases from the GCMs are not considered.

In contrast to PP, in MOS statistical relationships are derived using observed local predictands and outputs for large-scale variables from GCMs. One of the advantages of MOS is that, by construction, the developed statistical downscaling relationship has already taken the model biases into account. This is also the reason why MOS is often preferred for incorporating GCM data into local prediction (Wilks 1995). Maraun et al. (2010) reviewed and evaluated PP as well as MOS. They showed that in MOS biases in the GCM simulations are automatically corrected (see also Widmann et al., 2003). Brunet et al. (1988) also compared PP and MOS in the context of numerical weather forecasts. They concluded that PP (MOS) had higher skill scores for shorter (longer) range prediction.

Both PP and MOS approaches can be applied for other statistical downscaling tools such as regression method and weather pattern (circulation)-based method. Wilby and Wigley (1997) reviewed those statistical downscaling tools. Regression method is the earliest downscaling tool. In general, this tool involves linear or non-linear relationship between large-scale variables and regional-scale predictands. Multiple linear regression is one of the methods to find the regression links between multi-predictors and predictand. This method was employed in Liu et al. (2011). The AO Index (see Thompson and Wallace, 2000), 500hPa geopotential height, 850hPa humidity, and sea surface temperature, with input data taken from the Development of a European Multi-

model Ensemble System for Seasonal to Interannual Prediction (DEMETER) project, are used as the predictors for predicting the southeast China rainfall (Liu et al., 2011). They found that the skill in predicting the summer precipitation in southeast China is increased compared to direct model output.

Weather pattern (circulation)-based downscaling method is also used to identify the physical linkages between observations and large-scale variables. This tool can well simulate large-scale variables from the model and observed precipitation characteristics (Wilby and Wigley, 1997). A number of studies showed this pattern-based downscaling can also be used for rainfall prediction. Chu et al. (2008) investigated the potential of predicting local precipitation over northern Taiwan using downscaling of large-scale circulation variables from GCMs. In their study, the relationships between local precipitation and observed Z500/SLP were first revealed by using SVD analysis. Figure 2-6 gives spatial patterns for the first SVD mode using station precipitation and Z500 as input data, and those using precipitation and SLP. It can be seen that the suppressed rainfall over northern Taiwan is coupled with negative anomalies over Japan and Korea and positive anomalies over Taiwan and SC in both Z500 and SLP. This indicated that there are the physical connections between local rainfall and Z500/SLP. Similar analysis was repeated to reveal the statistical relationships between local precipitation and Z500/SLP from GCMs. These statistical relationships were then used to develop a statistical downscaling scheme for rainfall predictions. The results demonstrated that useful regional climate information can be obtained from downscaling using large-scale variables from

coarse-resolution GCM outputs. Chu and Yu (2010) investigated the use of the SVD method to downscale regional precipitation over Yunlin County in Taiwan. They also noted that precipitation over such area is closely related to the large-scale circulation over the East Asian monsoon region. Wang and Guan (2007) revealed the relationship between rainfall over China and air-sea interactions in the Indian Ocean using SVD analysis.

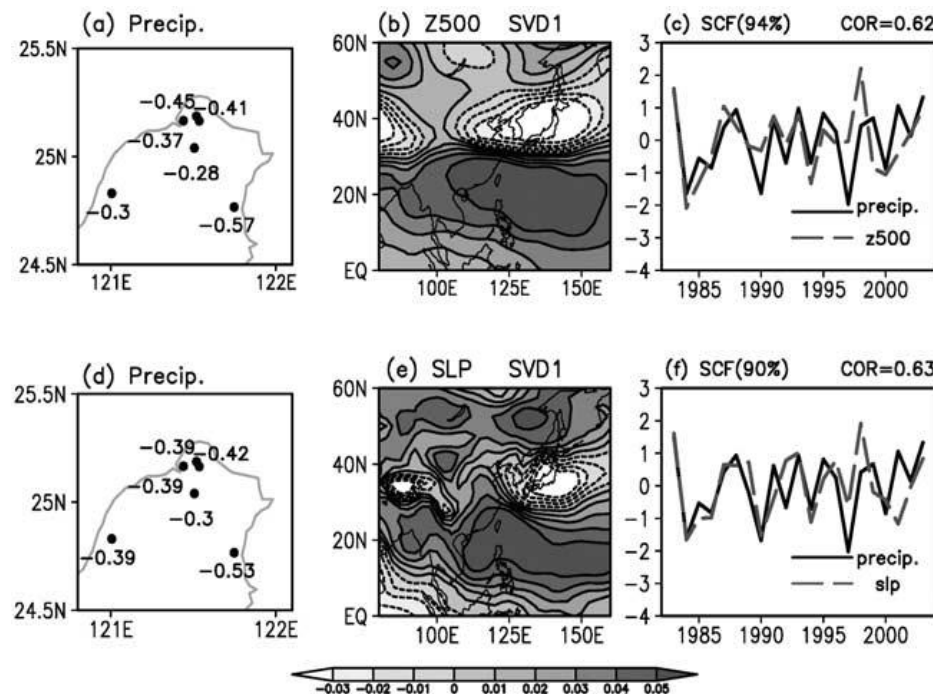


**Figure 2-6. Leading SVD mode spatial patterns of (a) the observed station precipitation in northern Taiwan and (b) the observed Z500 in East Asia during JJA. (c) Normalized expansion coefficients corresponding to precipitation and Z500. Leading SVD mode spatial patterns of (a) the observed station precipitation in northern Taiwan and (b) the observed SLP in East Asia during JJA. (c) Normalized expansion coefficients corresponding to precipitation and SLP. (From Chu et al., 2008)**

## 2.5 *Predictors for prediction*

Several key conditions need to be satisfied in order for a variable to be chosen as predictor. Two of them are presented here. First, the predictors should be well reproduced by GCMs so that it can be used for statistical downscaling (Wilby et al., 2004). The second condition is that the relationship between the predictors and predictands should remain stable. Cavazos (1999) and Wetterhall et al. (2005) used SLP as a predictor and found that the prediction skill of the seasonal mean precipitation was enhanced using statistical downscaling. Zhu et al. (2008) used Z500 to develop a statistical scheme to predict the summer rainfall anomaly in Asia-Pacific region. This downscaling scheme is found to have potential for improving the forecast skill of precipitation in SCS. Referring to Chu et al. (2008), the seasonal rainfall prediction was more stable and skilful when using the averaged of Z500- and SLP-based downscaling predictions. Besides SLP and Z500, other predictors were also used for predicting the local-scale rainfall, such as the relative vorticity (Wilby et al., 1998) or even precipitation itself (Widmann et al., 2003) from coarse-resolution models.

## 2.6 *Research motivations*

Many previous studies have indicated linkages between SC rainfall variability and various anomalous climate activities such as ENSO, WNPSM, IOD and even EASM. Studying these linkages between SC rainfall variability and the different anomalous climate activities are important for explaining how these activities affecting SC rainfall. It also helps to understand the origin of anomalous rainfall variability in SC.

In many studies, it was suggested that the statistical downscaling may enhance the seasonal prediction using data from GCMs. Chu et al. (2008) found that useful climate information could be obtained from statistical downscaling using the large-scale variables from coarse-resolution GCM products. These findings motivate this study for developing a statistical scheme to predict the summertime rainfall in SC using MME products. Moreover, we will assess and compare the prediction skill based on MOS and PP and try to indicate the limitations of statistical downscaling.

## **Chapter 3**

### **Observations and model data**

This chapter mainly describes the data sets being used for this study. It begins with the study period and describes the observational global datasets in section 3.1. After that, descriptions about GCM hindcast data and station data are given in sections 3.2 and 3.3, respectively. The method of removing the potential impacts of decadal change is described in section 3.4. Finally, the spatial interpolation method is delineated in section 3.5, which was applied for comparison between results based on direct model output (DMO) and various statistical downscaling methods.

#### ***3.1 Study period and observational global datasets***

The study period includes 21 June-July-August (JJA) seasons from 1983 to 2003. National Centers for Environmental Prediction – Department of Energy (NCEP-DOE) Atmospheric Model Intercomparison Project (AMIP-II)  $2.5^{\circ}$  latitude by  $2.5^{\circ}$  longitude gridded reanalysis datasets within this period were considered (R-2; Kanamitsu et al., 2002). The gridded mean sea-level pressure, geopotential height at 500 hPa (Z500) and wind 850hPa were used as observational data in this study.

### 3.2 Experiments based on model hindcast data

Institute	Model	Resolution	Ensemble Size	Experimental Type	Reference
Bureau of Meteorological Research Centre (BMRC)	Predictive Ocean-Atmosphere Model for Aus.(POAMA)	T47 L17	10	CMIP	<i>Zhong et al.</i> [2005]
Meteorological Service of Canada (MSC)	MSC-GM2	T32 L10	10	SMIP/HFP	<i>McFarlane et al.</i> [1992]
Meteorological Service of Canada (MSC)	MSC-GM3	T63 L32	10	SMIP/HFP	<i>Scinocca et al.</i> [2008]
Meteorological Service of Canada (MSC)	MSC Spectral Primitive Eqt. Model (MSC-SEF)	T95 L27	10	SMIP/HFP	<i>Ritchie</i> [1991]
Beijing Climate Center (BCC)	BCC CGCM	T63 L16	8	CMIP	<i>Ding et al.</i> [2000]
Korean Meteorological Administration (KMA)	Global Data Assimilation and Prediction system (GDAPS)	T106 L21	20	SMIP/HFP	<i>Park et al.</i> [2002]
National Institute of Meteorological Research (NIMR)	Meteorological Research Institute AGCM	5°x4°L17	10	SMIP/HFP	<i>Back et al.</i> [2002]
Pusan National University (PNU)	PNU CGCM	T42 L18	5	CMIP	<i>Sun and Ahn</i> [2011]
Seoul National University	Global Climate Prediction System (GCPS)	T63 L21	12	SMIP/HFP	<i>Kang et al.</i> [2004]
Central Weather Bureau (CWB)	CWB AGCM	T42 L18	10	SMIP/HFP	<i>Liou et al.</i> [1997]
National Centers for Environmental Prediction (NCEP)	NCEP Climate Forecast System (CFS)	T62 L64	15	CMIP	<i>Saha et al.</i> [2006]

**Table 3-1. Description of the model hindcast experiments used in this study.**

The models that are examined are the 11 climate models participating in the Asia-Pacific Economic Cooperation (APEC) Climate Center (APCC) multi-model ensemble (MME) seasonal forecasting. Table 3-1 gives a description of the hindcast experiments. The experimental types are those consistent with the Seasonal Model Intercomparison Project/Historical Forecast Project (SMIP/HFP) or the Coupled Model Intercomparison Project (CMIP). The former type of historical forecasts include those from the Canadian Climate Centre second (McFarland et al., 1992) and third generation general circulation models (Scinocca et al., 2008), and also the multilevel spectral primitive-equations model (Ritchie, 1991) of the Meteorological Service of Canada (MSC), the Global Data Assimilation and Prediction System (GDAPS) of the Korea Meteorological Administration (KMA) (Park et al., 2002), Meteorological Research Institute Atmospheric General Circulation Model (METRI AGCM) of the Nation Institute of Meteorological Research (NIMR)(Back et al., 2002), the Global Climate Prediction System (GCPS) from the Seoul National University (SNU), Korea (Kang et al., 2004), and the second generation global forecast system at the Central Weather Bureau (CWB) in Taiwan (Liou et al., 1997). The latter type of experiments are those from the Predictive Ocean-Atmosphere model for Australia (POAMA) of Bureau of Meteorology Research Center (BMRC), Australia (Zhong et al., 2005), the coupled general circulation model (CGCM) of the Beijing Climate Center (BCC), China (Ding et al., 2000), the first version of Pusan National University (PNU) CGCM, Korea (Sun and Ahn,

2011), and the NCEP Coupled Forecast System (CFS) (Saha et al., 2006). The common model hindcast period of 1983 to 2003 was considered. For each set of models run, historical predictions for JJA were initialized in May with slightly different initial conditions for each member in the ensemble integrations. Finally, meteorological variables including SLP, Z500 and the 850 hPa winds from each individual models as well as their MME averages, which are defined as the unweighted averages of output from all models, were also used. All model hindcast data were interpolated on a  $2.5^{\circ} \times 2.5^{\circ}$  regular grid.

### **3.3 *Station rainfall data***

The raw station data consist of daily precipitation records for the period of 1980-2004. They are obtained from 250 stations in China within the domain of  $16^{\circ}\text{-}30^{\circ}\text{N}$ ,  $85^{\circ}\text{-}125^{\circ}\text{E}$ . In this study, only stations within the SC area of  $18^{\circ}\text{-}28^{\circ}\text{N}$ ,  $105^{\circ}\text{-}120^{\circ}\text{E}$ , covering Guangdong, Hainan, Fujian, Jiangxi, Guizhou Hunan provinces as well as Guangxi, Hong Kong and Macau, were considered. Also, stations were discarded whenever there are missing values for one day or more in JJA during the whole 21-year study period. As a result, 89 stations in the SC region remained. Finally, only JJA mean precipitation data within the 1983-2003 period (which is the same as the common hindcast period) were used.

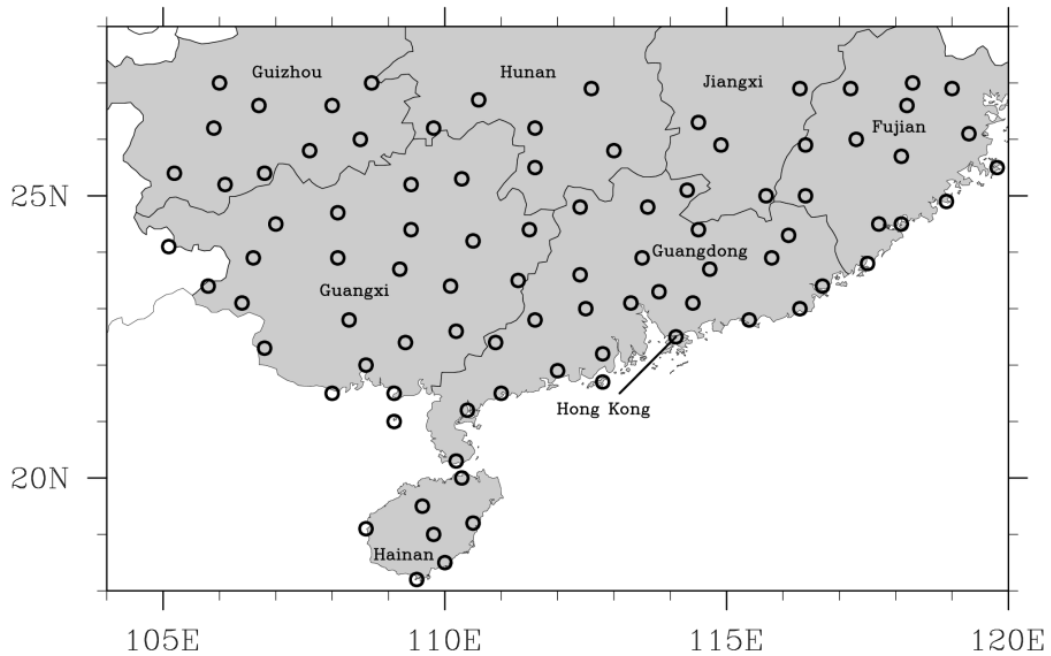


**Figure 3-1. Geographical locations of the 89 stations in SC.**

Figure 3-1 shows the geographical locations of the 89 stations considered in this study. It is seen that the resulting spatial distribution of stations is quite uniform and on average there are about one to two stations with each  $1^\circ \times 1^\circ$  sub-domain.

### 3.4 *Linear trend*

In order to focus on the interannual variability of SC rainfall, the removal of any long-term-trend in summer rainfall is necessary. It is because a long-term increase of summer rainfall can create a significant impact on the dominant patterns of anomalous summer rainfall in China (see Ye and Lu, 2012). Figure 3-2 shows the rainfall time series before and after removing the linear trend for a particular station location.

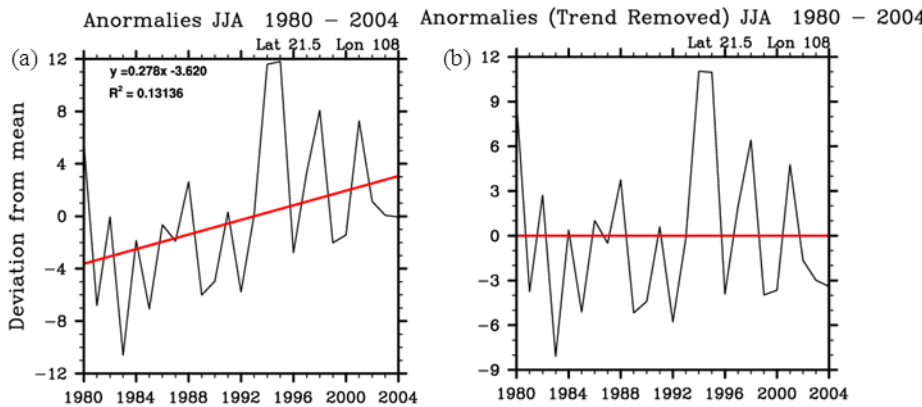


**Figure 3-2. An example illustrating the variability of SC rainfall. (a) The original anomalous rainfall for a particular station. (b) Same as (a) except with the linear trend removed.**

From Figure 3-2a, there is an obvious increasing trend in the observed summer rainfall record. This is the common feature of all stations in SC. The SC rainfall increase from 1979 has also been reported by other researchers (Ye and Lu, 2012), which can be related to a decadal change in precipitation since late 1970s. After removing the linear trends in the JJA mean rainfall as well as the gridded reanalysis and hindcast data, the influence on the decadal or long-term change can be minimized (Figure 3-2(b)). The removal procedures were similar to those of Niu and Li (2008).

### 3.5 Spatial interpolation of model rainfall output

The precipitation prediction based on DMO from GCM is for a regular grid whereas the observation (and downscaling prediction) for rainfall is measured (targeted) at station locations. Hence, it is difficult to compare DMO with observations (or downscaling results). In order to overcome this difficulty,

spatial interpolation of data (Chu and Yu, 2010), is necessary. In this study, the models' precipitation data are interpolated onto station locations, by computing a weighted average of precipitation value from the surrounding nine grid points for each station. Here the weighing factor is derived from the ratio of the distance between the centre of a particular grid and the station locations to the sum of distances of the nine grids and that station. If the grid-to-location distance is less than 10 km, however, then the model output is simply taken as the value at the station location. The advantage of this method is that the interpolated station data from GCM is more representative than the corresponding stations obtained by other linear interpolation methods (such as bilinear interpolation and nearest-neighbour interpolation).

## **Chapter 4**

### **Methodology**

In this chapter, the method of statistical downscaling rainfall prediction based on large-scale circulation variables from GCM will be explained. The flowchart in Figure 4-1 gives an outline of the research procedure of this study. In section 4.1, EOF analysis is introduced which was applied for identifying recurrent atmospheric circulation features associated with summer SC rainfall variability. The procedure of SVD analysis for downscaling is explained in section 4.2. Finally, the “leave-one-out” cross-validation method is outlined briefly in section 4.3.

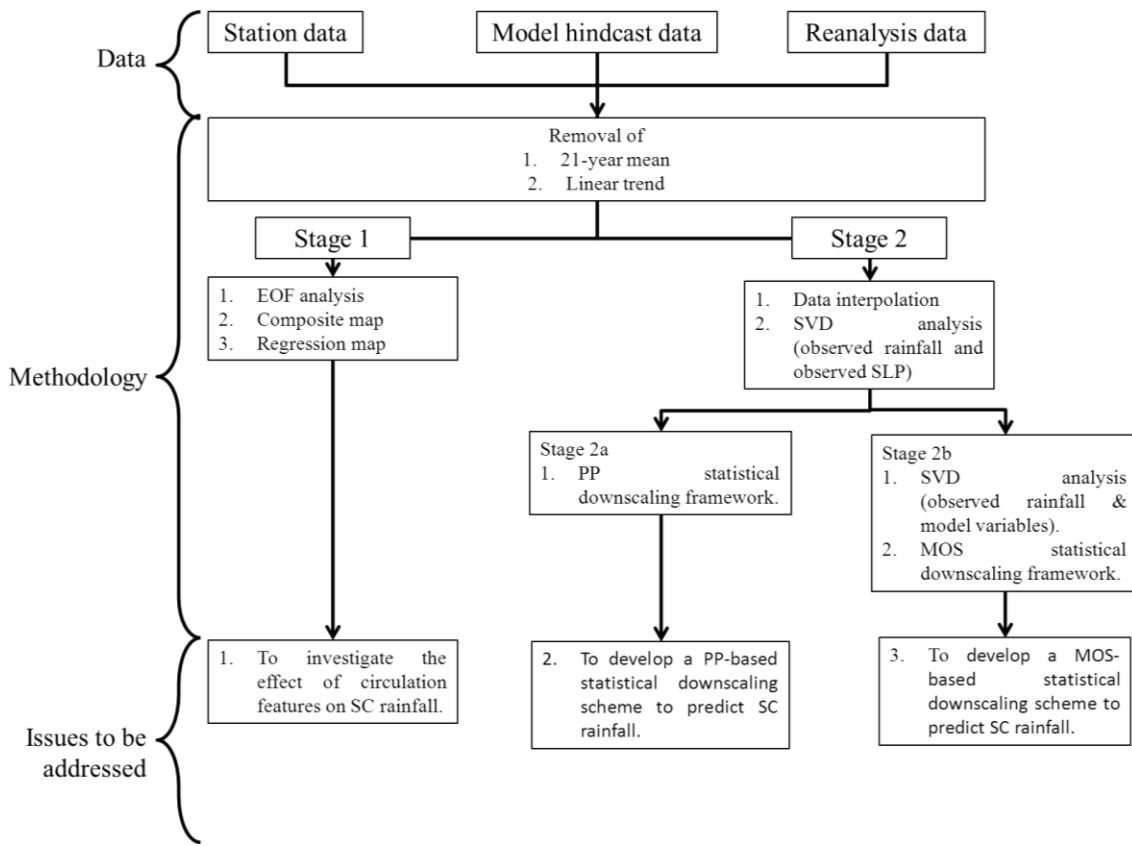


**Figure 4-1. Flowchart of the research procedure.**

#### 4.1 *Empirical orthogonal function analysis*

EOF analysis (Lorenz, 1956; Bjornsson and Venegas, 1997) is commonly used in meteorological research. The first application of EOF analysis for rainfall was conducted by Stidd (1967). Here, EOF analysis is applied to the anomalous precipitation data at 89 stations in JJA in order to obtain the recurrent precipitation patterns during the research period. Generally, eigenvectors are sorted according to the amount of variance explained. Rainfall patterns with the largest fluctuations are emphasized. Note that all eigenvectors patterns are specified up to a multiplication constant. In other words, the signs of

eigenvector patterns are arbitrary. Although the EOF patterns may provide some clues for the physical relationship between, say, the regional of large-scale circulation and SC rainfall, it should be noticed that the patterns themselves do not necessarily correspond to any physical modes.

#### **4.2 Statistical downscaling approach**

SVD (also referred to as maximum covariance analysis, or MCA; see Bretherton et al. 1992; Widmann, 2005; Tippett et al., 2008) provides an efficient way to diagonalize a rectangular matrix. It is a generalization of the diagonalization procedure that is performed in principal component analysis to matrices that are not square or symmetric. SVD of the cross-covariance matrix identifies, from, two data fields, pairs of spatial patterns that explain as much as the mean-squared temporal covariance between two field. SVD is also a method for providing better exposure of various relationships among the original data items through transforming correlated variables into a set of uncorrelated ones.

In this study (following that of Chu et al., 2008), SVD was employed in order to unveil any relationship between variability in the station precipitation and that in the large-scale circulation. The large-scale variable which has strong covariability with the SC regional precipitation (predictand) was chosen as the predictor. Both the anomalous large-scale variables and station precipitation can be expanded according to SVD as follows:

$$\text{Precipitation}(t, x) \approx \sum_{i=1}^N P_i(x) Q_i(t). \dots \quad (1)$$

$$\text{Predictor}(t, x) \approx \sum_{i=1}^N \text{Predictor}_i(x) R_i(t) \dots \quad (2)$$

Here the anomalous Predictor( $t, x$ ) and Precipitation( $t, x$ ) are normalized with unit standard deviation.  $N$  is the total number of SVD modes. Predictor <sub>$i$</sub> ( $x$ ) and  $P_i(x)$  denote the singular vectors for the  $i^{\text{th}}$  SVD mode, while  $R_i(t)$  and  $Q_i(t)$  are the time expansion coefficients corresponding to the predictor and precipitation, respectively. Finally, for downscaling prediction, the following transfer function is used:

$$\text{predicted Precipitation}(t, x) \approx \sum_{i=1}^N P_i(x)R_i(t) \dots \dots \dots \quad (3)$$

In other words, precipitation prediction is downscaled by multiplying the precipitation singular vectors with the corresponding predictor expansion coefficients. In this study, 18 SVD modes were used in reconstructing the station-scale precipitation.

#### 4.3 “Leave-one-out” cross validation

The final stage is to evaluate the skill of the downscaling prediction method by applying cross-validation. It involves the prediction of a single year precipitation, with the specific target year excluded from the training period based on which the statistical prediction scheme was constructed. This procedure was repeated for every single year and the precipitation prediction was then validated based on observations.

## Chapter 5

### Spacetime Characteristics of SC summer rainfall variability

Before we develop a statistical scheme for downscaling, EOF analysis is applied on the observed precipitation data. EOF analysis is used to investigate the variability of summer rainfall in SC due to the contribution of the dominant rainfall patterns. To begin, the first three leading rainfall patterns and the corresponding principal components (PC) obtained by EOF analysis are described in section 5.1. Next, the anomalous large-scale circulation associated with the leading EOFs based on regression is examined in section 5.2. In section 5.3, composite circulation anomalies based on EOF analysis is presented. The anomalous moisture flux divergence component and its divergence are studied in section 5.4. In addition, we also used SVD analysis to unveil the modes of covariability between precipitation and large-scale variables in section 5.5. The impact of EOF truncation on the SVD results is discussed in section 5.6.

#### **5.1    *EOF analysis of SC rainfall variability***

Using the observed precipitation at station locations, EOF analysis using covariance matrix was carried out and the first three leading EOFs are shown in Figure 5-1. (Please note that all the trends in rainfall data are removed before applying EOF analysis). Figure 5-1a shows that the first EOF is characterized by rainfall anomalies of the same sign (negative open circles) over most of the SC region. Strong precipitation anomalies are confined in coastal locations. This leading pattern explains about 36.4% of the domain-integrated precipitation variance over SC.

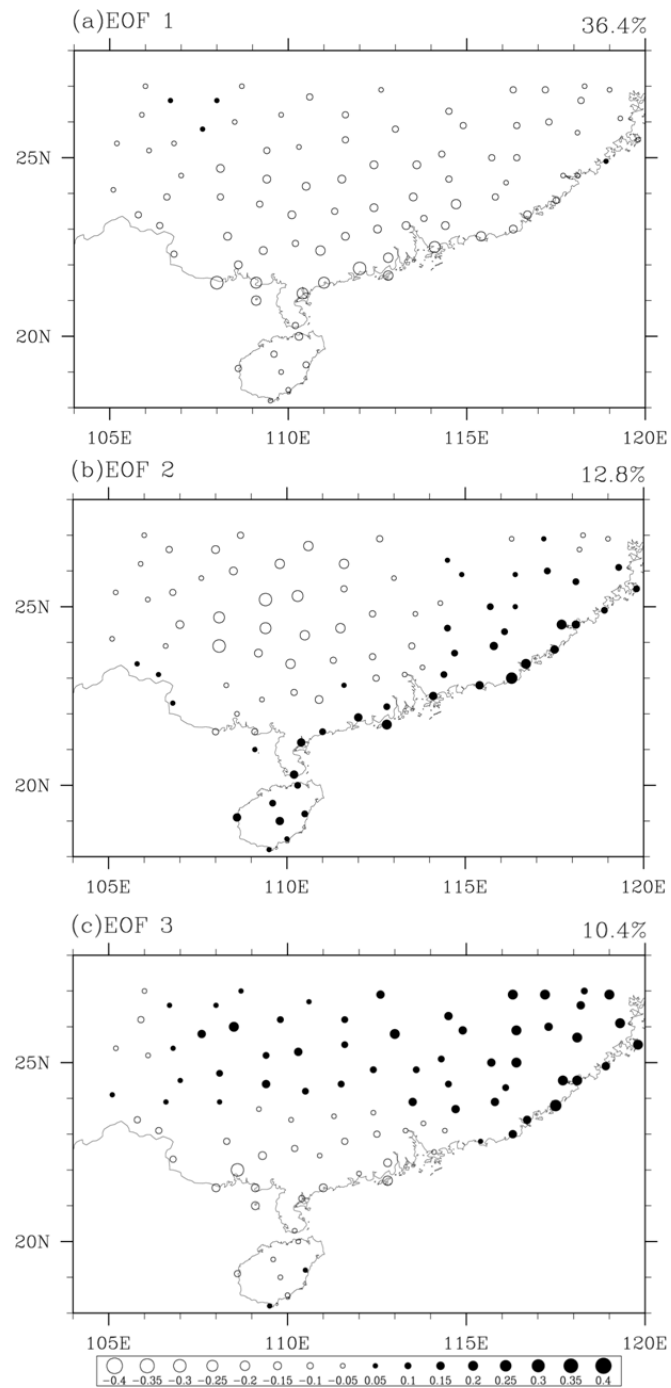


**Figure 5-1. Station precipitation (without units; normalized their corresponding square root of eigenvalue) corresponding to the (a) 1<sup>st</sup>, (b) 2<sup>nd</sup> and (c) 3<sup>rd</sup> leading EOF. Upper right shows the percentage of explained variance for each EOF.**

The second EOF for precipitation is shown in Figure 5-1b. It can be seen that rainfall anomaly along coastal SC gives an opposite sign compared to that over the more inland locations in western SC. Note that there are some relatively strong rainfall anomalies in the inland part of SC. This pattern explains about 12.8% of the total variance of SC rainfall.

The third EOF pattern, which accounts for about 10.4% of the rainfall variance, is shown in Figure 5-1c. A southwest-northeast rainfall dipole is found. Other EOFs account for less than 10% of the variance; they are not considered in this study. Principal components (PCs) corresponding to the EOFs were also calculated. Normalized PC time series (i.e., those divided by their corresponding standard deviations) are shown in Figure 5-2. From the observed rainfall record, lesser-than-normal rainfall is found in year 1989 whereas heavier-than-normal rainfall is found in year 1994 in SC. This characteristics of SC rainfall is also found in PC1 (Figure 5-2a); in particular there is a peak in year 1989 whereas 1994 gives a minimum in the PC1 time series. Based on the figure, the time series of PCs reverse their sign for every 1-2 years, indicative of variability on the inter-annual timescale. On the other hand, there is no obvious decadal change or short-term trend in the EOF products.

Next, other large-scale variables such as SLP, 850hPa wind and Z500 are regressed based on these normalized PCs to understand how the large-scale variables affecting SC rainfall variation.

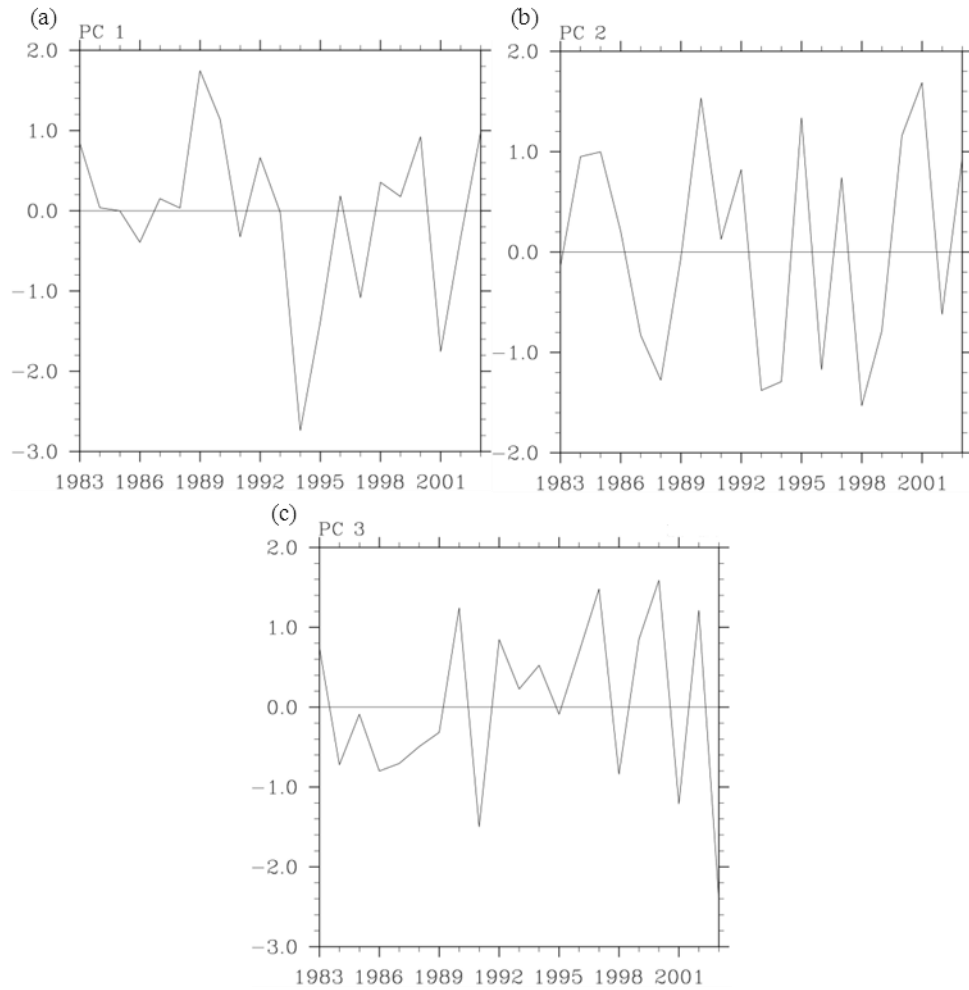


**Figure 5-2. Normalized PC time series for (a) 1<sup>st</sup>, (b) 2<sup>nd</sup> and (c) 3<sup>rd</sup> EOF mode.**

**5.2 Anomalous large-scale circulation associated with the leading EOFs based on linear regression**

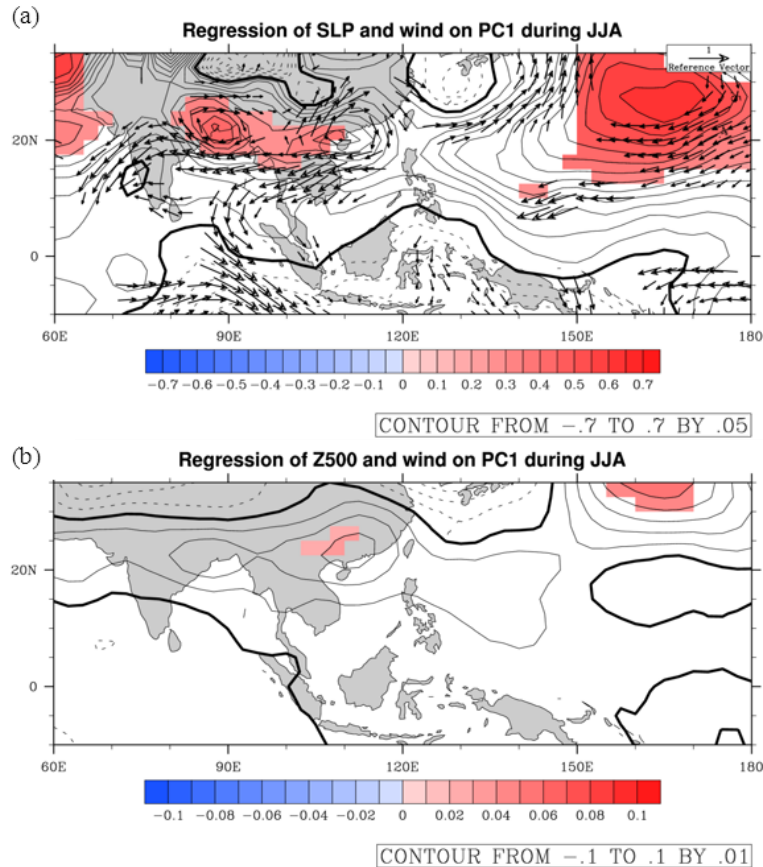


**Figure 5-3. Regression of (a) 850hPa wind (see scale arrow in upper right; units:  $\text{ms}^{-1}$ ) and SLP (contours in interval of 0.05 hPa, with negative values denoted by dashed lines), and (b) Z500 (contours in interval of 0.01 hPa), based on the leading normalized PC time series of SC rainfall. Shading (arrows) denotes either SLP (850 wind) or Z500 signals significant at the 90% level.**

In this section, regression maps for SLP, 850 hPa wind and Z500 are used to investigate the relationship between large-scale variables and the leading EOFs. Figure 5-3a shows the regression map of SLP based on PC1 of SC rainfall. In the figure, positive anomalous SLP associated with anomalous anti-cyclonic flow which passed the 90% significance level are observed over SC and IndoChina. Besides, along-shore wind off Sumatra and anti-cyclone in SC are observed. Although our findings do not repeat the results presented by Li and Mu (2001; see their Figure 2-3), a resemblance with the anomalous circulation typical of IOD events can be discerned. From Figure 5-3b, large-scale positive anomalous Z500 covers Bay of Bengal and SC, which is consistent with the SLP map (Figure 5-3a). Suppressed rainfall given by the leading EOF is seen to be associated with the presence of the high pressure system over SC. Later, a moisture budget analysis will be presented in order to understand the effect of anomalous moisture transport on SC rainfall.

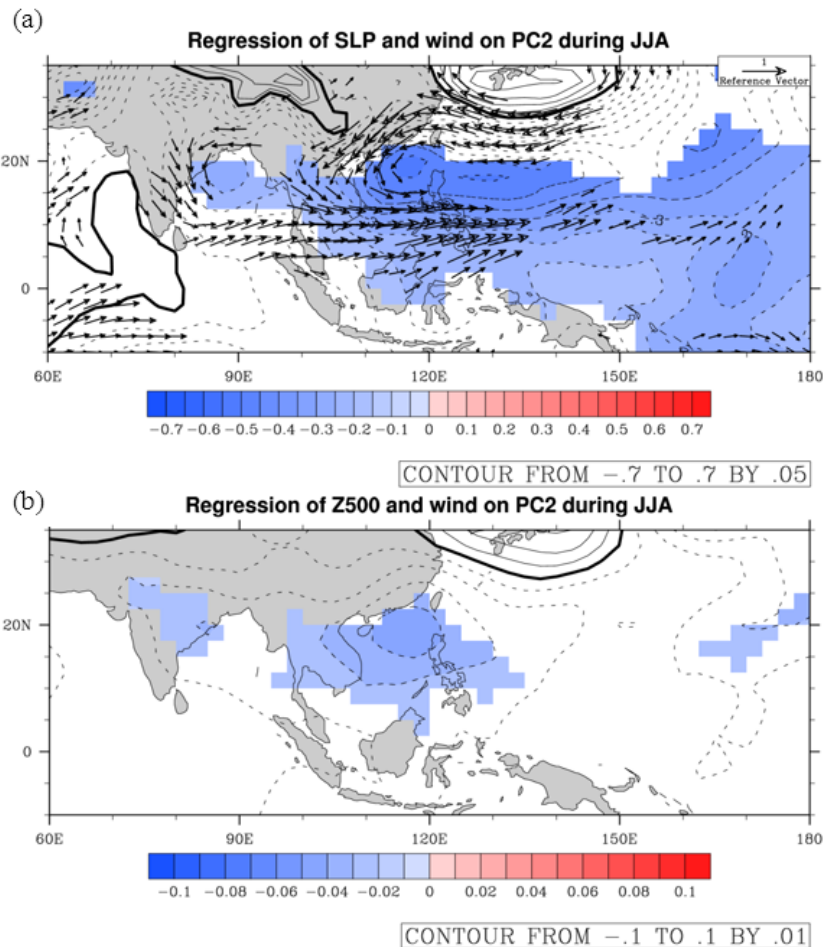


**Figure 5-4.** Same as Figure 5-3 except for regression based on PC2.

Regression maps of SLP and Z500 based on PC2 are shown in Figures 5-4a and 5-4b, respectively. Negative SLP anomalies are observed over SCS and the western north Pacific. Meanwhile, positive anomalous SLP is found over the northwest SC and south of Japan. Moreover, a large-scale low-level cyclone is seen over the western north Pacific. Such anomalous large-scale circulation patterns are very similar to those related to WNPSM activity described by Wang et al. (see their Figure 2-2). At the same time, large-scale negative (positive) anomalous Z500 is located in SCS (south Japan).

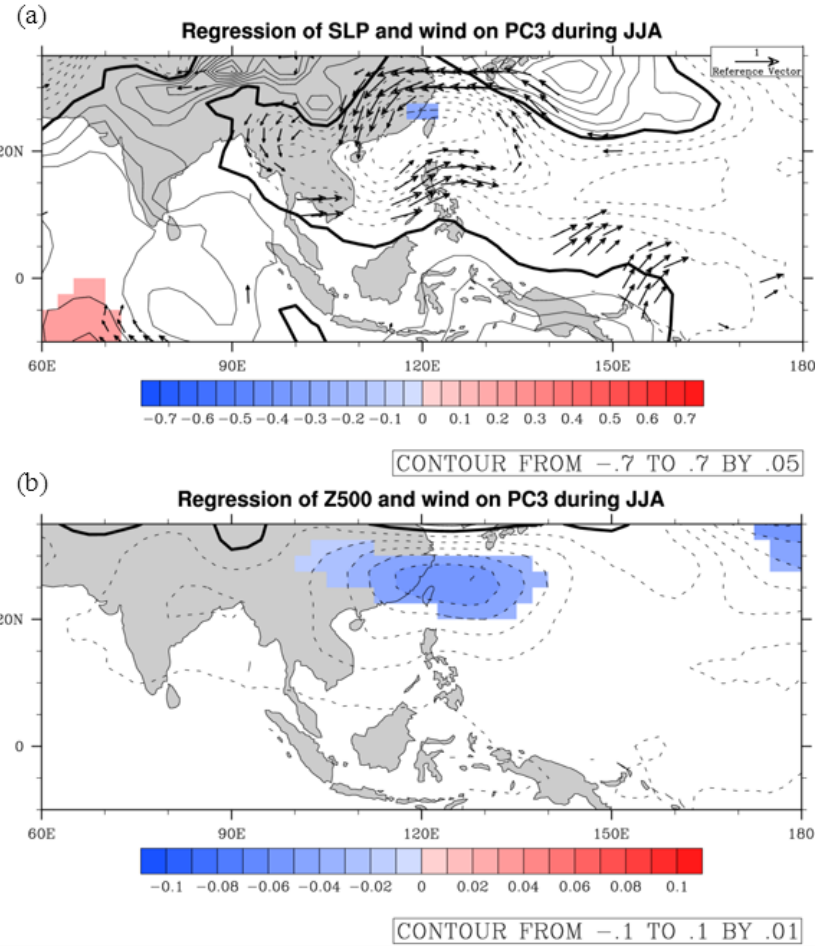


**Figure 5-5. Same as Figure 5-3 except for regression based on PC3.**

Figures 5-5a and 5-5b show the regression map of SLP and Z500 onto PC3, respectively. There is a weakened subtropical high (passing the 90% significance level) from Taiwan to the western north Pacific in the surface to the mid-troposphere. This weakened subtropical high signal extends to northeast SC and hence affects the precipitation there. Next, SC precipitation variability is investigated and discussed.

### **5.3 Composite circulation anomalies based on EOF analysis**

Composite circulation anomalies can also help us to have a better understanding of the relationship between the large-scale circulation and the rainfall EOF pattern. Here the composite maps are computed by taking the difference between the value of a particular variable averaged over the positive, and those over negative extreme years. An extreme year for a particular EOF mode is defined as (1) the year in which the absolute value of the corresponding PC is largest among the first 3 PCs; and (2) at the same time the absolute value of the normalized PC is greater than 1 (meaning that its variation is larger than its corresponding standard deviation). These extreme years are further classified into positive and negative extremes according to sign of the corresponding PCs. From Figure 5-2a, it can be seen that there are 6 extreme years for the leading EOF; they are 1989, 1990, 1994, 1995, 1997 and 2001. For the 2<sup>nd</sup> EOF, the extreme years are 1985, 1988, 1993, 1996 and 1998 (see Figure 5-2b); and those for the 3<sup>rd</sup> EOF are 1991, 2000, 2002 and 2003 (see Figure 5-2c). Next, the value of the large-scaled variables such as SLP and Z500 in these extreme years will be extracted and calculated to obtain composites for the corresponding EOF modes.

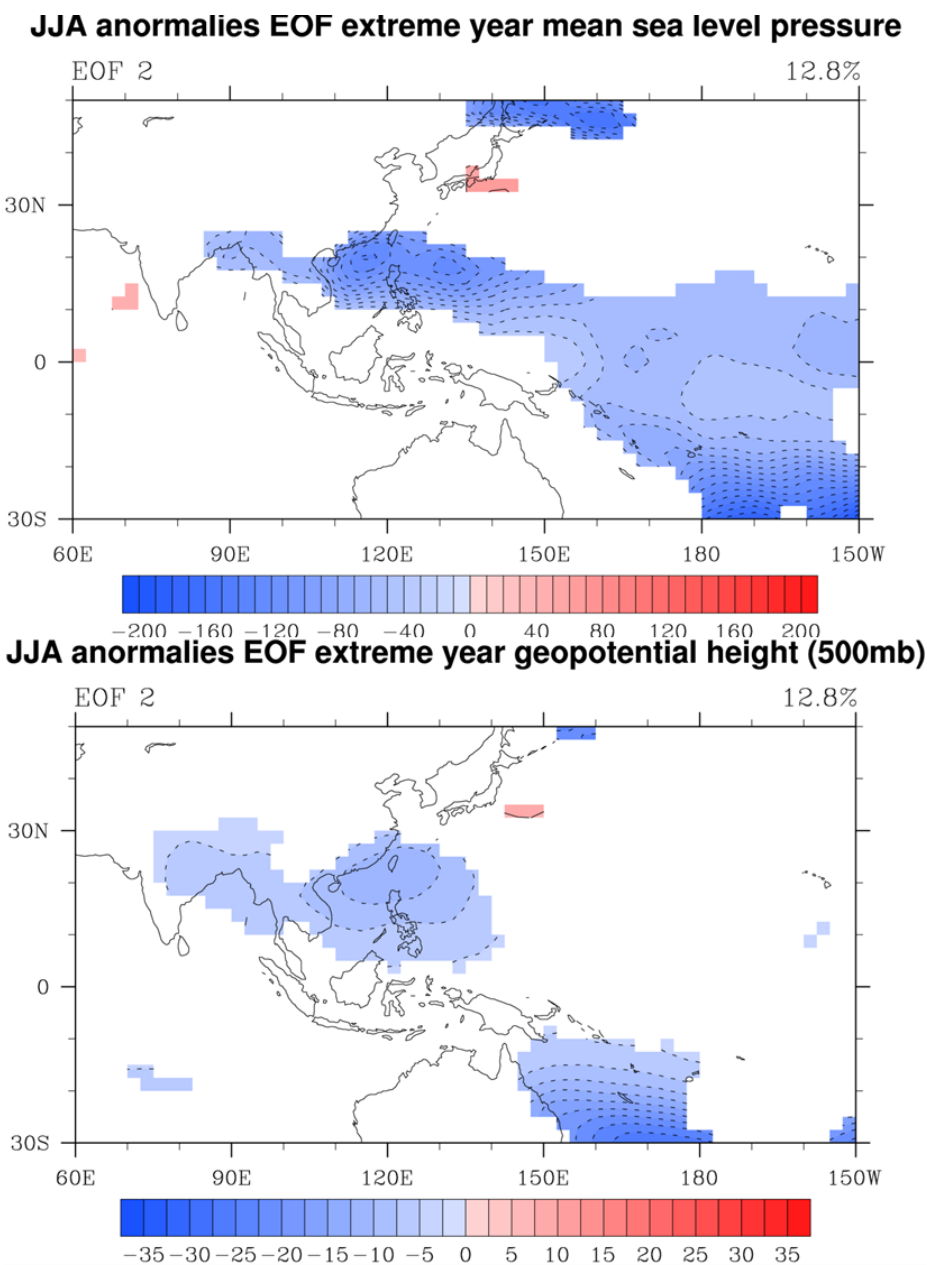


**Figure 5-6. Composite maps for (a) SLP (contours in interval of 10 hPa) and (b) Z500 (contours in interval of 2.5 hPa) of the 2<sup>nd</sup> EOF. Shading denotes SLP and Z500 signals significant at the 90% level.**

Figures 5-6a and 5-6b show the composite maps of SLP and Z500 corresponding to the 2<sup>nd</sup> EOF, respectively. As shown in Figure 5-6a, the large-scale negative anomalous SLP which passed the 90% significance level is found over SC and the western north Pacific. At the same time, positive SLP anomalies are observed over Japan. Anomalous easterlies (westerlies) can be inferred over the region of 20°-30°N, 110°-140°E (5°-15°N, 100°-130°E), which are indicative anomalous WNPSM activity. Figure 5-6b shows negative anomalous Z500 which exceeded 90% significance level at SC extending to western north Pacific and IndoChina. Overall, these composite maps are consistent with the regression results presented earlier (see Figure 5-4). The composite maps corresponding to the 1<sup>st</sup> and the 3<sup>rd</sup> EOF extreme years are not shown, since the signals are not statistically significant. The low significance is due to the fact that only a few extreme years could be extracted from the research period to obtain the composite maps.

#### **5.4 Anomalous moisture flux divergence and wind divergence.**

A moisture budget analysis can shed light on how precipitation variation is related to the anomalous circulation. In particular, the moisture budget equation (Prixoto and Oort, 1991) can be derived from the equation:

$$\frac{dq}{dt} = S.$$

where

$$\frac{d}{dt} = \frac{\partial}{\partial t} + u \frac{\partial}{\partial x} + v \frac{\partial}{\partial y} + \omega \frac{\partial}{\partial p},$$

with  $u, v$  and  $\omega$  representing the zonal, meridional and pressure velocity, respectively, whereas  $q$  indicates the specific humidity;  $S$  represents the difference between the sources and the sinks of water vapour following air parcel motion. The column-integrated value of  $S$  is given by  $E-P$ , where  $E$  ( $P$ ) is the local evaporation (precipitation) rate. Thus,

$$\frac{\overline{\partial w}}{\partial t} + \nabla \cdot \vec{Q} = \bar{E} - \bar{P}$$

where  $\vec{Q}$  is the vertically integrated mean total moisture flux. For seasonal means, the storage term  $\frac{\overline{\partial w}}{\partial t}$  is usually negligible compared to the other terms.

Hence, the moisture flux divergence can be simply written as

$$\nabla \cdot \vec{Q} \approx \bar{E} - \bar{P}$$

Based on the moisture flux equation, if the precipitation is larger (smaller) than the evaporation, the L.H.S of the equation be negative (positive) implying convergence (divergence) of  $\vec{Q}$ . The analysis can therefore help to illustrate the moisture transport and its relationship with precipitation and evaporation in SC.

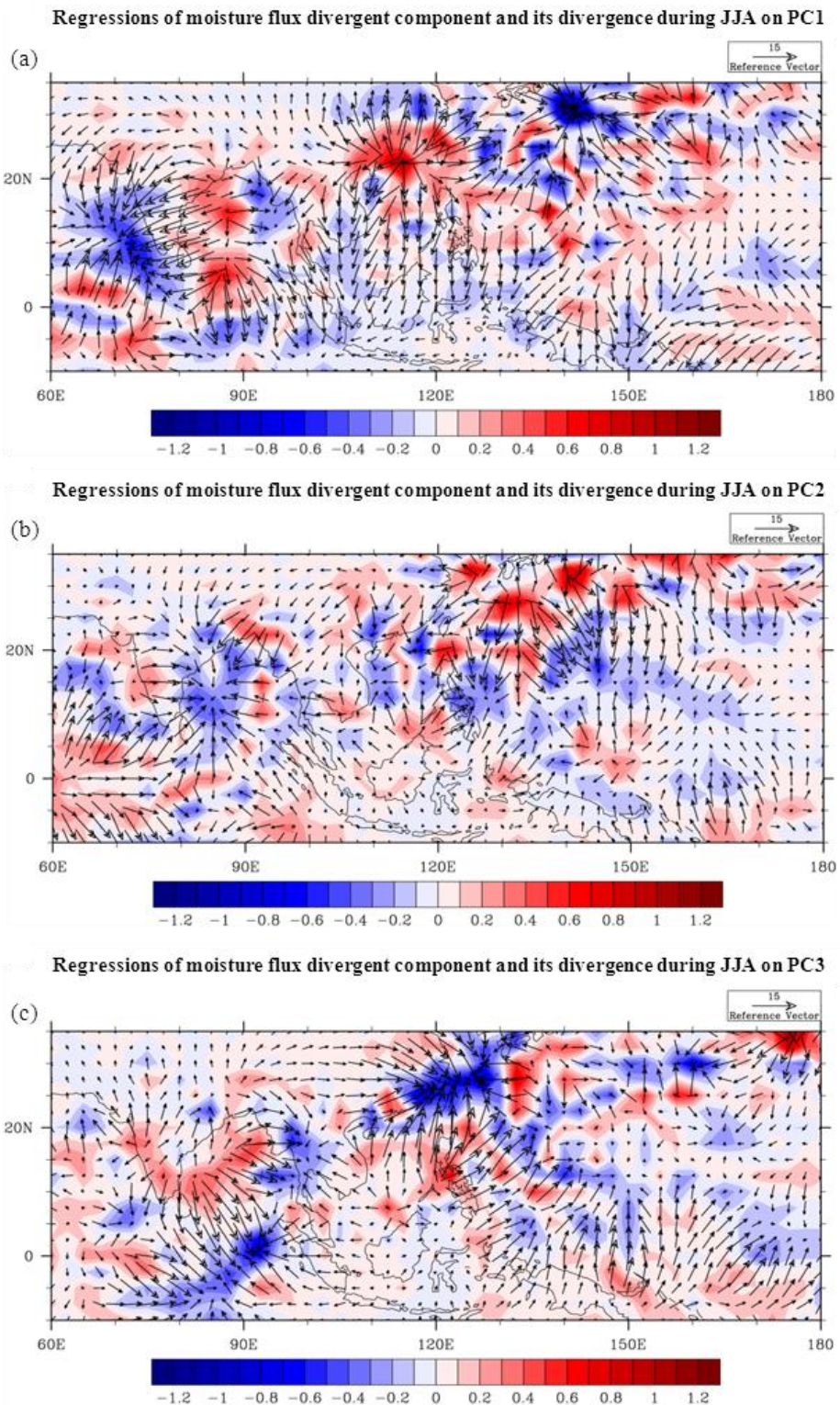


**Figure 5-7. Regression map of moisture flux divergent component (arrows) and its divergence (shading) based on (a) PC1, (b) PC2 and (c) PC3.**

Figure 5-7 shows the regression map of the anomalous moisture flux divergent component (arrows) and its divergence (shading) onto the corresponding PCs. The regression map based on PC1 is shown in Figure 5-7a. It can be seen that the anomalous divergence of moisture flux is observed over SC. Together with Figure 5-3a, result indicates that water vapour is transported away from the SC area when an anomalous high is present with same region. As a result, suppressed rainfall is observed over SC area.

For the regression pattern based on PC2, anomalous moisture flux convergence is found over the coastal part of SC (Figure 5-7b). Such anomalous convergence of the moisture flux over SC and SCS is consistent with the surplus precipitation in the coastal area. From the regression map onto PC3 (Figure 5-7c), anomalous moisture flux is found to be convergent over Taiwan and the western north Pacific. Thus there is convergence of moisture transport associated with the anomalous low-level cyclone in the region (see Figure 5-5). These anomalous circulation features are conclusive to surplus rainfall over northeast SC.

### **5.5 SVD analysis based on station rainfall and SLP/Z500.**

In the previous sections, the dominant modes of SC rainfall variability were found by using EOF analysis. Applying regression analysis, the relationship between large-scale variables and the leading rainfall EOFs was also obtained. In this section, SVD analysis is carried out in order to find out the covariability between SC rainfall and the large-scale flow. Based on the previous results, the domain for analysis is chosen to be the region of 10°S-35°N and 60°-180°E for the large-scale circulation variable. Results of SVD analysis are presented in subsections 5.5.1 and 5.5.2.

### 5.5.1 SLP

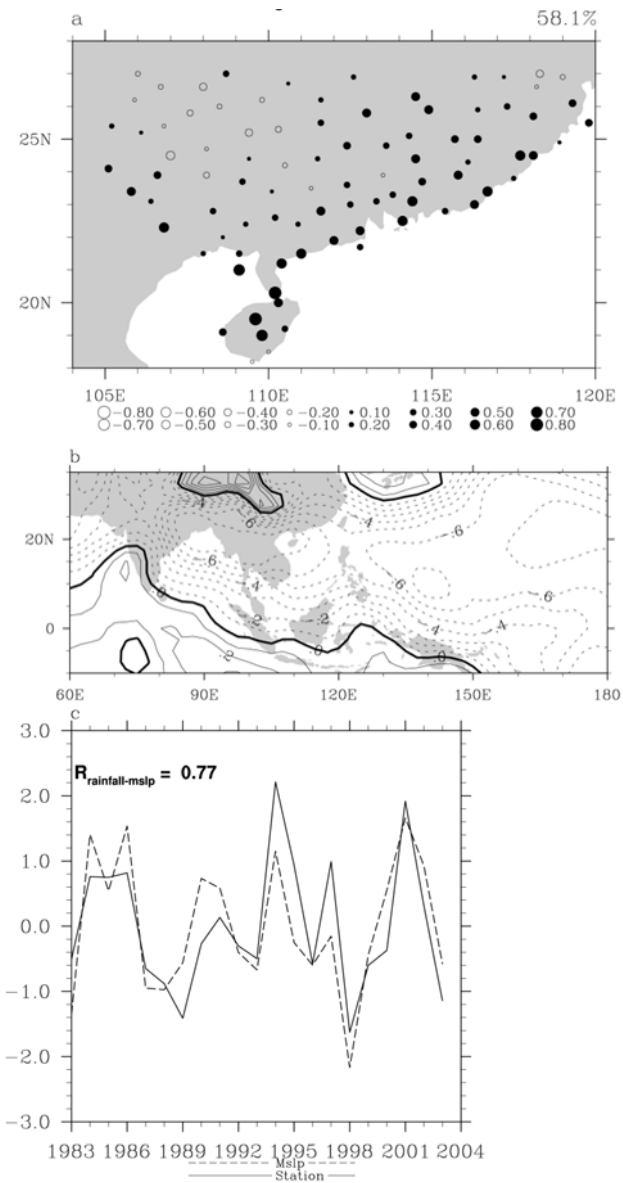


**Figure 5-8.** The dimensionless leading singular vector for (a) observed station precipitation and (b) SLP from observations based on SVD analysis. The fraction of squared covariance between two field explained by the leading mode is shown on upper right. (c) Normalized time series of the expansion coefficient for precipitation (solid line), SLP (dashed line). Upper left shows the correlation coefficient between SLP and SC rainfall.

The patterns associated with the first SVD mode for the observed station precipitation and observed SLP are shown in Figure 5-8. This mode explains about 58% of the squared covariance between station rainfall and SLP. Large-scale negative SLP anomalies are observed not only at Hainan to IndoChina, but also in the western north Pacific. Meanwhile, positive anomalous SLP is found over the northwest SC, southern Japan and the Indian Ocean to Indonesia. Associated with the anomalous SLP, positive rainfall anomalies (solid circles) are found at the coastal and east SC, whereas negative rainfall anomalies (open circles) are found over the northwest SC. Thus, the placement of the positive (negative) anomalous SLP and the suppressed (enhanced) rainfall in SC are consistent with each other. In addition, notice that the rainfall and SLP patterns of the leading SVD mode are similar to the 2<sup>nd</sup> EOF of precipitation (Figure 5-1b) and the corresponding regression map of SLP (Figure 5-4a), respectively. These circulations are also consistent with the schematic diagram of WNPSM which shows an anticyclone over the Japan and cyclone over western north Pacific. Based on these findings, it is suggested that this SVD mode is related to the anomalous WNPSM activity.

The normalized expansion coefficients for the station rainfall and SLP corresponding to this leading mode are given in Figure 5-8c. It is noteworthy that the two time series are highly correlated (with a correlation coefficient of 0.77), meaning that SC rainfall is strongly coupled with large-scale SLP in the Indo-Pacific region.

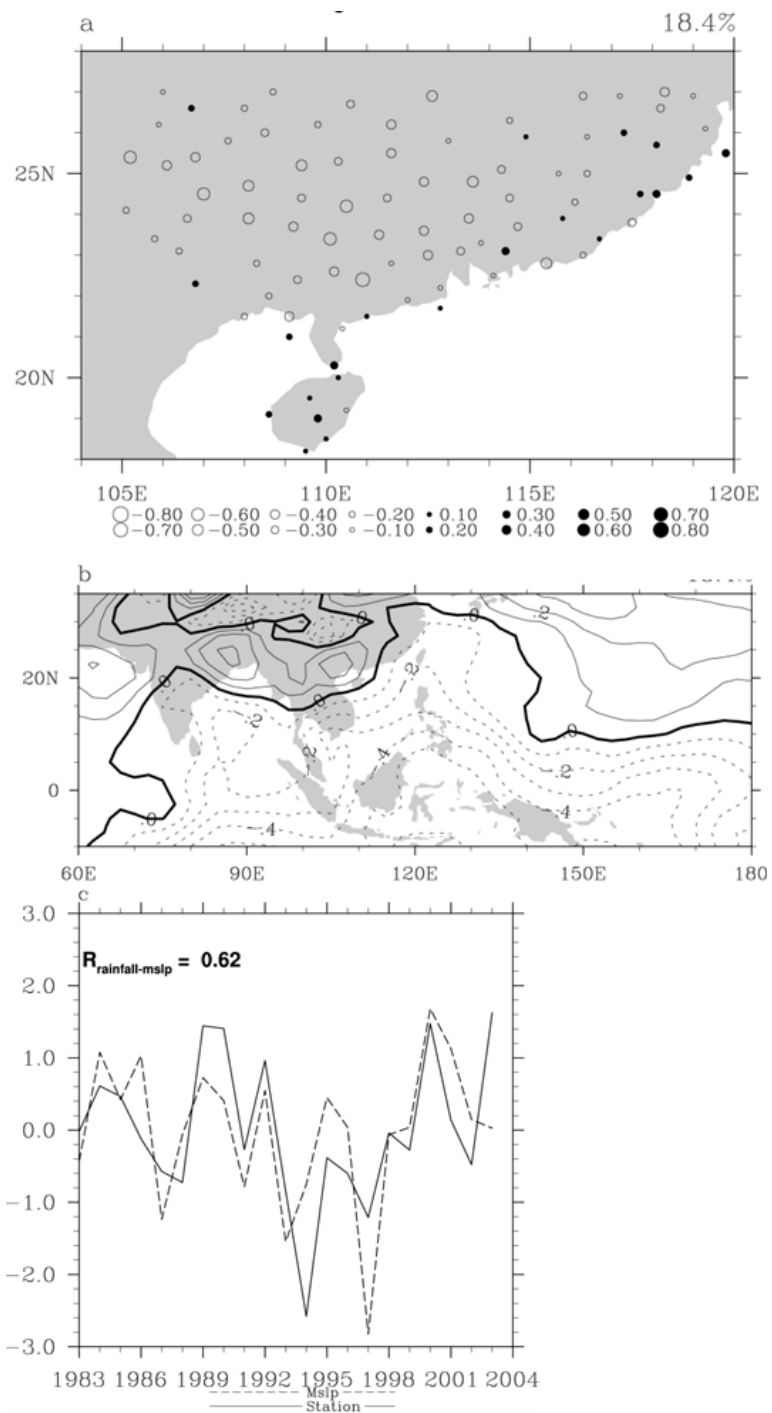


**Figure 5-9.** Same as Figure 5-8, except for the 2<sup>nd</sup> singular vector.

The second set of SVD patterns are shown in Figure 5-9. This mode accounts for about 18% of the squared covariance. As shown in Figure 5-9a, negative anomalous rainfall is found over the northwest inland part of SC whereas positive rainfall anomalies are observed along the coastal area and over the Hainan Island. The suppressed rainfall in SC is accompanied by positive anomalous SLP covering SC and Indochina (Figure 5-9b). Different from the leading SVD, this set of second SVD patterns of rainfall and SLP are similar to the leading EOF for rainfall (Figure 5-1a) and also the SLP regressed onto PC1, respectively. Figure 5-9c presents the time expansion coefficient of the station rainfall and SLP corresponding to the second SVD. The correlation between these two time series is about 0.62.

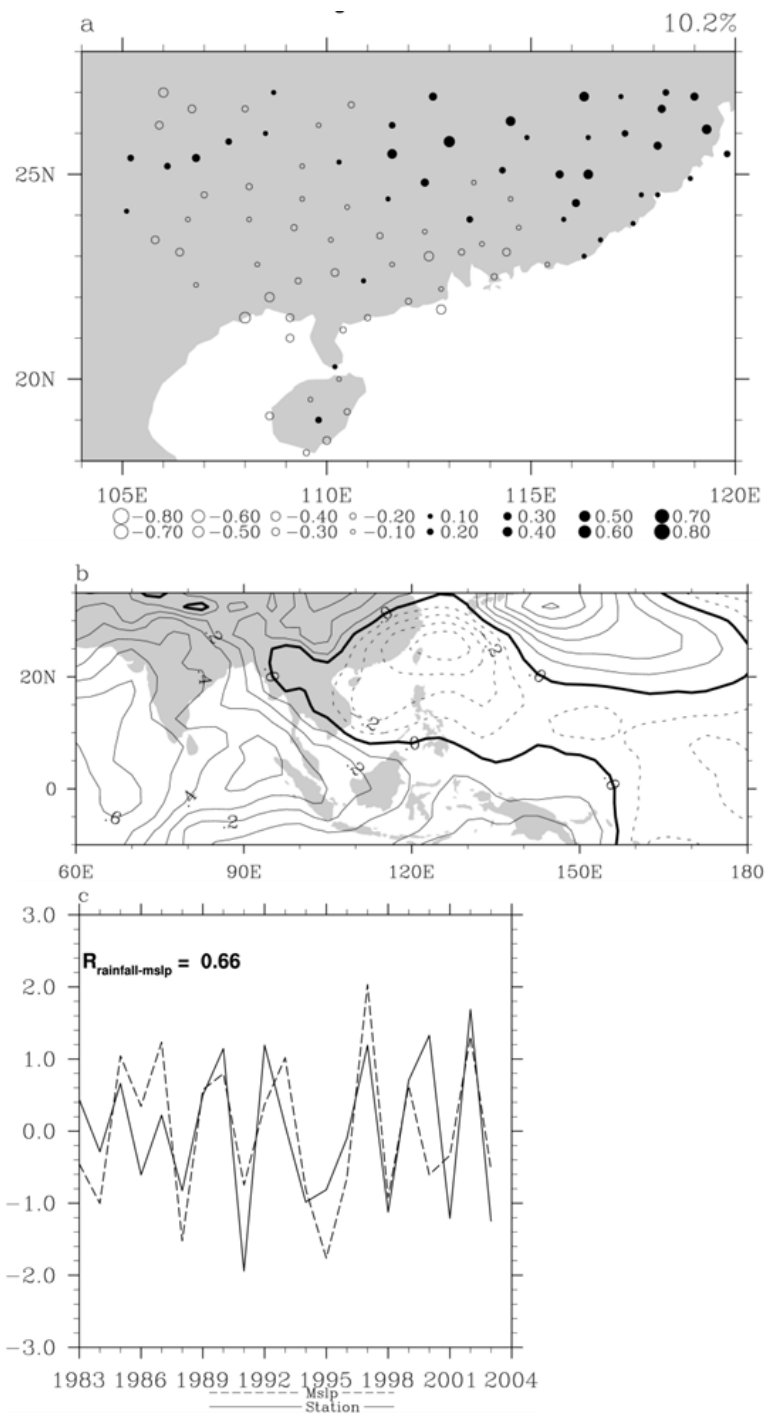


**Figure 5-10.** Same as Figure 5-8, except for the 3<sup>rd</sup> singular vector.

Figure 5-10 shows the anomalous rainfall and SLP associated with the third SVD mode, the latter of which accounts for about 10% of the rainfall-SLP squared covariability. It shows positive (negative) anomalous precipitation at the northeast (southwest) part of SC (Figure 5-10a). This mode suggests a connection between a northeast-to-southwest dipole precipitation pattern over SC and the anomalous SLP with a centre of action at Taiwan/western north Pacific (Figure 5-10b). Note that the third SVD mode patterns also resemble the 3<sup>rd</sup> EOF for rainfall (Figure 5-1c) and the corresponding SLP regression map (Figure 5-5a). The correlation between the rainfall and SLP expansion coefficients for this mode is 0.66.

Correlation coefficient	(a) Rainfall	(b) SLP
Between leading SVD mode & WNPMI	0.67	0.89
Between 2 <sup>nd</sup> SVD mode & DMI	-0.54	-0.52
Between 3 <sup>rd</sup> SVD & Nino 3 index	0.21	0.53

**Table 5-1. Correlation coefficient between time expansion coefficient of the leading SVD modes and climate indices for (a) rainfall and (b) SLP.**

Table 5-1 shows a summary of correlation between SLP expansion coefficient time series for the leading SVD modes and a number of climate indices, namely WNPMI, DMI and the Nino 3 index. It has been seen that the SLP pattern for the leading SVD mode is very similar to the anomalous WNPSM SLP feature (see Figures 5-8b and 2-3). Moreover, both time series for rainfall and SLP are highly correlated to WNPMI, implying that the leading SVD is related with the anomalous WNPSM activity.

The second SVD mode seems to be related to IOD although the along-shore wind off Sumatra is difficult to infer from Figure 5-9b. Notice that the time expansion coefficient of SLP and rainfall are both negative correlated to DMI during JJA (with correlation coefficient of -0.52 and -0.54, respectively, passing the 95% significance level). In other words, positive anomalous rainfall is found when DMI is positive, and vice versa, which is consistent with previous studies (see, e.g. Xiao et al., 2002). Finally, the time expansion coefficient of SLP for the third SVD mode is found to be correlated with Nino3 index, with a correlation of 0.53 (which passes the 95% significance level). It means that the SLP pattern is related to ENSO, which plays a role in affecting the local SC rainfall.

## 5.5.2 Z500

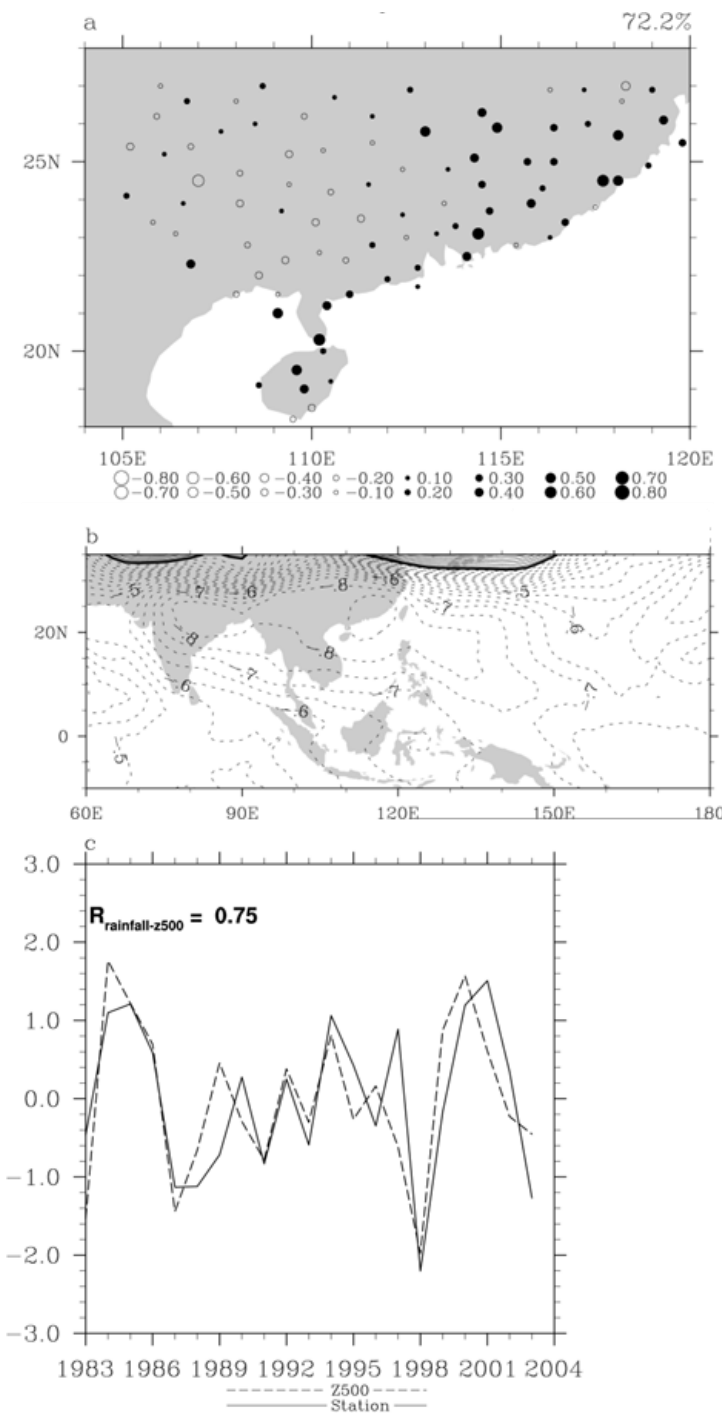


**Figure 5-11.** Same as Figure 5-8, except based on Z500 from observations.

In addition to SLP, SVD analysis based on station rainfall in SC and Z500 is also carried out. The results of the leading SVD patterns for the observed precipitation and Z500 are shown in Figure 5-11. This mode explains about 72% of rainfall-Z500 squared covariability, which is higher than that using SLP. Large-scale negative anomalous Z500 is located in the northern tropical region ( $0^{\circ}$ - $30^{\circ}$ N) (Figure 5-11b). Besides, positive anomalous Z500 are observed in Japan, again consistent with that expected for anomalous WNPSM activity (i.e., an anti-cyclone at the 500hPa level over Japan). Associated with these anomalous Z500 signals, positive (negative) rainfall anomalies are found over the east coastal (northwest) SC. Again, this leading precipitation singular vector and the 2<sup>nd</sup> EOF pattern are very similar (Figure 5-1b). Notice that rainfall in SC is also strongly coupled with the large-scale Z500 since the normalized expansion coefficients for these two variables are highly correlated, with a correlation coefficient of 0.75 (Figure 5-11c).

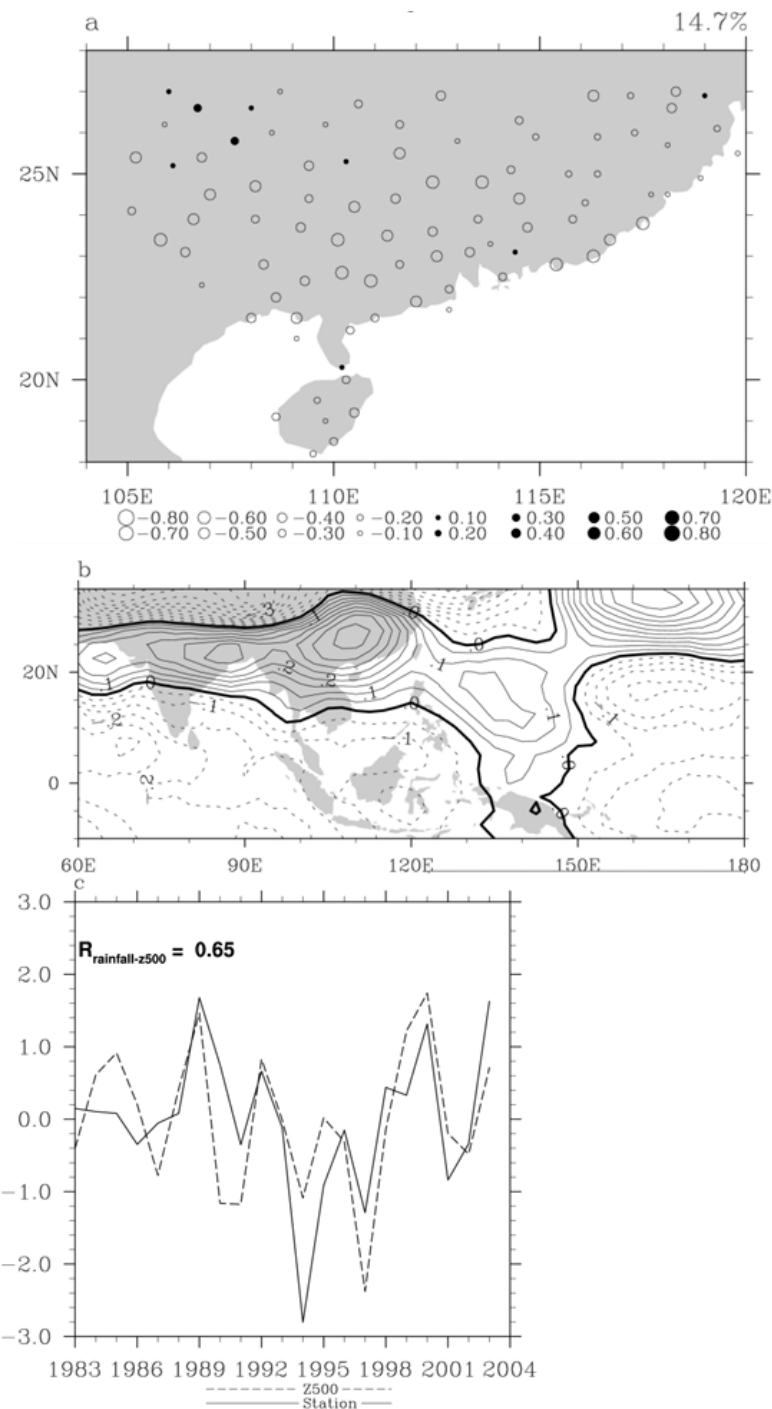


**Figure 5-12.** Same as Figure 5-11, except for the 2<sup>nd</sup> singular vector.

Patterns for the 2<sup>nd</sup> SVD mode based on Z500 and station rainfall are shown in Figure 5-12; the correlation coefficient between expansion coefficients is 0.65. The 2<sup>nd</sup> SVD mode explains about 15% of the squared covariance of rainfall and Z500. As shown in Figure 5-12a, negative rainfall anomalies are observed over SC, consistent with the SVD result based on SLP (Figure 5-9a) and similar to the leading rainfall EOF (Figure 5-1a).

Besides, large-scale positive anomalous Z500 is observed in SC and it extends to the western north Pacific (Figure 5-12b). In the Z500 regression map based on PC1, very similar positive Z500 anomaly is also found (Figure 5-3b). It implies that negative rainfall anomalies are accompanied by a positive geopotential height anomaly. This finding agrees with that given by Li and Mu (2001) during positive IOD, suggesting a linkage between IOD activity and this SVD mode. (Note that the 2<sup>nd</sup> SVD mode expansion coefficients are significantly correlated with DMI; see Table 5-2)

For the 3<sup>rd</sup> SVD mode, positive (negative) anomalous rainfall is observed in northeast (southwest) SC (figure not shown). This mode explains about 5% of the rainfall-Z500 squared covariability, meaning that it is physically meaningless.

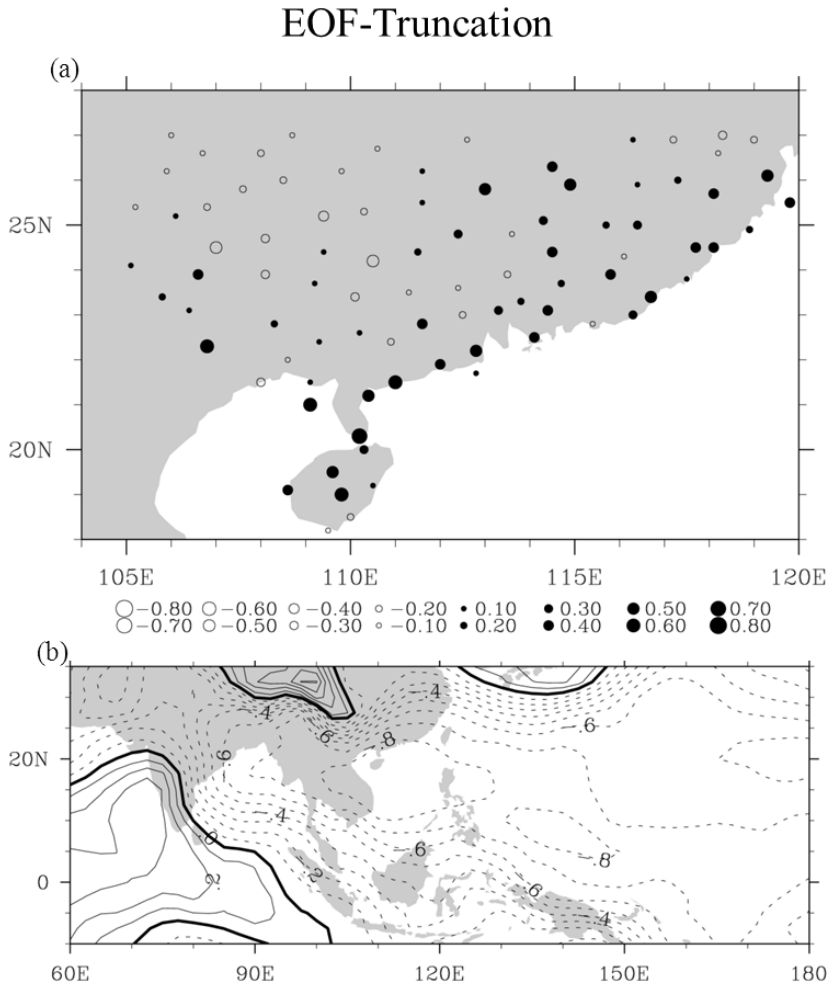
Correlation coefficient	(c) Rainfall	(d) Z500
Between leading SVD & WNPMI	0.74	0.62
Between 2 <sup>nd</sup> SVD & DMI	-0.53	-0.53

Table 5-2. Same as Table 5-1 except for Z500.

Table 5-2 shows a summary of the correlation between expansion coefficient time series for SVD analysis based on Z500 and various climate indices. From the table, it is seen that the leading SVD mode is closely associated with anomalous WNPSM activity because the expansion coefficients are highly correlated with WNPMI.

The 2<sup>nd</sup> SVD mode is also related to IOD. The correlation between the expansion coefficients (for both rainfall and Z500) and DMI is about -0.5 (passing 95% significance level). In other words, this SVD pattern is negative correlated to positive IOD. To conclude, the precipitation in SC is related to three prominent Indo-Pacific climate phenomena namely anomalous WNPSM, IOD and ENSO.

### 5.6 The impact of EOF truncation



**Figure 5-13. The dimensionless leading singular vector for (a) station precipitation and (b) SLP based on SVD analysis with EOF truncation.**

In this section, the impact of EOF filtering on the results of SVD analysis is examined. The advantage of the EOF filtering method is to reduce the “climate noise” of input data before applying SVD analysis. Notice that part of the information in the original input field will be lost after EOF truncation. Figure 5-13 shows the leading SVD mode of the station rainfall and observed SLP with EOF truncation. Comparing this to the result shown in Figure 5-8, it

can be seen that the impact of EOF filtering on the SVD results is insignificant. Both give positive rainfall anomalies in the coastal area and negative rainfall anomalies at northwest SC (see Figure 5-8a and 5-13a. Meanwhile, negative anomalous SLP is located in the regions of Vietnam and IndoChina for the leading SVD mode. To conclude, since noise removal (EOF truncation) does not cause significant differences, no EOF truncation was applied before carrying out the SVD analysis in this study.

## **Chapter 6**

### **SC rainfall prediction based on direct model output and statistical downscaling**

In Chapter 5, the dominant rainfall patterns in SC have been determined using EOF analysis. It has found that the variability of SC rainfall is associated with the large-scale circulation anomalies over Indo-Pacific region, which in turn can be linked with the anomalous WNPSM activity, IOD and ENSO. Moreover, the relationship between anomalous rainfall in SC and the observed large-scale circulation (as revealed by SLP and Z500 anomalies) has also been obtained through employing SVD analyses. In this chapter, SVD analysis is used again to develop a statistical scheme for rainfall prediction in SC based on model SLP as predictor. The SC rainfall prediction based on DMO is presented and evaluated in section 6.1. Next, the performance of the PP-based downscaling scheme is evaluated in section 6.2. SVD analysis is applied again for obtaining the relationship between SC rainfall and model SLP in section 6.3, and MOS-based downscaling prediction is presented and evaluated in section 6.4. Finally, how statistical downscaling can enhance SC rainfall prediction in certain locations is examined in section 6.5.

### 6.1 SC rainfall predictions based on direct model output

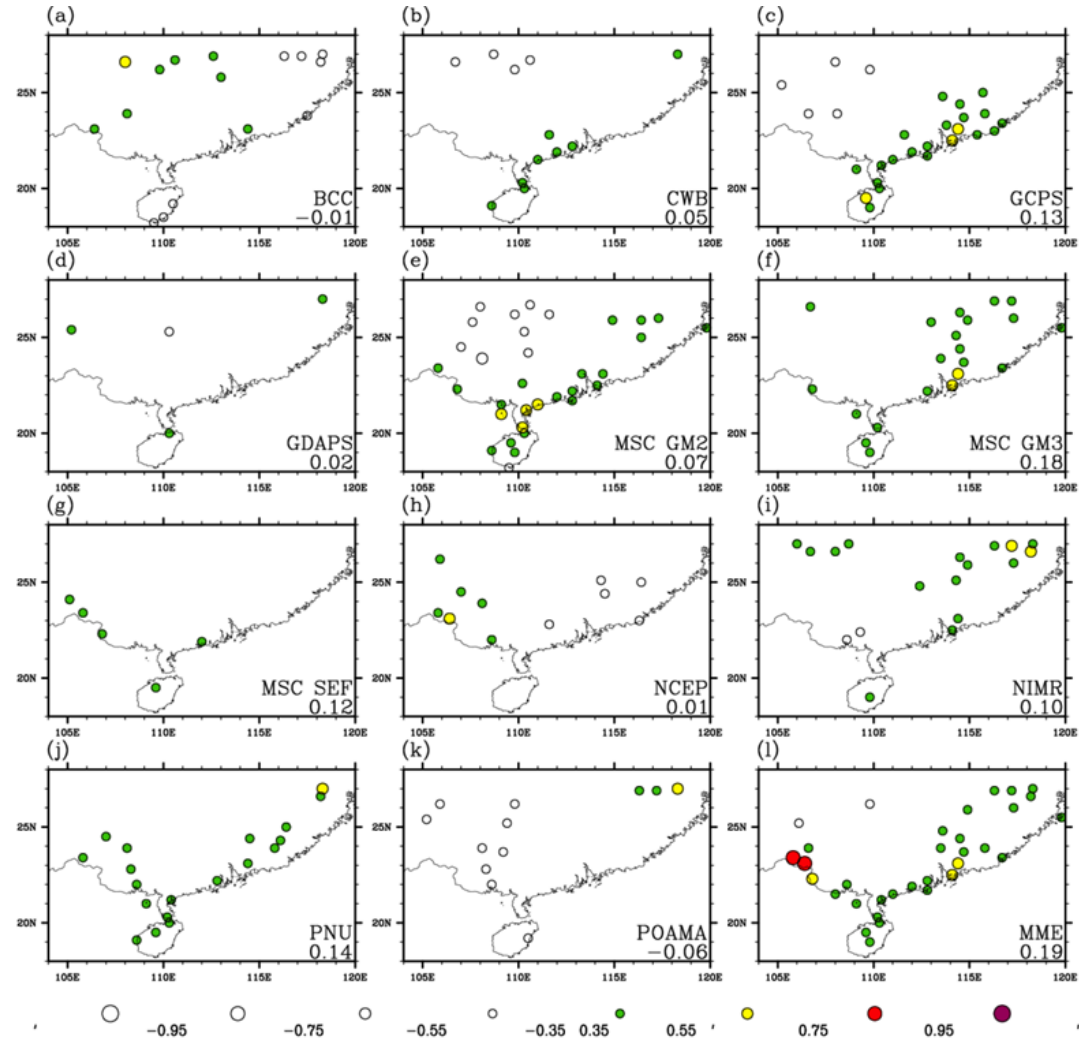


**Figure 6-1. Correlation coefficients between the JJA precipitation (exceeded 90% significance level) at station locations based on observations and the interpolated DMO of precipitation from (a) BCC (b) CWB (c) GCPS (d) GDAPS (e) MSC-GM2 (f) MSC-GM3 (g) MSC-SEF (h) NCEP (i) NIMR (j) PNU (k) POAMA, and (l) the MME average. The correlation coefficient averaged over all stations is provided in the bottom right corner.**

Before evaluating the performance of models in predicting the local SC rainfall, rainfall predictions based on DMO were first spatially interpolated onto each station location (see section 3.5). The correlation between the observed and DMO precipitation at 89 stations which passed 90% significance level is shown in Figure 6-1. The 89-station averaged correlation coefficient is also shown at the bottom right of each panel. Most models show skilful rainfall predictions (with correlation of at least 0.35) over coastal SC locations, especially in Hainan Island and the Pearl River Delta Region; however, rainfall prediction with negative correlation is also found in western SC. This result indicates that most models do not have outstanding skills in rainfall prediction in the western part of SC. The exceptions are the hindcasts from BCC and NCEP, which, however, show negative correlation in eastern or eastern-to-central SC.

For the MME average, it gives the highest skill score as measured by the averaged correlation coefficient over all stations, compared to each individual model. It is noteworthy that the skill of MME average in some western SC locations remains low (not passing 90% significance level), meaning that the MME technique cannot increase the skill in this particular sub domain. This might be related to the low skill of individual models (and probably low variance) in this region; this can strongly affect the skill of the MME average. In other words, if most models fail to simulate the rainfall in the western part of SC, then it is likely that MME will also present a low skill in this area.

## 6.2 Prediction based on statistical downscaling (PP)

After examining the results from the SVD analysis between observed rainfall and various large-scale variables (from observations and models), a suitable predictor had been selected. The time series of the expansion coefficient for precipitation are highly correlated to those for SLP and Z500. In particular, we found that SLP has stronger covariability with the SC regional-scale precipitation. Hence, SLP is chosen as the predictor for statistical downscaling (for details please see section 6.3).

In this section, a PP-based downscaling scheme is developed based on the relationship deduced between the reanalysis SLP data and the observed station rainfall. Repeating the equations described in section 4.2, both the anomalous observational SLP, station precipitation and the rainfall prediction can be expanded as follows:

$$\text{Precipitation}(t, x) \approx \sum_{i=1}^N P_i(x) Q_i(t) \dots \quad (4)$$

$$SLP^{obs}(t, x) \approx \sum_{i=1}^N SLP^{obs}_i(x) R_i(t) \dots \quad (5)$$

$$\text{Predicted Precipitation}(t, x) \approx \sum_{i=1}^N P_i(x) R^{model}_i(t) \dots \quad (6)$$

Here the anomalous SLP( $t, x$ ) and precipitation( $t, x$ ) are normalized to unit standard deviation, and  $SLP^{obs}_i(x)$  and  $P_i(x)$  represent the singular vectors for the

$i^{\text{th}}$  SVD mode. To develop a prediction scheme using model output as the predictor, the expansion coefficient of SLP, i.e.  $R_i(t)$ , is estimated as follows:

$$R^{\text{model}}_i(t) = \frac{SLP^{\text{model}} \cdot SLP^{\text{obs}}_i}{|SLP^{\text{obs}}_i|^2} \dots \dots \dots \quad (7)$$

where  $SLP^{\text{model}}$  represents the anomalous SLP from the dynamical models, and  $SLP^{\text{obs}}_i$  represents the singular vector of observed SLP for the  $i^{\text{th}}$  SVD mode. In other words, the rainfall prediction in SC is obtained by multiplying each singular vector of observed precipitation with  $R^{\text{new}}_i(t)$  which is based on projecting  $SLP^{\text{model}}$  onto the  $i^{\text{th}}$  observed SLP singular vectors. Thus in the PP-based downscaling prediction, the statistical relationship is obtained completely from observations while using model SLP as predictor. Finally, the PP-based rainfall predictions are validated based on a “leave-one-out” cross validation process.

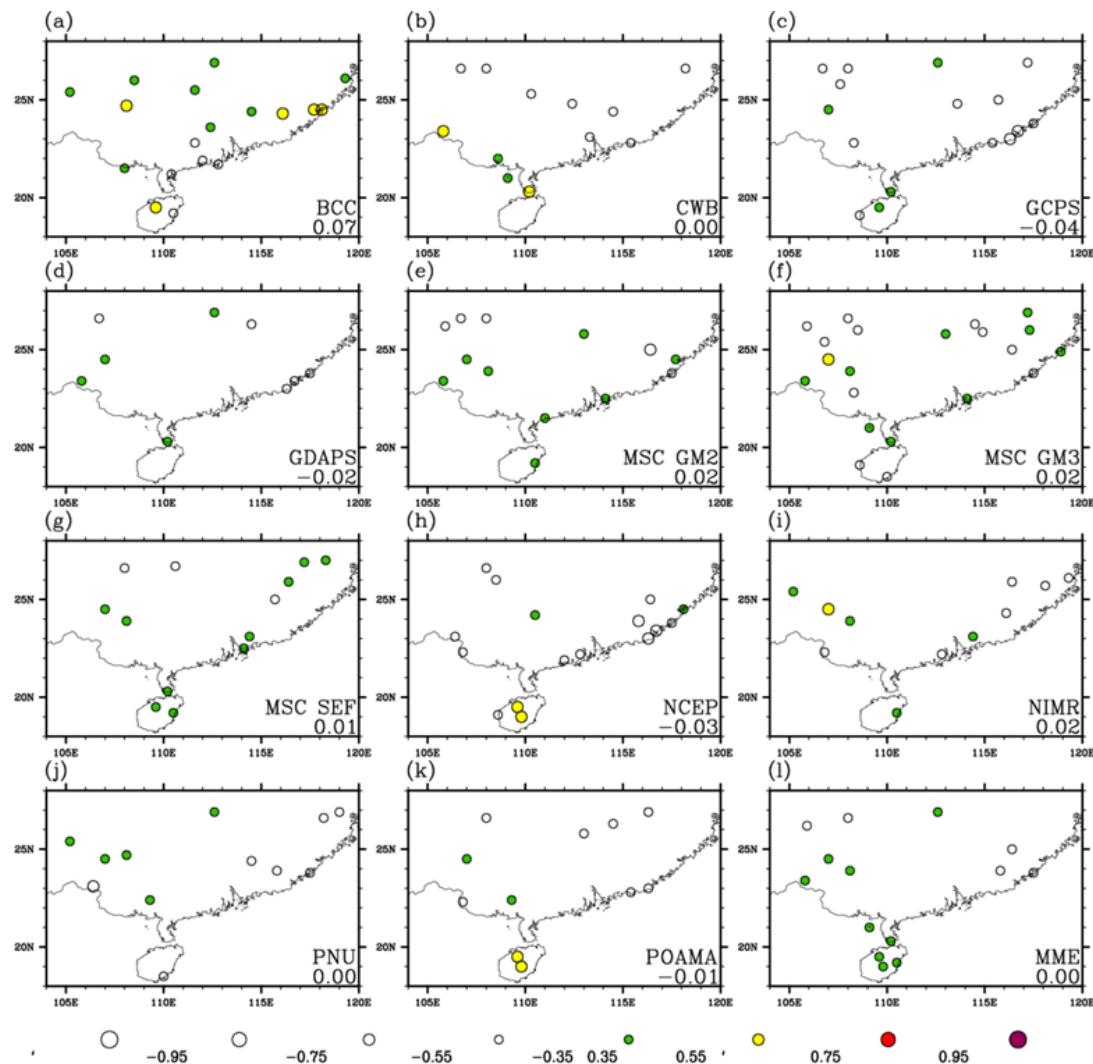


**Figure 6-2.** Same as Figure 6-1, except for predictions based on PP-type statistical downscaling.

The cross-validated correlation coefficients between the PP-based rainfall predictions and observed station rainfall are shown in Figure 6-2. The 89-station averaged correlation is presented at the bottom right of each panel. It shows that the PP-based predicted rainfall performs better than DMO in certain locations, and this is especially the case for BCC and CWB. For BCC, the PP-based downscaling leads to 20 stations over the eastern part of SC with correlation coefficient of at least 0.35, while DMO leads to only 8 stations. Similarly, for CWB, PP downscaling improves the correlation coefficient from about 0.5 to 0.7 in the western part of SC. For the rest of the models, correlation coefficients of ~ 0.35 to 0.55 are obtained, showing improvements over west and northwest SC. The maximum correlation coefficient of 0.7 at some station locations can be reached in three models (CWB, NCEP and POAMA) after downscaling.

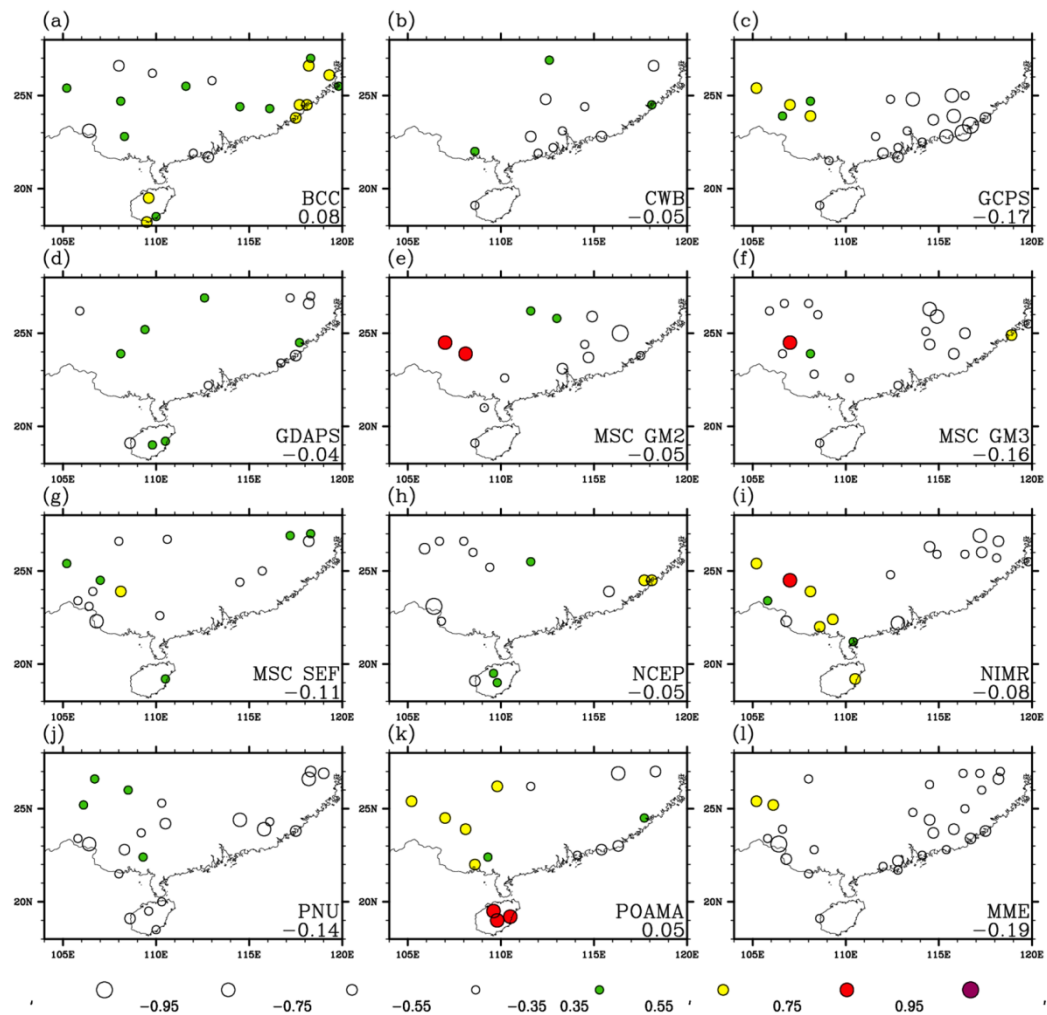


**Figure 6-3. Difference between Figures 6-1 and 6-2.**

Figure 6-3 shows the difference between the correlation coefficients given by DMO and those from the PP-based statistical downscaling. It indicates that the rainfall prediction and the 89-station averaged correlations are slightly improved after applying the PP-based downscaling for BCC and POAMA. In BCC, a remarkable improvement (with difference passing the 90% significance level as estimated using the Fisher transform; see Kenny 1946) over the eastern/coastal part of SC is obtained whereas the correlation coefficient in POAMA in western SC is improved significantly. At the same time, PP-based downscaling decreases the correlation for some stations in western (eastern) SC in BCC (POAMA).

Despite the fact that the PP-based downscaling cannot increase the average correlation over all stations in the other models, it can improve the correlation at same particular locations. For instance, CWB, GCPS, MSC-GM2, MSC-GM3, NIMR and MME give an improvement in the western/in-land part of SC, similar to POAMA. However, stations located in eastern SC see a reduction of the correlation after downscaling.

To conclude, the PP-based statistical downscaling which is based on the observed statistical relationship between station rainfall and SLP can enhance the prediction skill of the seasonal rainfall at certain locations. However, as Carter et al. (1989) suggested, the systematic errors or biases in GCMs may limit the PP-based downscaling results. Therefore, another approach, namely MOS-

based downscaling, is also studied and the results will be discussed in the next section.

### ***6.3 SVD analysis based on observed SC rainfall and model SLP.***

Similar SVD analysis was used to obtain the statistical linkage between the observed precipitation and ***model*** SLP in the MOS-approach. Results for the leading SVD mode are given in Figures 6-4 to 6-6. Figure 6-4 shows the leading precipitation pattern with the model SLP taken from 11 different hindcast models and their MME average. It is worth mentioning that most singular vectors of rainfall compare well with that from the observed rainfall-observed SLP SVD analysis (see Figure 5-8a). Among the results of the twelve different model datasets, nine of them have their pattern correlation with the aforementioned observed singular vector greater than 0.6. In particular, the singular vectors from MSC-GM2 and also the MME average compare very well with observations (with pattern correlation values over 0.9).

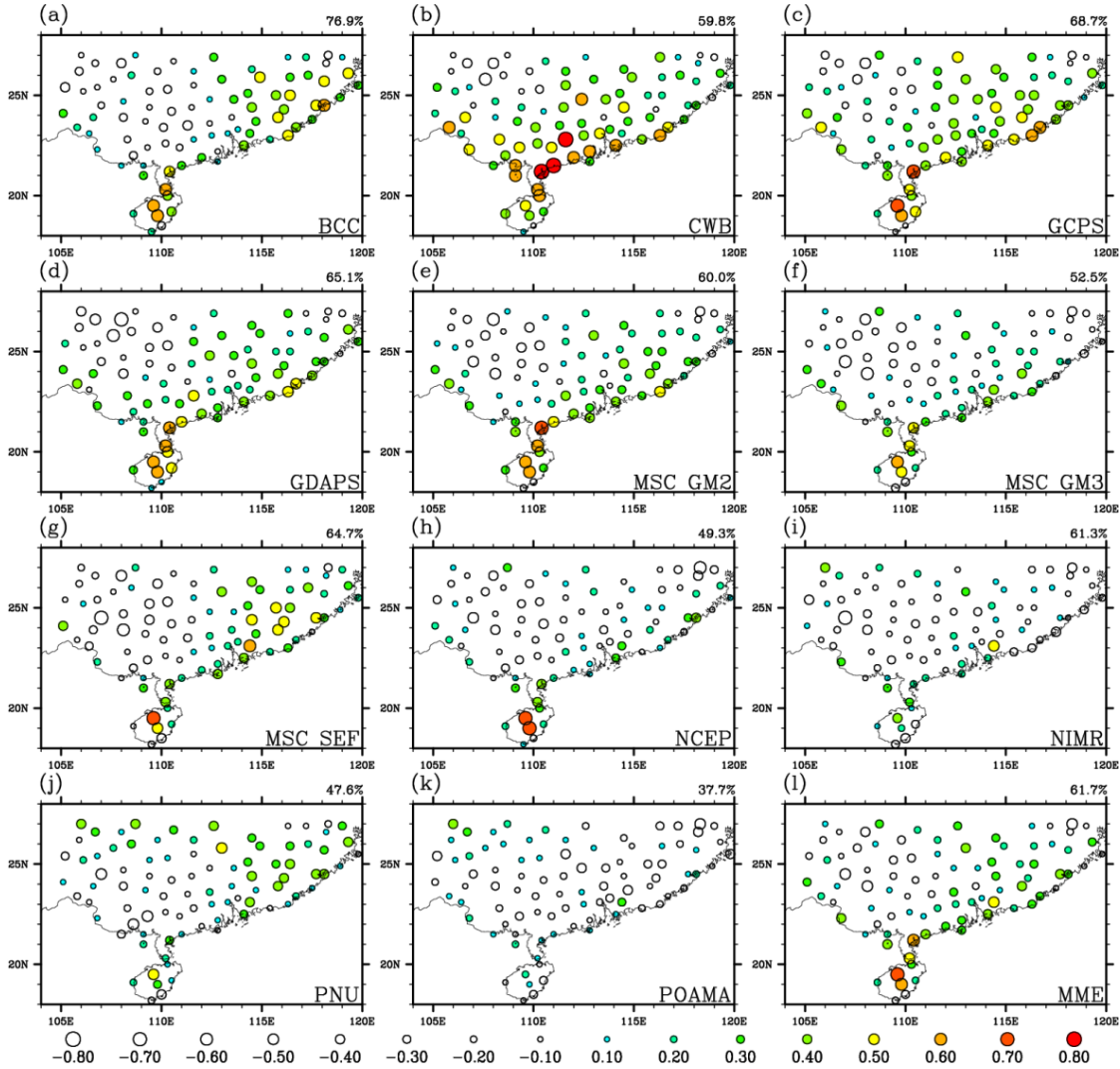


**Figure 6-4. The leading singular vector for precipitation, based on SVD analysis between observed station precipitation and model SLP from (a) BCC, (b) CWB, (c) GCPS, (d) GDAPS, (e) MSC-GM2, (f) MSC-GM3, (g) MSC-SEF, (h) NCEP, (i) NIMR, (j) PNU, (k) POAMA, and (l) the MME average. Upper right of each panel shows the fraction of squared covariance between station precipitation and model SLP explained by this SVD mode.**

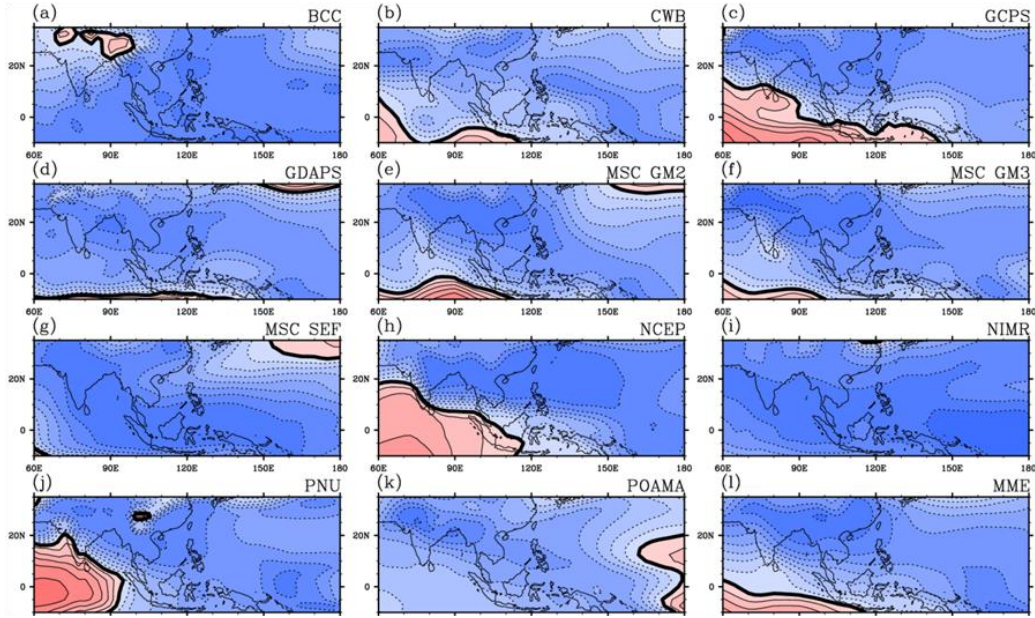


**Figure 6-5. Same as Figure 6-4 except for singular vectors for model SLP.**

From Figure 6-4, it can be seen that most (10 out of 12) models give strong rainfall-model SLP covariability with a pattern of surplus rainfall in coastal to eastern SC, and suppressed precipitation over the north-western part of SC. The only exceptions are NIMR and POAMA. The strong positive anomalous rainfall signal in east SC is missing in NIMR, while eastern/coastal to western/inland dipole structure of rainfall cannot be found in POAMA. The MME average also gives positive (negative) anomalous rainfall in eastern/coastal (west) SC, reflecting the associated leading rainfall pattern for the majority of the models. Notice that the leading SVD mode explains about 50% or more of the squared covariance between observed rainfall and model SLP (with a maximum value of 77%) for all models except POAMA (which accounts 38% of explained squared covariance).

The model SLP patterns for the leading SVD mode are given in Figure 6-5. Generally speaking, the patterns of this SVD mode are consistent with observations (Figure 5-8b), with most models giving a prominent low-pressure anomaly extending from Indochina to SCS. However, details of the SLP pattern vary from model to model. For example, only BCC and PNU can capture the positive anomalous SLP in north western SC; the positive SLP anomaly located over the Indian Ocean is not found in the BCC, MSC-SEF, NIMR and POAMA hindcasts. Furthermore, most models (other than GDAPS, MSC-GM2 and MSC-SEF) encounter difficulties in capturing the positive anomalous pressure in south Japan/western north Pacific. Figure 6-6 gives the corresponding expansion coefficients for this SVD mode. The correlation between the expansion coefficients for station precipitation and model SLP is relatively high for all models (ranging from 0.57 to 0.79).

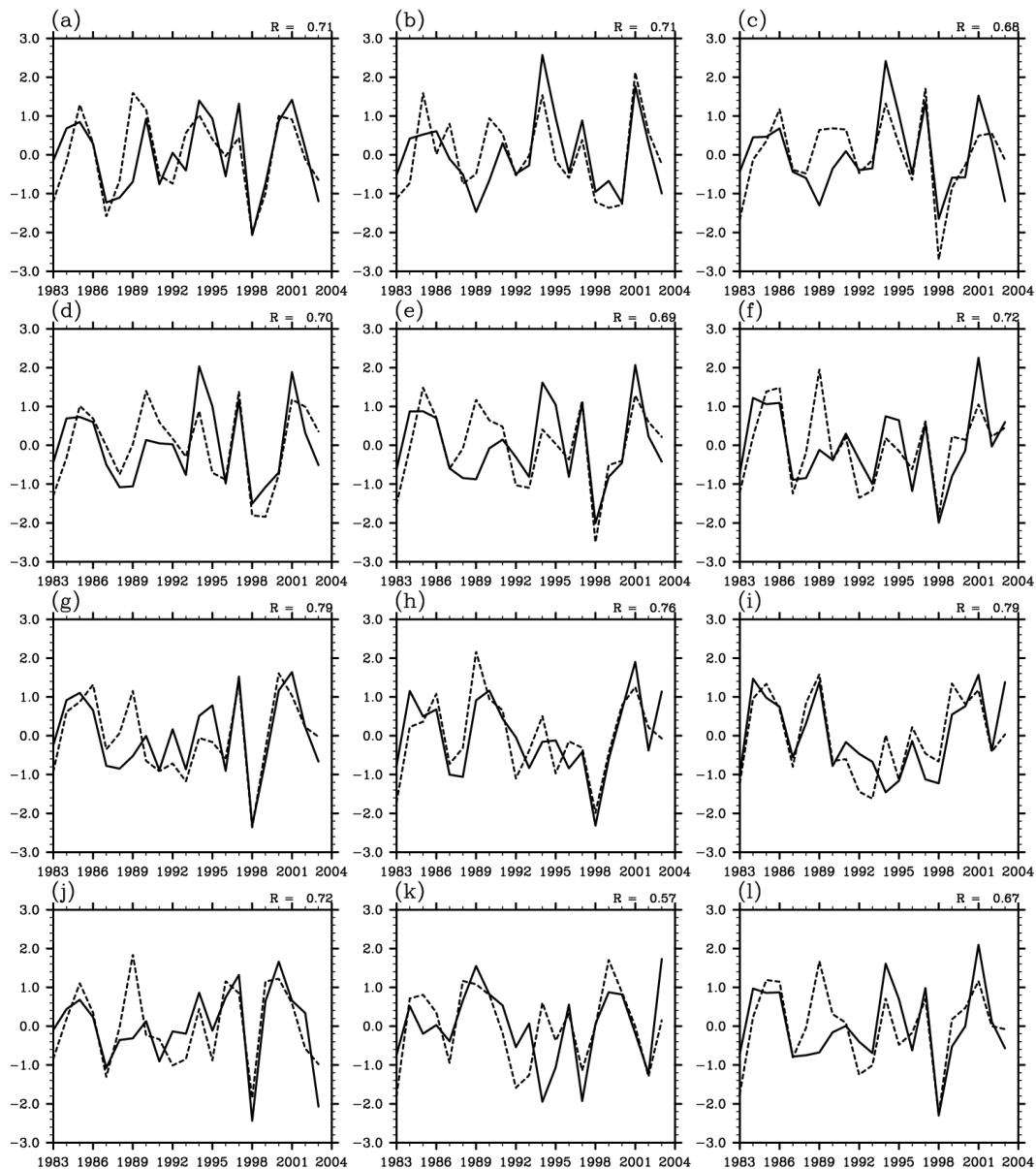


**Figure 6-6. Normalized time series of the expansion coefficient for precipitation (solid line) and model SLP (dashed line) from (a) BCC, (b) CWB, (c) GCPS, (d) GDAPS, (e) MSC-GM2, (f) MSC-GM3, (g) MSC-SEF, (h) NCEP, (i) NIMR, (j) PNU, (k) POAMA, and (l) the MME average, corresponding to the leading SVD mode. Upper right of each panel shows the correlation between the two time series.**

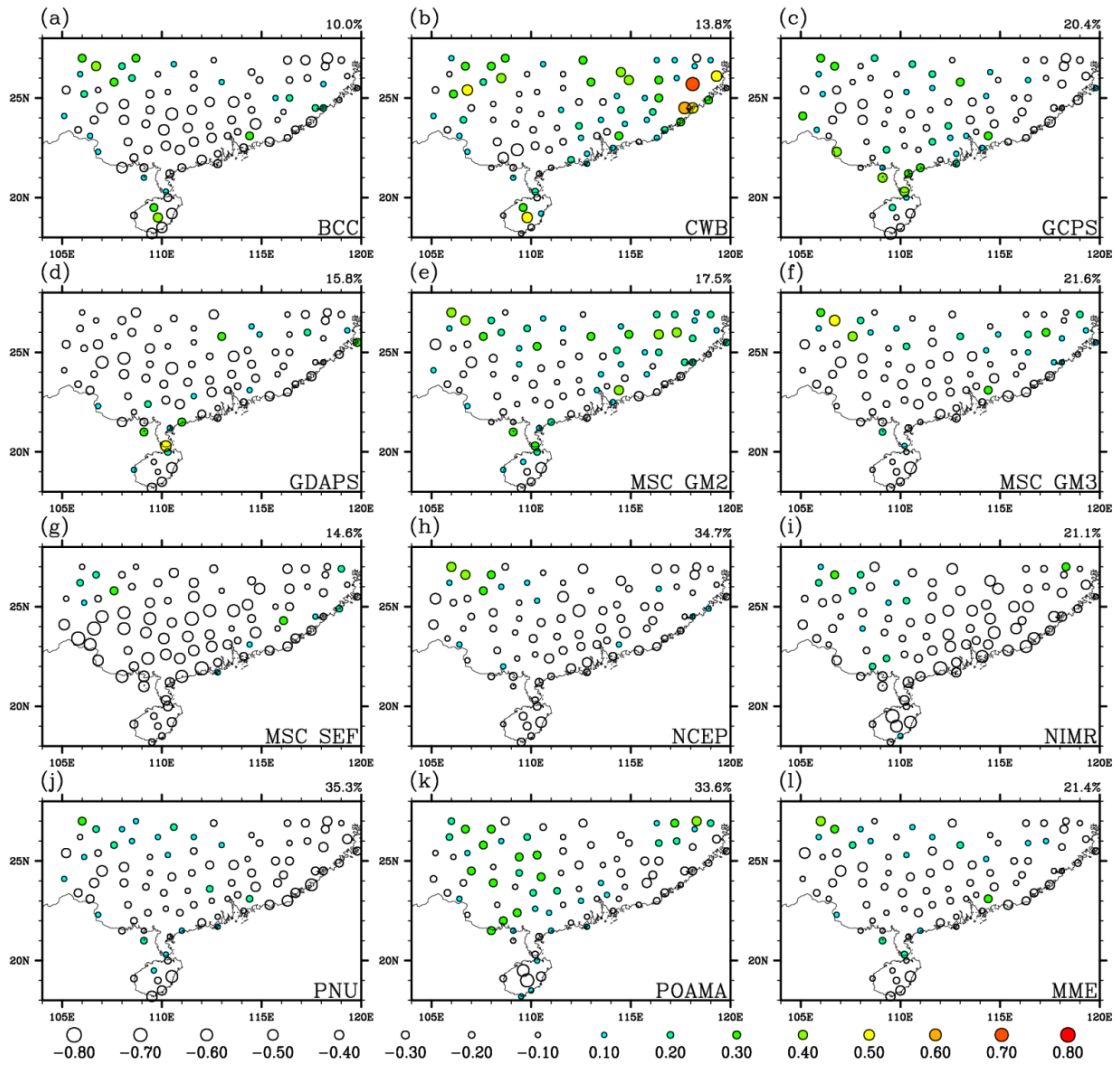


**Figure 6-7. Same as Figure 6-4, except for the 2<sup>nd</sup> SVD mode.**

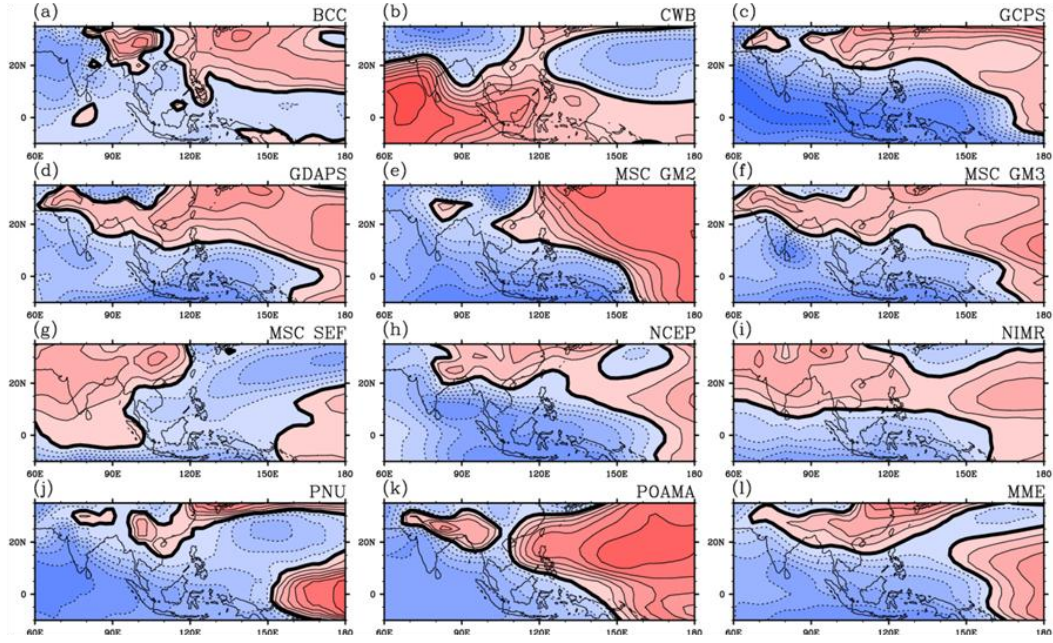


**Figure 6-8. Same as Figure 6-5, except for the 2<sup>nd</sup> SVD mode.**

The rainfall patterns for the second SVD modes are shown in Figures 6-7 to 6-9. We found that BCC, GDAPS, MSC-GM3 and MME average are consistent with observations (see Figure 5-9a); the pattern correlation coefficients between these singular vectors and that based on observed rainfall and observed SLP for the 2<sup>nd</sup> SVD mode are over 0.5. From Figure 6-7, it can be seen that most of the precipitation patterns indicate drier-than-normal conditions within the whole SC, except CWB, GCPs, MSC-GM2 and POAMA. For CWB and MSC-GM2 (GCPs and POAMA), positive anomalous rainfall is found over the northern (western) SC. The MME average gives negative anomalous rainfall in SC, reflecting the rainfall singular vector from a majority of models. From the anomalous SLP for this mode, it can be seen that most models can capture a relative large-scale anomalous high over the Indochina and SC (Figure 6-8). The corresponding expansion coefficients for this mode are given in Figure 6-9.

Moderately high correlation (from 0.51 to 0.79) between the expansion coefficients of station precipitation and model SLP is found for all models.

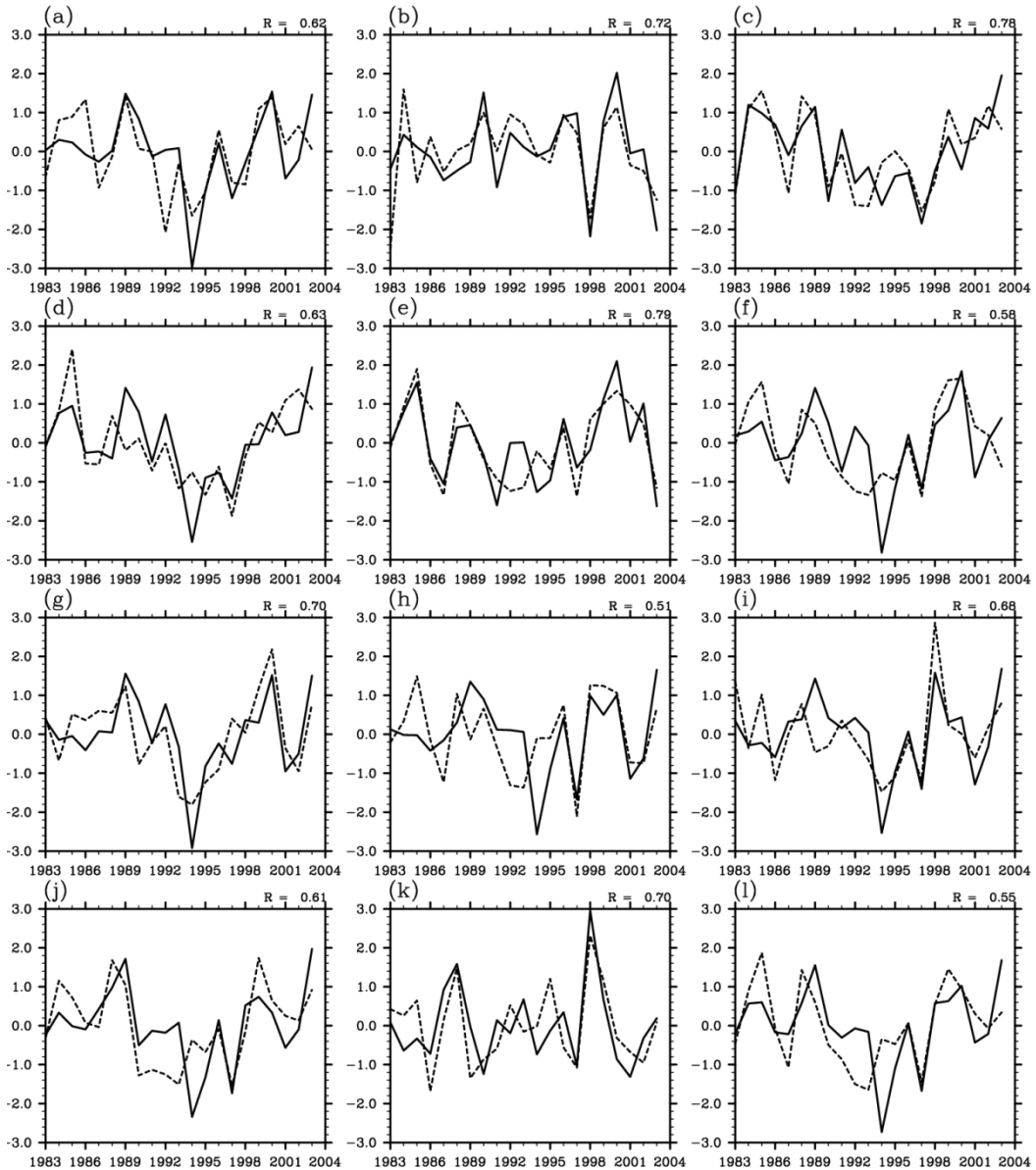


**Figure 6-9. Same as Figure 6-6, except for the 2<sup>nd</sup> SVD mode.**

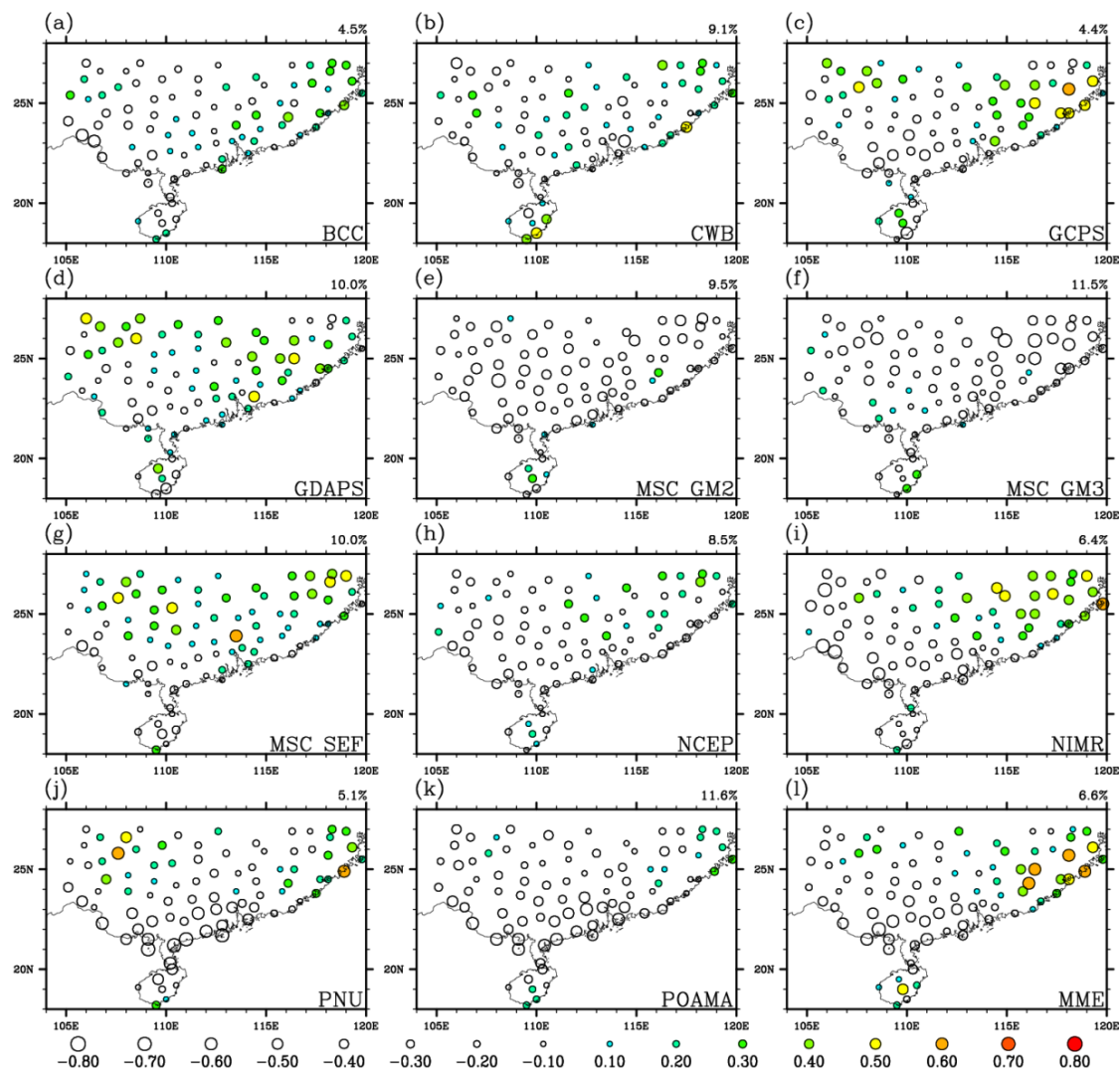


**Figure 6-10.** Same as Figure 6-4, except for the 3<sup>rd</sup> SVD mode.

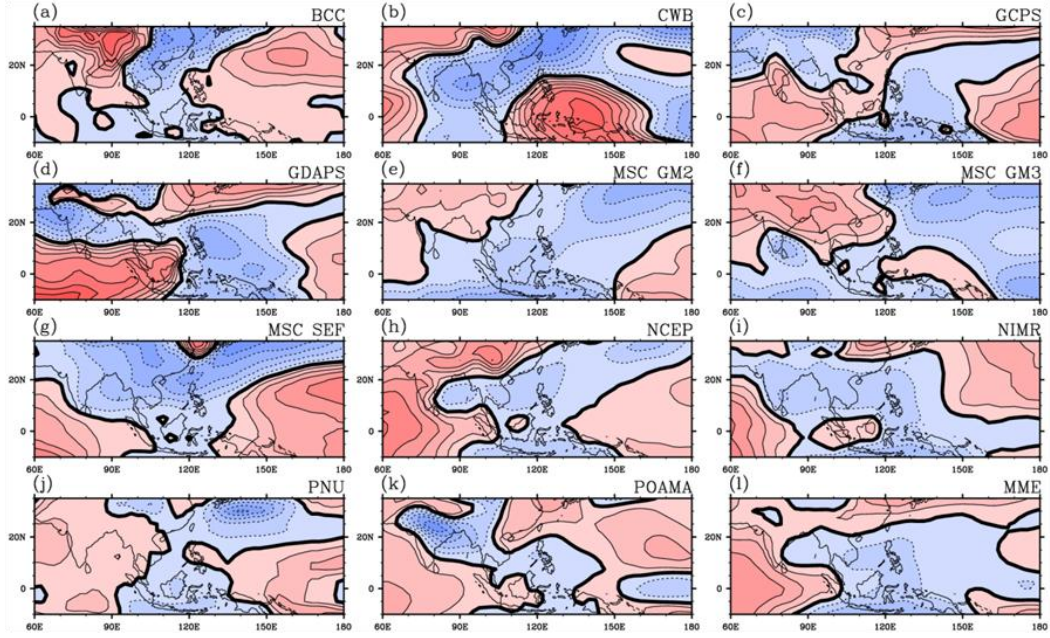


**Figure 6-11. Same as Figure 6-5, except for the 3<sup>rd</sup> SVD mode.**

Figures 6-10 to 6-12 show the results for the third SVD mode. Precipitation patterns (exclusive of MSC-GM2, MSC-GM3 and POAMA) give a northeast-southwest dipole as in observations. The northeast-southwest dipole pattern is consistent with the regional-scale negative anomalous SLP (Figure 6-10). However, it seems that the regional-scale negative SLP anomalies over Taiwan are shifted northward (eastward) in BCC and CWB, (MSC-SEF and PNU), and displaced westward (southward) in GDAPS (NCEP). For those models without a northeast-southwest dipole rainfall pattern, the regional-scale negative SLP signal over the western tip of the subtropical high cannot be captured (Figure 6-11). The correlation between the expansion coefficients of the station precipitation and SLP is again relatively high (about 0.60 to 0.82).

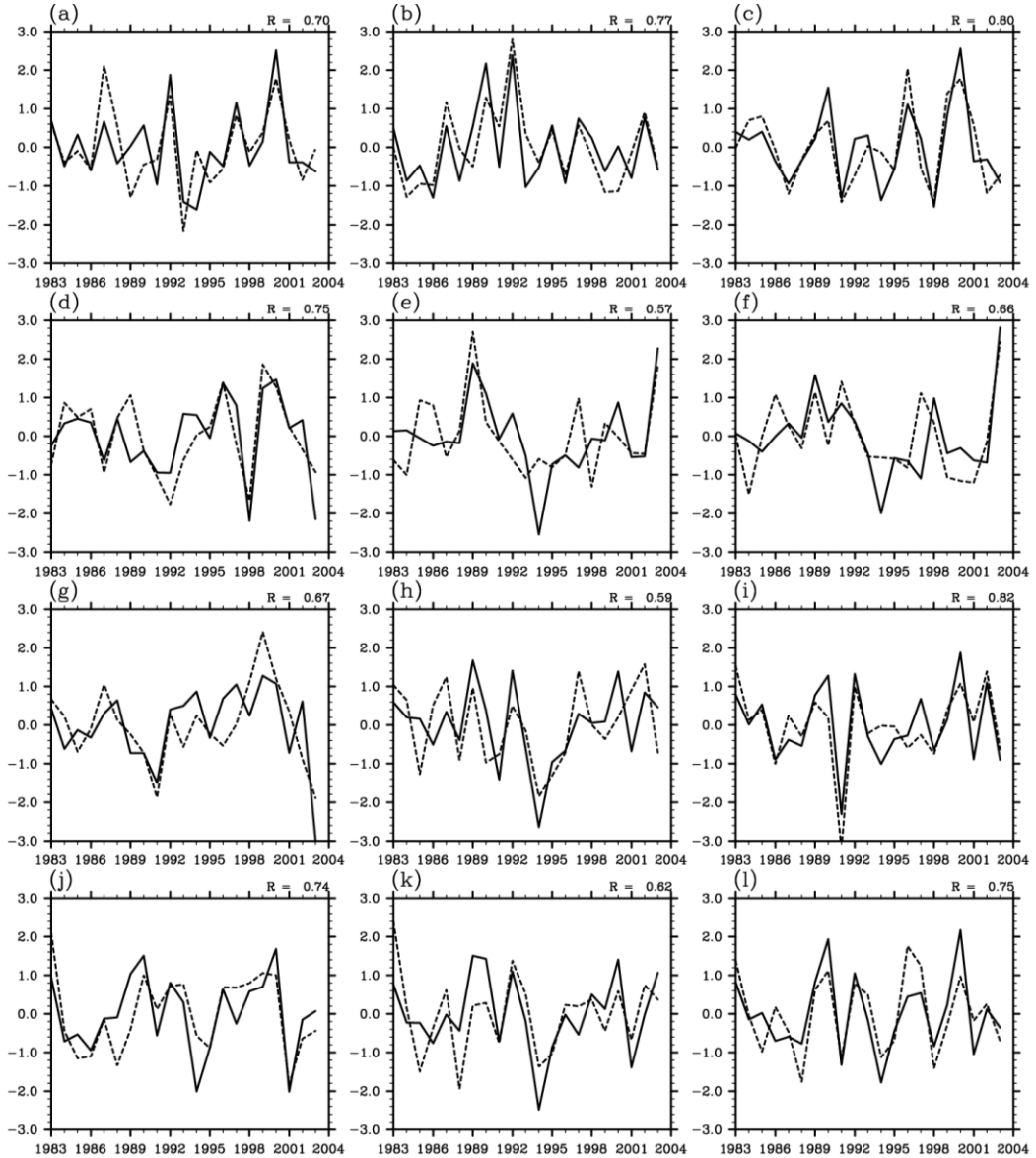


**Figure 6-12. Same as Figure 6-6, except for the 3<sup>rd</sup> SVD mode.**

The same SVD analysis was repeated but based on the observed rainfall and Z500 from **models**. For the leading SVD mode, the singular vectors for rainfall show some similarity to the previous result using model SLP (figures not shown). The correlation between the expansion coefficients of the station precipitation and Z500 is moderately high for all models (ranging from 0.59 to

0.72), but less than their counterparts using SLP for 11 out of 12 models. In addition, the 2<sup>nd</sup> and 3<sup>rd</sup> singular vectors based on model Z500 do not resemble those from the rainfall-observed Z500 analysis (figures not shown).

Overall, a broad agreement is seen between SVD analysis results based on station rainfall and observed SLP, and those by replacing the observed with model SLP. For instance, most model SLP patterns for the leading mode are consistent with that from observations, with negative anomalies covering Indochina to SCS. Moreover, the correlation between the expansion coefficients of station precipitation and model SLP is relatively high for all models for the first 3 leading SVD modes. This indicates that the large-scale circulation variability in models is also linked to that in the observed station precipitation. Finally, based on similar SVD analysis, it was found that the observed rainfall-model Z500 coupling is not as strong as that for the model SLP. The strong rainfall-SLP linkage will be exploited to construct a statistical prediction scheme for SC rainfall, with model SLP outputs as the predictor.

#### 6.4 Predictions based on statistical downscaling (MOS)

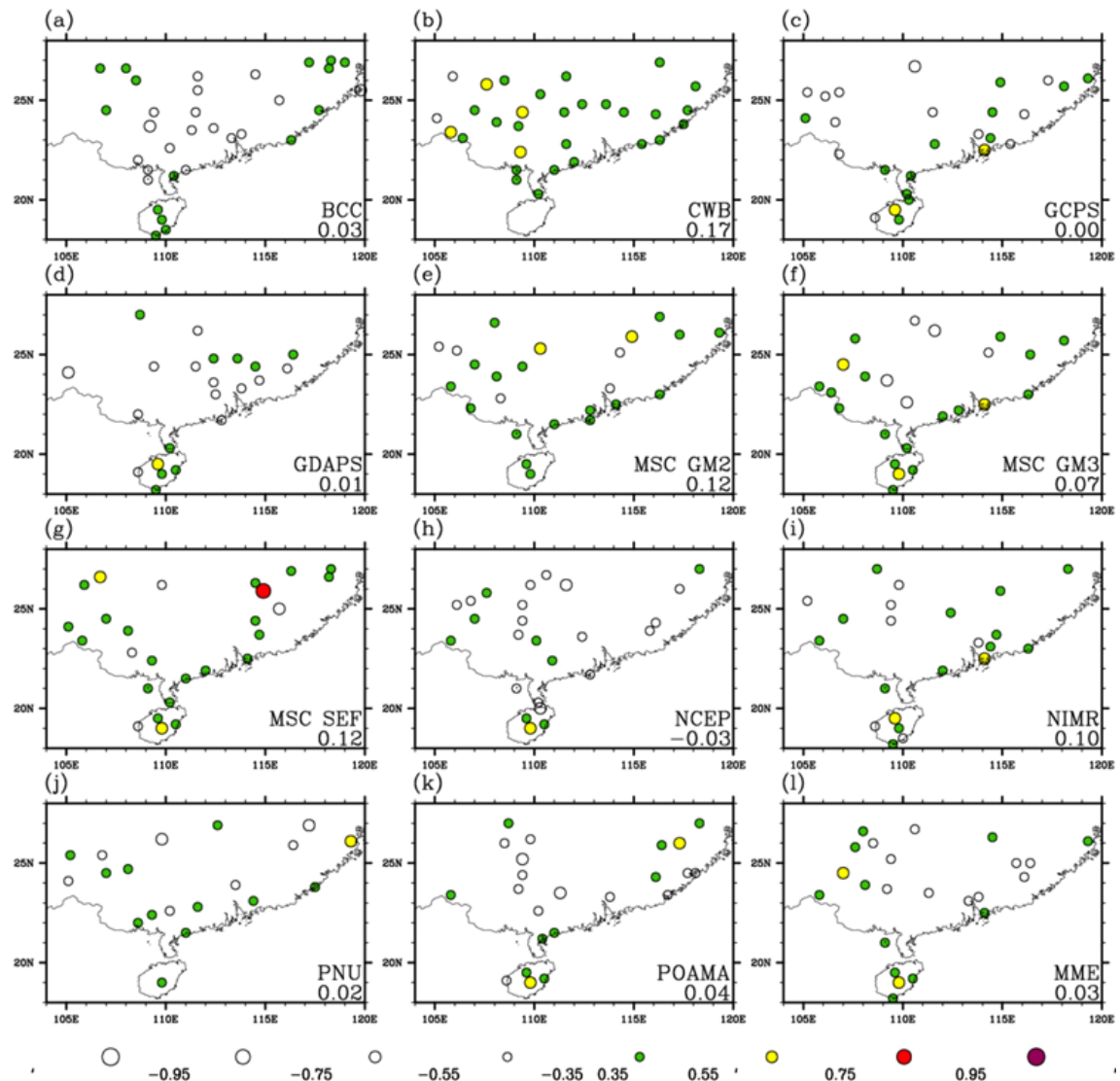


**Figure 6-13.** Same as Figure 6-1 except for predictions based on MOS-type statistical downscaling.

Following the MOS-based downscaling scheme outlined in section 4.2, the station-scale rainfall in SC was predicted with model SLP as predictor. Here the downscaled rainfall predictions were produced and validated based on a “leave-one-out” cross validation framework. Figure 6-13 shows the cross-validated correlation coefficient between the MOS-based downscaling predictions and the station observations, with the correlation coefficient averaged over all stations indicated at the bottom right of each panel. It can be seen that, statistical downscaling performs better than DMO in many locations for most models, especially for BCC and CWB. DMO gives the maximum correlation coefficient of just below 0.3 (see Figures 6-1a and 6-1b); downscaling can increase its value to ~0.6 to 0.7. For MSC-GM2, MSC-SEF and GDAPS, there is an improvement in west SC, with the correlation coefficient reaching 0.6. A similar improvement in the north-western part of SC is also seen in the GCPS, NIMR, PNU, MSC-GM3, POAMA and the MME mean hindcasts whereas the enhancement of the prediction skill is observed in the eastern part of SC in BCC and NCEP.

Meanwhile, stations with negative correlation are still found in central SC in BCC, GDAPS, MSC-GM3, NCEP, POAMA and MME. It indicates that MOS-based downscaling has some limitations in predicting SC rainfall in such a region. More work needs to be done to investigate the limitations and the reasons behind.

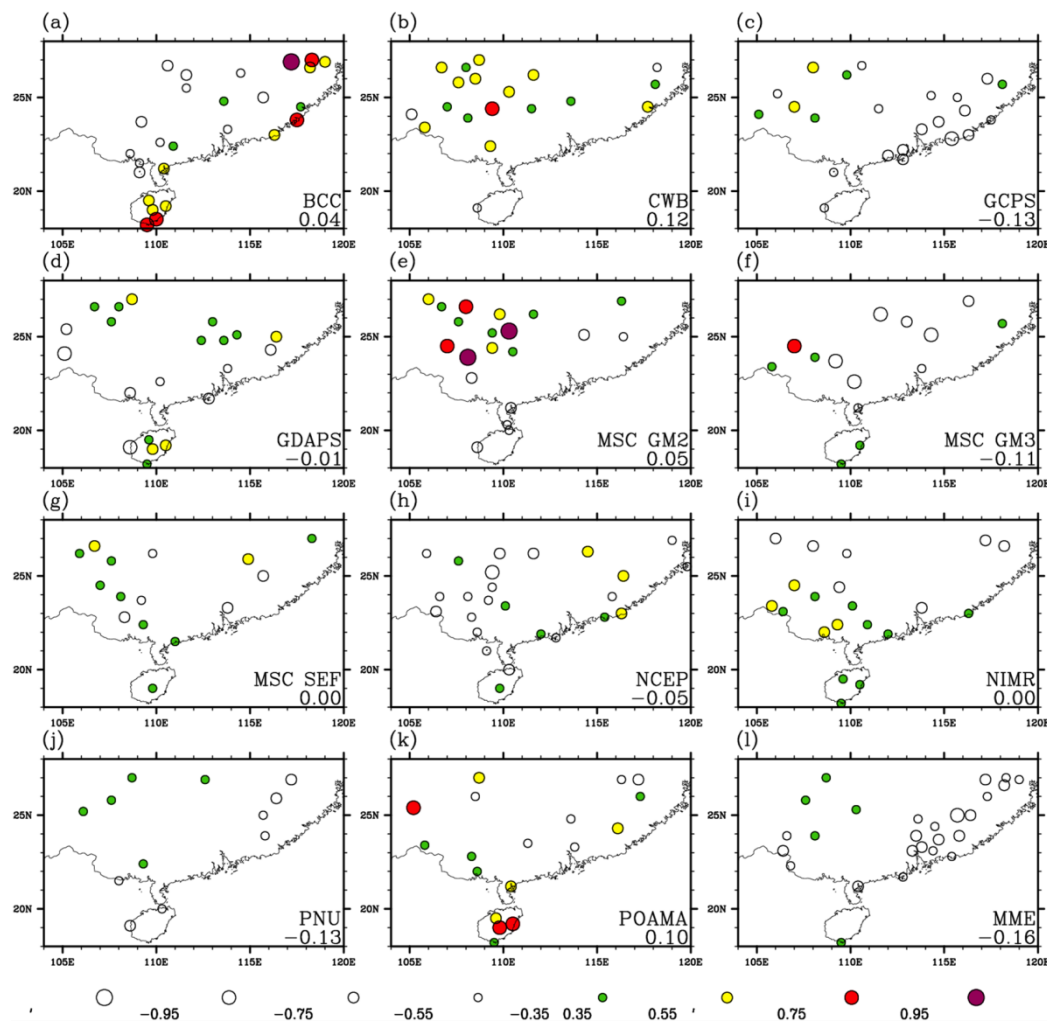


**Figure 6-14. Difference between Figures 6-1 and 6-13.**

The difference between the correlation coefficients given by DMO and those from MOS-based statistical downscaling is shown in Figure 6-14. Despite MOS-based statistical downscaling decreasing the SC rainfall prediction skill in central SC, this statistical downscaling scheme still brings remarkable improvement (which difference passing the 90% significance level) in many locations, especially for BCC, CWB, MSC-GM2 and POAMA. Moreover, the 89-stations averaged correlation for these models is also increased after downscaling. Some models such as GDAPS, MSC-SEF, NCEP and NIMR give an improvement at some locations while the average correlation over all stations decreases slightly.

The MME average shows a similar result with improvement found in western part of SC. Meanwhile, MOS-based rainfall prediction in coastal SC cannot be improved or even worse than DMO. Those correlation differences agree with the results obtained from the PP-based downscaling. Based on the above results, it can be inferred that improvement of the prediction skill due to statistical downscaling scheme is mainly found in two separate regions, namely the western and eastern part of SC. That is consistent with the previous studies showing the impressive improvement in the prediction skills at the locations where DMO performs poorly [Chen *et al.*, 2012]. On average, the positive impact of the statistical downscaling for single-model is larger than that for the MME average.

### **6.5 Improvement in seasonal rainfall variation prediction**

Base on the previous section, the improvement due to statistical downscaling is mainly found in two separate regions, and for two different groups of models. The first group of models is referred to as Type 1 models; for CWB, GCPS, GDAPS, MSC-GM2, MSC-GM3, MSC-SEF, NIMR PNU and POAMA, the rainfall prediction over the western part of SC is improved significantly by downscaling. The second group of models is referred to as Type 2 models; for BCC, NCEP and POAMA, the prediction skill is increased in the eastern and coastal part of SC. Notice that POAMA is classified as both Type 1 and Type 2 model, meaning that its prediction skill is improved in both regions. According to this classification, the ensembles comprising Type 1 and Type 2 models were computed, and the respective rainfall prediction based on DMO and statistical downscaling were also compared.

	Improvement in	Models
Type 1 Model	Western part of SC	CWB, GCPS, MSC-GM2, MSC-GM3, MSC-SEF, NIMR, PNU, POAMA
Type 2 Model	Eastern & Coastal part of SC	BCC, NCEP, POAMA

**Table 6-1. Summary of the Type 1 and Type 2 model.**

Figures 6-15a and 6-15b show the difference between the correlation coefficients for the Type 1 and Type 2 models ensembles based on downscaling and DMO. It is obvious that rainfall variation predictions are mainly improved over northwest SC for the Type 1 model ensemble average; on the other hand,

downscaling improves the prediction skills over the eastern coastal SC for the Type 2 model ensemble average, while some improvement in northwest SC can also be discerned.

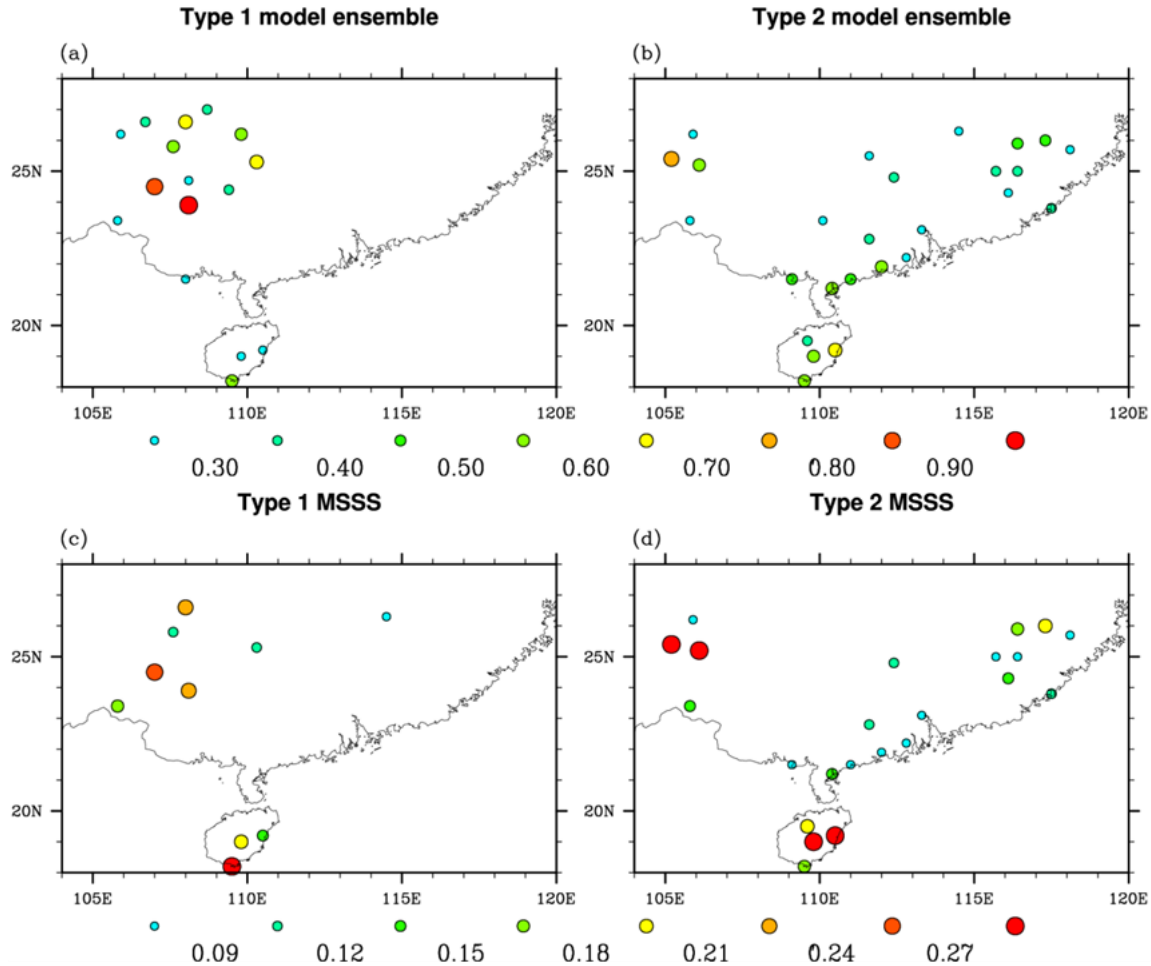


**Figure 6-15. Difference between the temporal correlation coefficients (a,b) and the MSSS (c,d) for DMO and MOS-type downscaled precipitation for Type 1, and Type 2 model ensemble average, respectively.**

Besides temporal correlation coefficients, the Mean Square Skill Score (MSSS; WMO, 2002) is also used to assess the forecast skill of the MOS-based downscaling. Here, MSSS is given by the formula:

$$MSSS = 1 - \frac{MSE_{for}}{MSE_{clim}}$$

where  $MSE_{for}$  and  $MSE_{clim}$  refer to the mean square error of the forecast and model climatology, respectively. MSSS is zero if the forecast error equals the error in the climatology. If MSSS is positive (negative), it indicates that  $MSE_{for}$  is smaller (larger) than  $MSE_{clim}$ . Generally speaking, the MSSS values are also improved over the stations in northwest SC for Type 1 model ensemble and over east SC in the Type 2 model ensemble (Figures 6-15c and 6-15d). The results of temporal correlation coefficient and MSSS show that rainfall prediction based on downscaling can outperform DMO in different locations, depending on the model being considered.

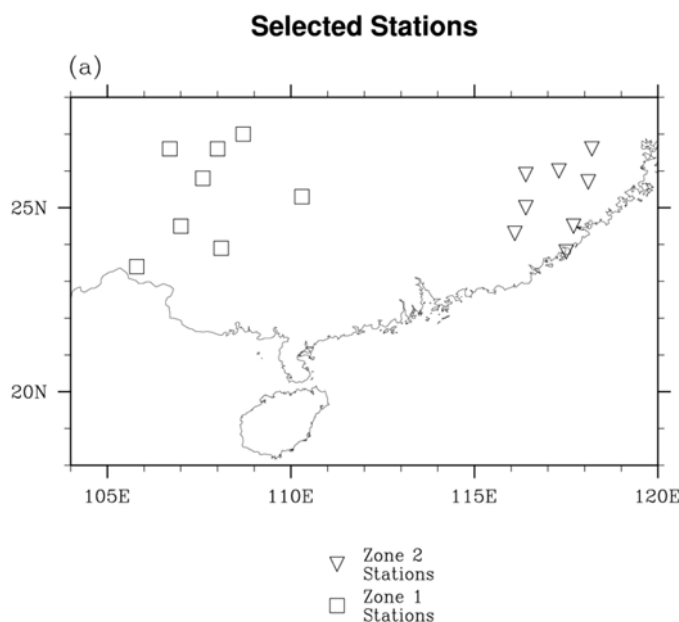


**Figure 6-16. Geographical locations of the selected stations comprising Zone 1 (squares) and Zone 2 (triangles).**

To accentuate the improvement of the seasonal forecasts, results from 16 different stations are grouped into those belonging to Zone 1 or Zone 2, which are located in the western and the eastern part of SC, respectively (Figure 6-16).

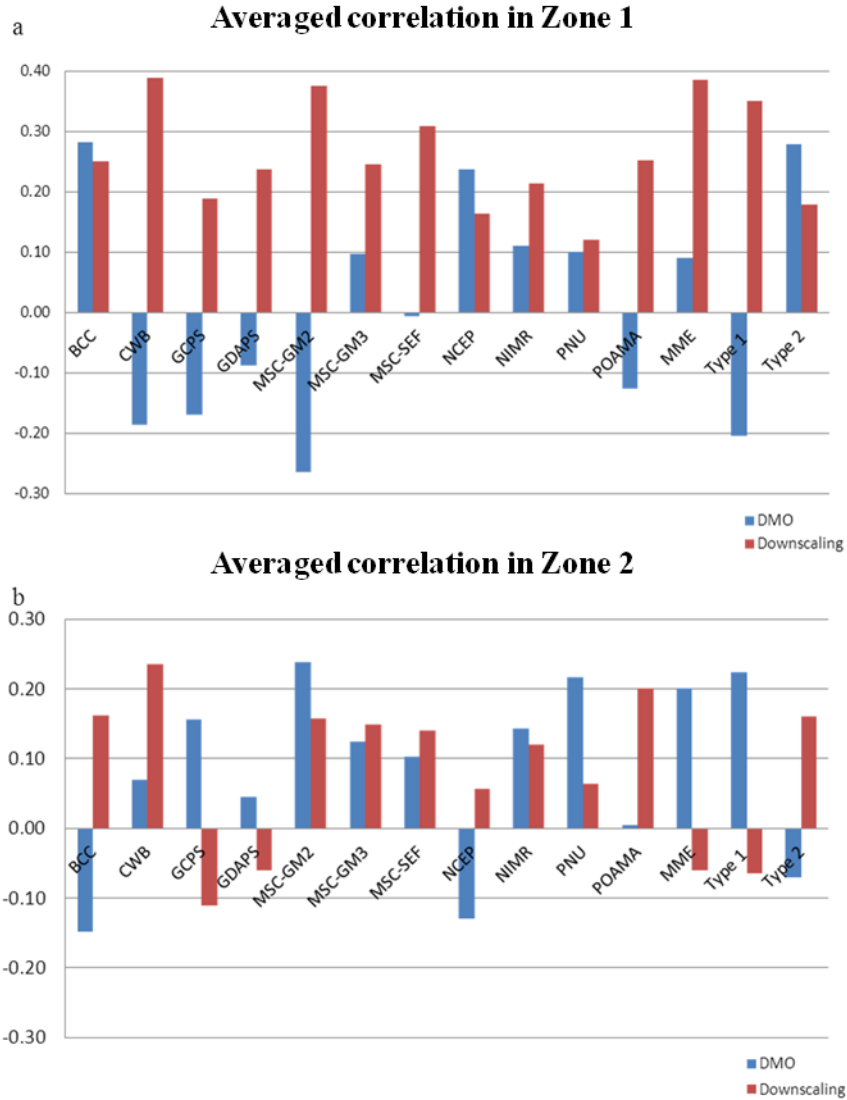


**Figure 6-17. Correlation coefficient for precipitation prediction average over (a) Zone 1, and (b) Zone 2, for different models, the MME average as well as Type 1 and Type 2 ensemble averages based on DMO (blue) and MOS-type statistical downscaling (red).**

Figure 6-17 shows the correlation coefficients between the observed and predicted rainfall averaged over Zone 1 and Zone 2, with results from DMO in blue and statistical downscaling in red. By comparing the blue and red bars in Figure 6-17, it is seen that downscaling exhibits outstanding skills and can improve the prediction for most models (except PNU). Consistent with the previous results, DMO of Type 1 (Type 2) model shows almost no skill for rainfall prediction in Zone 1 (Zone 2). In Zone 1, the correlation coefficient of MME average and of the Type 1 model ensemble average is improved by downscaling from 0.09 to 0.38 and from -0.2 to 0.35 respectively (Figure 6-17a). The result in Zone 2 is shown in Figure 6-17b. Improvement is obtained in 6 out of the 12 models after downscaling. Lastly, we have also compared DMO and downscaling predictions using MSSS. Improvement in MSSS is formed for both Type 1 model (from 0.04 to 0.12) and Type 2 model (from 0.02 to 0.12) after statistical downscaling for seasonal rainfall variation prediction in west and eastern-coastal SC, respectively.

In summary, the MOS-based downscaling scheme for prediction of seasonal rainfall variation in SC is evaluated, improving the prediction skill of the GCMs in different locations. For Type 1 models (CWB, GCPS, GDAPS, MSC-GM2, MSC-GM3, MSC-SEF, NIMR, PNU and POAMA) downscaling can improve predictions over west SC significantly, while for Type 2 models (BCC, NCEP and POAMA) impressive improvement is found in coast-to-eastern SC.

To shed light on how statistical downscaling can give better rainfall prediction in certain sub regions in SC, we further examined the circulation features associated with the recurrent SC rainfall modes in both observations and model simulations. First, both the observed and DMO data are regressed upon the leading, second and third PC time series of SC rainfall from station observations obtained by EOF analysis.

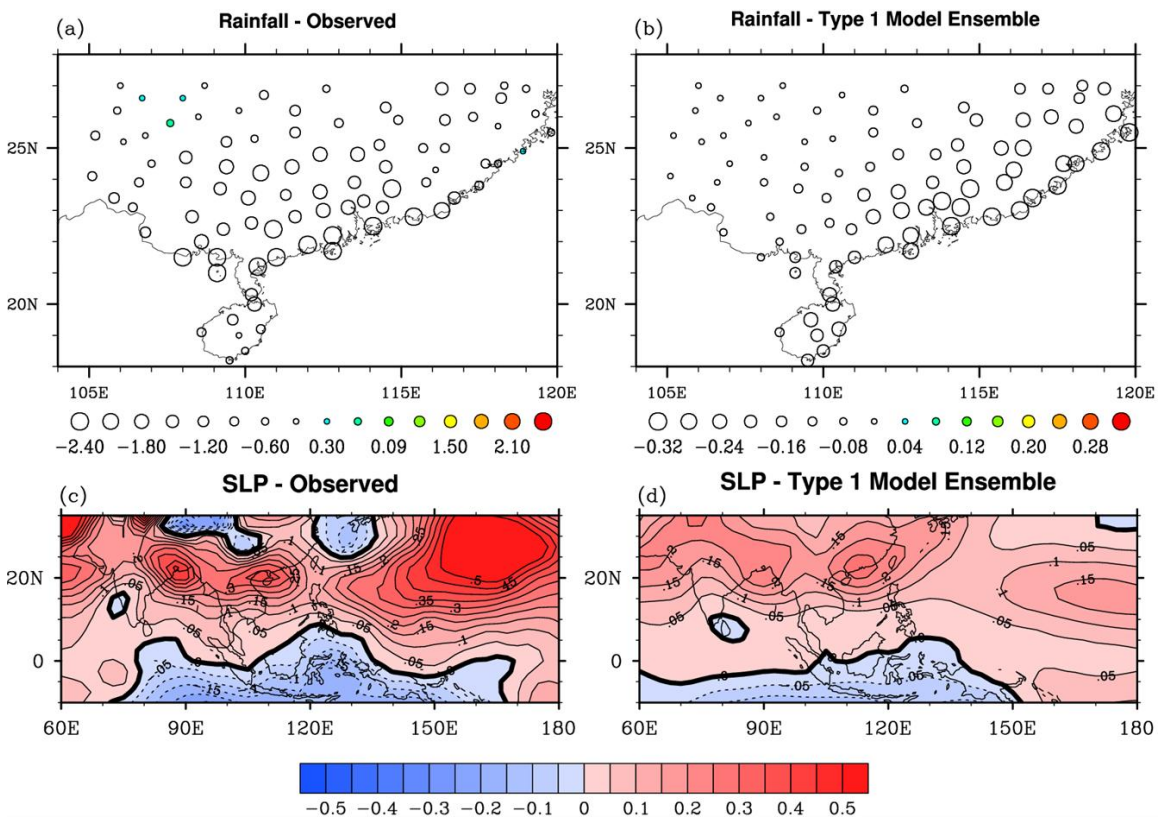


**Figure 6-18. Regression coefficients of the JJA mean (a,b) rainfall (units: mm/day), and (c,d) SLP (contours, in interval of 0.05 hPa) from (a,c) observations and (b,d) Type 1 model ensemble average based on the leading PC of the observed SC station rainfall.**

Figures 6-18a and 6-18b show the regression coefficients based on the leading PC for the observed and the Type 1 model ensemble mean rainfall. A cluster of strong rainfall anomalies are seen over the south-coastal part of SC in the regression map for observed rainfall, which agrees with the leading EOF (Figure 5-1a). This map resembles the second singular vector of SC rainfall, with negative anomalies over most locations in SC. From Figure 6-18b, even though the cluster of strong rainfall anomalies are shifted eastward, Type 1 model ensemble can broadly reproduce the suppressed rainfall pattern over SC. The corresponding regression coefficients for observed and model SLP are given in Figures 6-18c and 6-18d, respectively. It is clear that the negative anomalous rainfall (the leading EOF pattern) is coupled with the positive SLP anomalies at Hainan/Guangxi (Figure 6-18c). Similar positive SLP anomalies are also found in the model ensemble, albeit with a slight eastward shift (Figure 6-18d). Hence, DMO of the Type 1 model is capable of reproducing the rainfall variability in coastal SC (see Figure 6-1).

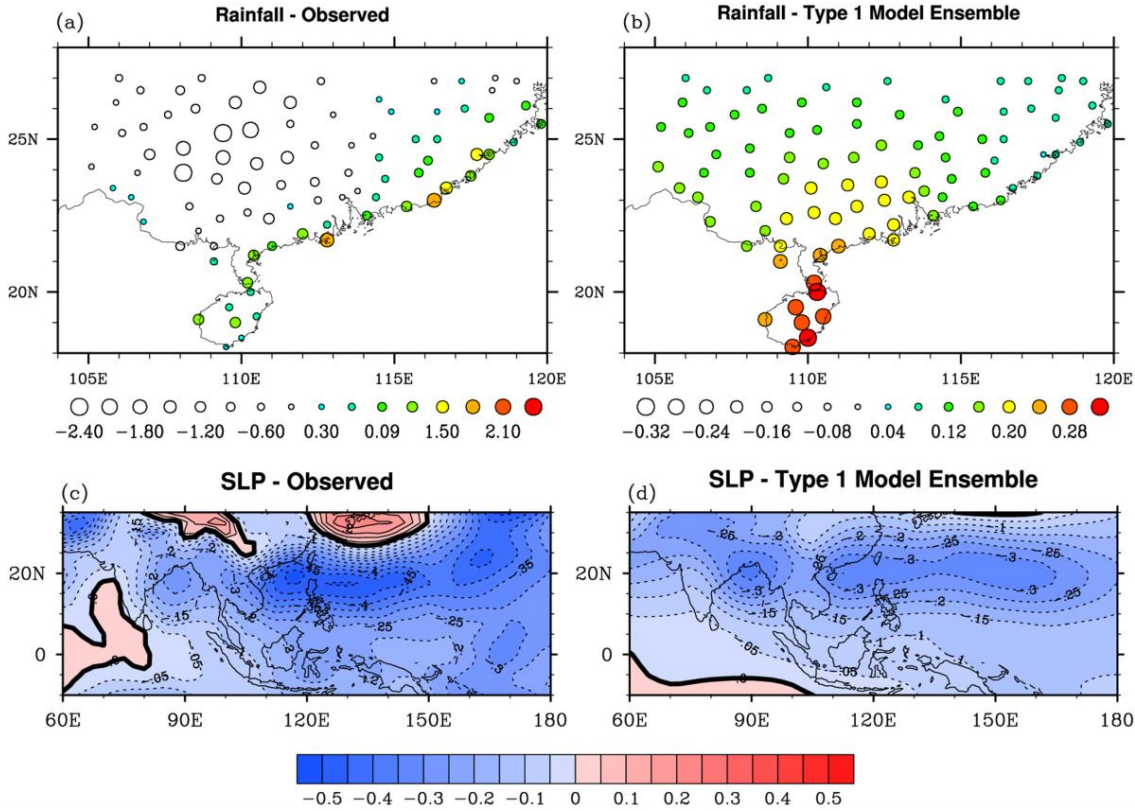


**Figure 6-19. Same as Figure 6-16, except for the second PC.**

Figure 6-19 gives the regression maps for observations and Type 1 model ensemble based on PC2. The observed rainfall pattern is the same as the second EOF (Figure 5-1b). This regression map is also similar to the leading singular vector of SC rainfall (see Figure 5-8a; the pattern correlation between the second EOF and the leading singular vector for rainfall is 0.74). In contrast, this rainfall pattern is not fully captured in the Type 1 model environment. Corresponding to the same temporal variations of the observed second PC, models fail to predict suppressed rainfall in many of the inland SC stations (Figure 6-19b). Figures 6-19c and 6-19d give the corresponding regression coefficients for SLP. It can be seen that the second SC rainfall mode is

associated with a negative centre of action in northern Bay of Bengal and the western north Pacific, and a positive anomaly in southwest China in observations (Figure 6-19c). This latter feature is consistent with the suppressed rainfall over the western to inland part of SC (refer to Figure 6-19a). On the other hand, such a positive SLP anomaly is not reproduced by the Type 1 models ensemble (Figure 6-19d). This is consistent with the fact that the negative rainfall anomaly is missing in these models.

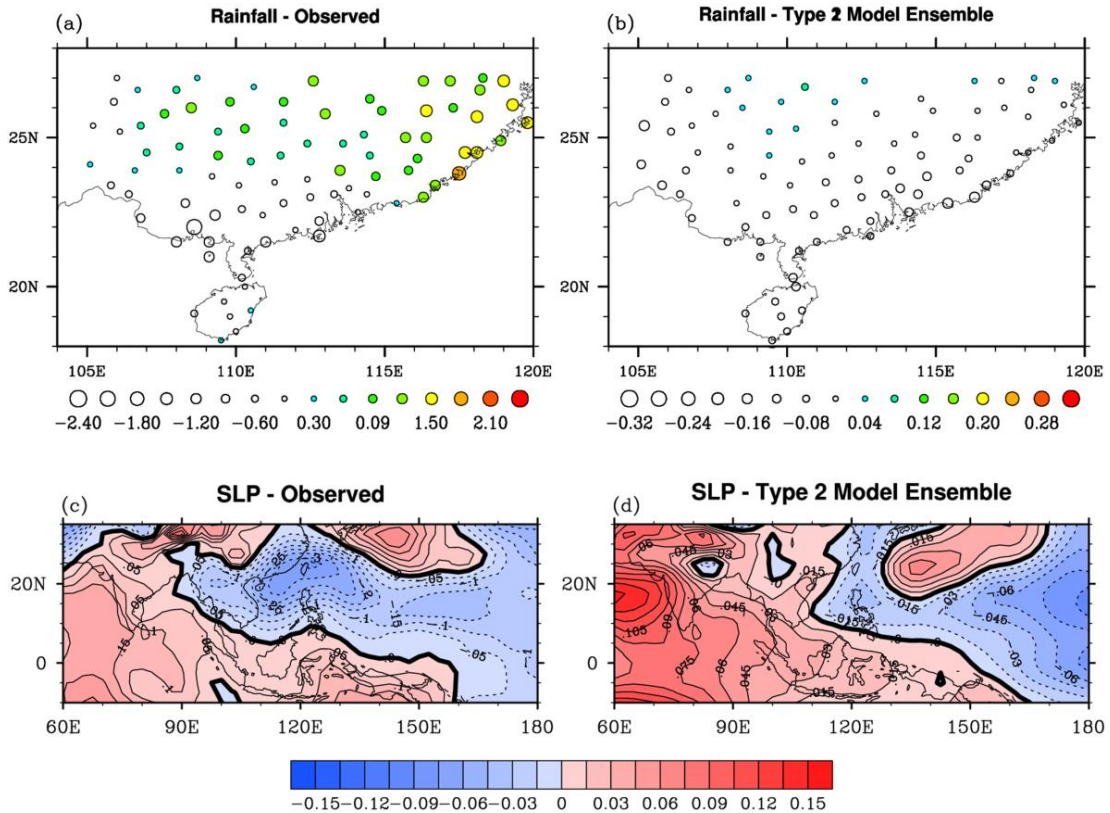


**Figure 6-20.** Same as Figure 6-16 except for regression coefficients based on the third PC for the observations and the Type 2 model ensemble average.

The regression maps based on PC3 are given in Figure 6-20. By construction, this regression pattern for observed rainfall is same as the third EOF shown in Figure 5-1c. Notice that this regression map also resembles the third singular vector of SC rainfall (see Figure 5-10a). It shows a dipole pattern with positive (negative) anomalies over the northeast (southwest) SC. Regression using model rainfall shows that the Type 2 model ensemble has difficulties in capturing this rainfall pattern. In particular, models fail to predict

the surplus rainfall in many stations in the northeast and underestimate the suppressed rainfall signal in southern coastal SC (Figure 6-20b).

From the corresponding regression coefficients for SLP (in Figures 6-20c and 6-20d), it can be seen that the third SC rainfall mode is associated with a large negative anomaly over northeast SC and SCS, and with a anomalous high pressure system over western SC and the western north Pacific (Figure 6-20c). Moreover, the corresponding regression of moisture flux shows that a convergent pattern over northeast SC (Figure 5-7c), thus consistent with the surplus rainfall over the northeast to inland part of SC (see to Figure 6-20a). From the Figure 6-20d, negative SLP anomalies are shifted south-eastward and centred at the Philippines for the Type 2 model ensemble. At the same time, a positive anomaly extends from the Indian Ocean to SCS covering SC. This feature in models is consistent with their failing in reproducing the observed positive rainfall pattern over northeast SC.

To summarize, Type 1 model can well reproduce the rainfall variability in the south-coastal SC, thus giving a more reliable DMO prediction over this area, especially in Hainan Island and the Delta Pearl Region. On the other hand, Type 1 model (Type 2 model) shows systematic errors in the western-inland (eastern-coastal) area of SC, indicating DMO fails to simulate the variation of SC rainfall. MOS-type statistical downscaling helps to correct the models biases, and enhance SC rainfall prediction in these areas.

## **Chapter 7**

### **Summary and discussions**

The interannual SC summertime rainfall variability, as well as its predictability, has been studied by using station observations, NCEP reanalysis-II, and model hindcast experiments from the APCC MME, during the 1983-2003 period. A strong relationship between the SC rainfall variation and the anomalous large-scale circulation in Indo-Pacific region was revealed. Assessment of the hindcast experiments indicates that most models give low (moderate) prediction skill in western (eastern) SC. Finally, two different statistical downscaling (PP- and MOS-based) schemes were constructed and evaluated. Results showed that the statistical schemes could enhance the rainfall prediction skill at the aforementioned locations where models performance is poor.

By using EOF analysis, the dominant patterns of summertime rainfall variation in SC were determined. Moreover, PC time series corresponding to the EOFs were computed. The results showed that (1) rainfall anomalies of the same sign over the SC region are associated with the leading EOF, with large-amplitude signals in the southern coastal locations; (2) an east-west dipole of rainfall anomalies over SC are associated with the second EOF; (3) a dipole with northeast-to-southwest orientation is found for the third EOF.

In order to understand the relationship between the dominant rainfall patterns and the large-scale circulation, regression maps based on the first three

leading PC time series were computed. For the leading EOF, positive large-scale SLP and Z500 anomalies over Bay of Bengal and SC accompany suppressed rainfall signal in the region (when PC1 is positive). There is also divergence of the vertically-integrated moisture flux anomaly associated with this mode. For the second EOF, large-scale negative anomalous SLP and Z500 in SCS and western north Pacific lead to surplus rainfall in eastern/coastal SC (when PC2 is positive). Meanwhile, there is also a positive regional-scale SLP anomaly in northwest SC consistent with the suppressed rainfall there. Convergence of anomalous moisture flux is also found over eastern coastal SC. The southwest-northeast dipole rainfall pattern associated with the third EOF is consistent with the anomalous SLP and Z500 over northeast SC. It is found that anomalous moisture flux converges in the northeastern part of SC, resulting in enhance precipitation in the area (when PC3 is positive).

Results from the regression analysis indicate a strong covariability between the local SC rainfall variation and the large-scale circulation. SVD analysis based on observation was further carried out to reveal the relationship between the rainfall variability in SC and the large-scale flow (based on SLP and Z500) over the Indo-Pacific region. For the leading SVD mode, positive (negative) rainfall anomalies in eastern-coastal (northwestern) SC are associated with negative (positive) anomalous SLP over Hainan and Indochina (northwest SC). Results using Z500 gives a similar rainfall pattern, associated with large-scale negative anomalous Z500 over the northern Indo-Pacific region for the leading mode. For the 2nd SVD mode, the station with negative rainfall signals

over the whole SC domain is related to a positive SLP anomaly covering Bay of Bengal and SC. (Results for the 2nd mode based on Z500 are very similar.) For the 3rd SVD mode, a northeast-southwest dipole of rainfall anomaly over SC is consistent with a negative SLP anomaly with a centre of action over Taiwan. The counterpart of this mode based on Z500 gives a negative signal extending from the western north Pacific to Indochina.

Results from the above SVD analysis can be used to construct a PP-based statistical downscaling scheme with model SLP as predictor. Compared to DMO, the PP-based downscaling has difficulties in improving the rainfall prediction in central SC whereas it improves the prediction in western SC for most models. For other models, improvement is found over the eastern/coastal region of SC. In general, the PP-based downscaling approach can enhance the prediction skill of summertime rainfall at the locations where DMO performs poorly. However, the enhancement of skill brought about by the PP-based downscaling is only modest. This could be related to biases in the model SLP field which is the predictor for PP-based downscaling.

SVD analysis between observed precipitation and model SLP was also carried out, in order to unveil any covariability between observed station rainfall and the simulated large-scale circulation from hindcasts. Results were found to be similar to those using the observed SLP dataset. For the leading SVD mode, expansion coefficients of the station rainfall and model SLP are highly correlated for all models (ranging from 0.6 to 0.8). For the second and the third mode, there is still a strong resemblance between the corresponding singular

vectors from the observational and model results. Overall, these suggest a strong covariability is also present between the observed SC rainfall and model SLP over the Indo-Pacific region from the hindcast data. The same SVD analysis was repeated but based on observed rainfall-model Z500. However, singular vectors for model Z500 bear less resemblance to their observational counterparts, compared to the aforementioned SVD results for SLP.

After establishing the relationship between observed station rainfall and the large-scale circulation from models, a MOS-based statistical scheme for summertime rainfall prediction in SC was then constructed with SLP as predictor, based on the above SVD analysis. Results from cross-validated MOS-based statistical downscaling were compared to those from DMO. In general, DMO is skilful over southern coastal locations but poorer skill is found in the inland region, especially over the western part of SC. Although the MOS-based statistical downscaling scheme decreases the prediction skill in central SC, it still outperforms DMO in western SC for most models; in eastern coastal SC, MOS-based downscaling also gives better performance for some models.

According to the areas in which MOS downscaling can improve the rainfall prediction, models are classified into two categories: for the Type 1 models (including CWB, GCPS, GDAPS, MSC-GM2, MSC-GM3, MSC-SEF, NIMR PNU and POAMA), prediction over the western part of SC is improved significantly, while for the Type 2 models (including BCC, NCEP, and POAMA) the prediction skill is increased in eastern SC by MOS-based statistical downscaling. Further analysis showed that, despite models being able to

reproduce the basin-scale circulation patterns associated with the recurrent SC rainfall modes, they have difficulties in capturing regional details of the circulation. (1) Type 1 models have skill in reproducing the circulation in the western north Pacific. However, these models cannot capture the anomalous circulation pattern over western SC to Indochina which can be important for the local rainfall variation. (2) Even though the anomalous circulation can be captured in the Type 1 (Type 2) models, the location is shifted eastward (southward) to SCS (the Philippines). These features appear to be the model biases or the systematic errors that result in erroneous rainfall predictions. MOS statistical downscaling helps to correct these biases and hence improves the rainfall prediction. Overall, MOS-based statistical downscaling can map the large-scale SLP patterns on local rainfall variability, thereby tapping the source of predictability from the large-scale circulation signals to enhance the prediction skill.

From rainfall prediction based on DMO, it was found that MME mean gives the highest skill score in terms of 89-station averaged correlation, compared to all individual models. The skill of the MME average strongly depends on the performance of the individual models and their variances. How different combinations of models can affect the performance of the MME average, and also the criteria of model selection for the MME mean should be further examined.

In this study, the time expansion coefficients of the predictand of particular SVD mode are directly replaced by that of the predictor for the

corresponding mode while constructing the statistical downscaling scheme (i.e. predicted rainfall  $\approx \sum_{i=1}^N P_i(x) R_i(t)$ ; where  $P_i(x)$  is singular vector of predictand and  $R_i(t)$  is the time expansion coefficients of predictor for  $i^{\text{th}}$  SVD mode). This estimation is exact as long as the time expansion coefficients of predictor and those of the predictand are perfectly correlated. However, if they are not perfectly correlated, a re-estimation of the predictor time series is then necessary. In general, the rainfall can be estimated from  $\sum_{j=1}^N P_j(x) R_j(t) b_{ij}$ , where the coefficients  $b_{ij}$  relate the different precipitation and SLP expansion coefficients. The values of  $[b_{ij}]$  can be estimated by multiple linear regressions (MLR) (Tippet et al., 2008). After the new predictor time series is estimated, the same statistical downscaling prediction is repeated, and then validated. The results from downscaling prediction based on the new estimates of predictor time series are very similar to those presented in this study for individual models. The method with MLR, however, gives better performance for the MME mean (see Tung et al., 2013). The use of different downscaling methods for, as well as the dependence of their skills on the different model data being used would be other topics for further investigations.

We found that most models have considerable skill in capturing the WNPSM activity. In view of its strong linkage with the circulation over SC, it seems likely that WNPSM is one of the major factors determining the predictability of SC summertime rainfall. More work needs to be done to

understand the role of WNPSM on the Asian monsoon rainfall and its predictability.

Hindcast experimental datasets from GCMs were utilized to construct a statistical downscaling scheme for SC rainfall prediction during JJA. It provides a good capability for studying the performance of downscaling methods. As compared with the model output, statistical downscaling can lead to better prediction skill in some locations in SC.

Finally, the statistical downscaling prediction is obtained based on the statistical relationship established between the station rainfall in SC and model variables such as SLP, Z500 or SST. In other words, the stationarity of the statistical relationship is important for the success of the downscaling scheme. However, such relationship may experience interdecadal change in the future and this might affect the downscaling result (Wu et al, 2012). In order to address the issue of possible non-stationarity, one can make use of the most up-to-date historical model predictions (say for the last 30 years up to the very last year) to derive statistical relationships between variables using SVD analysis. By updating the statistical relationship based on the latest available data, one can minimize the impact due to (possible) decadal change of relationship between the local rainfall and the large-scale circulation.

### **Bibliography**

- Ajayamohan, R. S. (2007), Simulation of South-Asian summer monsoon in a GCM, *Pure Appl. Geophys.*, *164*, 2117–2140.
- Back, S. K., J. H. Ryu, and S. B. Ryoo (2002), Analysis of the CO<sub>2</sub> doubling experiment using METRI AGCM part I: The characteristics of regional and seasonal climate response, *J. Korean Meteor. Soc.*, *38*, 465–477.
- Bjornsson, H. and S. A. Venegas (1997), A manual for EOF and SVD analyses of climatic data, Report No 97–1, *Department of Atmospheric and Oceanic Sciences and Centre for Climate and Global Change Research, McGill University*, 52.
- Bretherton, C. S., C. Smith, and J. M. Wallace (1992), An intercomparison of methods for finding coupled patterns in climate data, *J. Clim.*, *5*, 541–559.
- Brunet, N., R. Verret and N. Yacowar (1988), An objective comparison of model output statistics and perfect prog systems in producing numerical weather element forecasts, *Wea. Forecasting*, *3*, 273–283.
- Cavazos, T. (1999), Large-scale circulation anomalies conductive to extreme precipitation events and derivation of daily rainfall in Northeastern Mexico and Southeastern Texas, *J. Clim.*, *12*, 1506–1523.
- Chen, H.-P., J.-Q. Sun, and H.-J. Wang (2012), A statistical downscaling model for forecasting summer rainfall in China from DEMETER hindcast datasets, *Weath. & Fore.*, *27*, 608–628.

- Chu, J.-L., H. Kang, C.-Y. Tam, C.-T. Chen, and C.-K. Park (2008), Seasonal forecast for local precipitation over northern Taiwan using statistical downscaling, *J. Geophy. Res.*, 113, doi:10.1029.2007JD009424.
- Chu, J.-L. and P.-S. Yu (2010), A study of the impact of climate change on local precipitation using statistical downscaling, *J. Geophy. Res.*, 115, doi:10.1029/2009JD012357.
- Ding, Y., Y. Ni, X. Zhang, W. Li, M. Dong, Z.-C. Zhao, Z. Li, and W. Shen (2000), Introduction to the short-term climate prediction model system, *China Meteorological Press, Beijing, China*, 500 (in Chinese).
- Ding, Y., Z. Wang and Y. Sun (2008), Inter-decadal variation of the summer precipitation in East China and its association with decreasing Asian summer monsoon part I: observed evidences, *Int. J. Climatol.* 28, 1139–1161.
- Doblas-Reyes, F. J., M. Déqué and J.-P. Piedelievre (2000), Multi-model spread and probabilistic seasonal forecasts in PROVOST, *Q. J. R. Meteorol. Soc.*, 126, 2069–2087.
- Feng, S. and Q. Hu (2004), Variations in the teleconnection of ENSO and summer rainfall in northern China: A role of the Indian summer monsoon, *J. Clim.*, 17, 4871–4881, doi:10.1175/JCLI-3245.1.
- Fennessy, M. J., L. Marx and J. Shukla (1985), General circulation model sensitivity to 1982–83 equatorial Pacific sea surface temperature anomalies, *Mon. Wea. Rev.*, 113, 858–864.
- Giorgi, F. (1990), Simulation of regional climate using a limited area model nested in a general circulation model, *J. Clim.*, 3, 941–963.

- Gong, D.-Y. and C.-H. Ho (2003), Arctic oscillation signals in the East Asian summer monsoon, *J. Geophys. Res.*, *108*, D2, 4066, doi:10.1029/2002JD002193.
- Gong, D.-Y., J. Yang, S.-J. Kim, Y.-Q. Gao, T.-J. Zhou and M. Hu (2011), Spring Arctic oscillation-East Asian summer monsoon connection through circulation changes over the western North Pacific, *Clim. Dyn.*, *37*, 2199–2216, doi:10.1007/s00382-011-1041-1.
- Grotch, S. L. and M. C. McCracken (1991), The use of general circulation models to predict regional climate change, *J. Clim.*, *4*, 286–303.
- Guan, Z. and T. Yamagata (2003), The unusual summer of 1994 in East Asia: IOD teleconnections, *Geophys. Res. Lett.*, *30*, 10, 1544, doi:10.1029/2002GL016831.
- Huang, R.-H. and Y.-F. Wu (1989), The Influence of ENSO on the summer climate change in China and its mechanism, *Adv. Atmos. Sci.*, *6*, 1, 21–32.
- Kanamitsu, M., W. Ebisuzaki, J. Woollen, S. K. Yang, J. J. Hnilo, M. Fiorino, and G. L. Poter (2002), NCEP-DOE AMIP-II reanalysis (R-2), *Bull. Amer. Meteor. Soc.*, *83*, 1631–1643.
- Kang, I.-S., J.-Y. Lee, and C.-K. Park (2004), Potential predictability of a dynamical seasonal prediction system with systematic error correction, *J. Clim.*, *17*, 834–844.
- Klein, W. H., B. M. Lewis, I. Enger (1959), Objective prediction of five day mean temperature during winter, *J. Meteor.*, *16*, 672–682.
- Kenny, David A (1946), Statistics for the social and behavioural sciences, *Library of Congress, Canada.*

- Krishnamurti, T. N., C. M. Kishtawal, T. E. LaRow, D. R. Bachiochi, Z. Zhang, C. E. Williford, S. Gadgil and S. Surendran (1999), Improved weather and seasonal climate forecasts from multimodel superensemble, *Science*, 285, 1548–1550.
- Li, C. and M. Mu (2001), The influence of the Indian Ocean dipole on atmospheric circulation and climate, *Adv. Atmos. Sci.*, 18, 5, 821–843.
- Li, T. and B. Wang (2005), A review on the western North Pacific monsoon: synoptic-to-interannual variabilities, *TAO*, 16, 2, 285–314.
- Liou, C. S., J. H. Chen, C. T. Terng, F. J. Wang, C. T. Fong, T. E. Rosmond, H. C. Kuo, C. H. Shiao, and M. D. Cheng (1997), The second generation global forecast system at the central weather bureau in Taiwan, *Wea. Forecasting*, 3, 654–663.
- Liu, Y., K. Fan, and H.-J. Wang (2011), Statistical downscaling prediction of summer precipitation in Southeastern China, *Atmos. Ocean. Sci. Lett.*, 4, 173–180.
- Lorenz, E. N. (1956), Empirical orthogonal functions and statistical weather prediction, *Massachusetts Instit.Tech., Dept. of Meteor.*, 1, 1, 52.
- Maurer, Ed. (2009), Translating global models to the local scale, OCCRI workshop, Scenarios of future climate.
- Maraun, D., F. Wetterhall, A. M. Ireson, R. E. Chandler, E. J. Kendon, M. Widmann, S. Brienen, H. W. Rust, T. Sauter, M. Themessl, V. K. C. Venema, K. P. Chun, C. M. Goodess, R. G. Jones, C. Onof, M. Vrac, and I. Thiele-Eich (2010), Precipitation downscaling under climate change: Recent developments to bridge the gap between dynamical models and the end user, *Rev. Geophys.* 48, RG3003, doi:10.1029/2009RG000314.

- McFarlane, N. A., G. J. Boer, J. P. Blanchet, and M. Lazare (1992), The Canadian climate centre second generation circulation model and its equilibrium climate, *J. Clim.*, *5*, 1013–1044.
- Mearns, L. O., F. Giorgi, L. McDaniel and C. Shields (1995), Analysis of daily variability of precipitation in a nested regional climate model: comparison with observations and doubled CO<sub>2</sub> results, *Glob. & Planet. Change*, *10*, 55–78.
- Min, Y.-M., V. N. Kryjov and C.-K. Park (2009), A probabilistic multimodel ensemble approach to seasonal prediction, *Wea. Forecasting*, *24*, 812–828.
- Murakami, T. and J. Matsumoto (1994), Summer monsoon over the Asian continent and western North Pacific, *J. Meteorol. Soc. Jpn.* *72*, 719–745.
- Niu, N. and J. Li (2008), Interannual variability of autumn precipitation over South China and its relation to atmospheric circulation and SST anomalies, *Adv. Atmos. Sci.*, *25*, *1*, 117–125.
- Park, H., B. K. Park, D. K. Rha, and J. Y. Cho (2002), An improvement of global model in 2001, *KMA/NWPD Tech. Rep.*, 2002–1, (in Korean).
- Peixoto, J. P. and A. H. Oort (1991), Physics of climate, *AIP press. New York, NY*, 275–275.
- Ritchie, H. (1991), Application of the semi-Lagrangian method to a multilevel spectral primitive-equations model, *Q. J. R. Meteorol. Soc.*, *117*, 91–106.
- Rowell, D. P. (1998), Assessing potential seasonal predictability with an ensemble of multidecadal GCM simulations, *J. Clim.*, *11*, 109–120.

- Saha, S., S. Nadiga, C. Thiaw, and Coauthors (2006), The NCEP climate forecast system, *J. Clim.*, *19*, 3483–3517.
- Saji, N. H., B. N. Goswami, P. N. Vinayachandran and T. Yamagata (1999), A dipole mode in the tropical Indian Ocean. *Nature*, *401*, 360–363.
- Saji, N.H. and T. Yamagata (2003), Possible impacts of Indian Ocean dipole mode events on global climate. *Clim. Res.*, *25*, 151–169.
- Scinocca, J. F., N. A. Mcfarlane, M. Lazare, J. Li, and D. Plummer (2008), The CCCma third generation AGCM and its extension into the middle atmosphere, *Atmos. Chem. and Phys.*, *8*, 7055–7074.
- Shafer, P. E. and H. E. Fuelberg (2008), A perfect prognosis scheme for forecasting warm-season lightning over Florida, *Mon. Wea. Rev.*, *136*, *6*, 1817–1846.
- Shukla, J. and J. L. Kinter III (2006), Predictability of seasonal climate variations: a pedagogical review, In T. Palmer and R. Hagedorn (Ed.), *Predictability of weather and climate*, 306–341, N.Y., Cambridge University Press.
- Sohn, S.-J., C.-Y. Tam and C.-K. Park (2011), Leading modes of East Asian winter climate variability and their predictability: an assessment of the APCC multi-model ensemble, *J. Meteorol. Soc. Jpn.*, *89*, *5*, 455–474, doi:10.2151/jmsj.2011–504.
- Stidd, C. K. (1967), The use of eigenvectors for climatic Estimates, *J. Appl. Meteor.*, *6*, 255–264.
- Sun, J. Q. and J. B. Ahn, (2011), A GCM-based forecasting model for the landfall of tropical cyclones in China. *Adv. Atmos. Sci.*, *28*, 1049–1055.

- Thompson, D. W. J. and J. M. Wallace (1998), The Arctic oscillation signature in the wintertime geopotential height and temperature fields,
- Thompson, D. W. J. and J. M. Wallace (2000), Angular modes in the extratropical circulation, part I: Month-to-month variability, *J. Clim.*, *13*, 1000–1016.
- Tippett, M. K., T. Delsole, S. J. Mason, and A. G. Barnston (2008), Regression-based methods for finding coupled patterns, *J. Clim.*, *21*, 4384–4398.
- Trenberth, K. E. (1997), The definition of El Nino, *Bull. Amer. Meteor. Soc.*, *78*, 2771–2777.
- Tung, Y.-L., C.-Y. Tam, S.-J. Sohn and J.-L. Chu (2013), Improving the seasonal forecast for summertime South China rainfall using statistical downscaling, *J. Geophys. Res. (in press)*.
- Wang, B. (1995), Interdecadal changes in El Nino onset in the last four decades, *J. Clim.*, *8*, 267–285.
- Wang, B., R. Wu, and K.-M. Lau (2001), Interannual variability of the Asian summer monsoon: contrasts between the Indian and the west north Pacific-east Asian monsoons, *J. Clim.*, *14*, 4073–4090.
- Wang, B. and L. Ho (2002), Rainy season of the Asian-Pacific summer monsoon, *J. Clim.*, *15*, 386–398.
- Wang, G.-C. and Z.-Y. Guan (2007), Modes of air-sea interactions in the Indian Ocean and their relationships with the rainfall over China as revealed by SVD analysis, *J. Nanjing Ins. Meteor.*, *30*, *1*, 63–71 (in Chinese).

- Wetterhall, F., S. Halldin, and C.-Y. Xu (2005), Statistical precipitation downscaling in central Sweden with the analogue method, *J. Hydrology*, *306*, 1–4, 174–190.
- Widmann, M. (2005), One-dimensional CCA and SVD, and their relationship to regression maps, *J. Clim.*, *18*, 2785–2792.
- Widmann, M., C. S. Bretherton, and P. Salathé Eric (2003), Statistical Precipitation Downscaling over the Northwestern United States Using Numerically Simulated Precipitation as a Predictor. *J. Clim.*, *16*, 799–816.
- Wilby, R. L., and T.M. Wigley (1997), Downscaling general circulation model: a review of methods and limitations, *Prog. Phys. Geography*, *21*, 4, 530–548.
- Wilby, R. L., T.M. Wigley, D. Conway, P. D. Jones, B.C. Hewitson, J. Main, and D. S. Wilks (1998), Statistical downscaling of general circulation model output: A comparison of methods, *Water Resources Res.*, *34*, 2295–3008.
- Wilby, R. L., S. P. Charles, E. Zorita, B. Timbal, P. Whetton, and L.O. Mearns (2004), Guidelines for use of climate scenarios developed from statistical downscaling methods, *Supporting material of the Intergovernmental Panel on Climate Change, available from the DDC of IPCC TGCIA*, 27.
- Wilks, D. S. (1995), Statistical methods in the atmospheric sciences, *Academic Press, San Diego, CA*, 467.
- Williams, P. (1961), An experiment in the use of “perfect” prognostic charts, *Mon. Wea. Rev.*, *88*, 219–222.

WMO (2002), Standardized verification system (SVS) for long-range forecasts (LRF), *Manual on the GDPS, WMO-No. 485*, 1.

Xiao, Z.-N., H.-M. Yan and C.-Y. Li (2002), The relationship between Indian Ocean dipole index and the precipitation and temperature over China, *J. Trop. Meteor.*, 18, 4, 335–344. (in Chinese).

Yang, S., Z.-Q. Zhang, V. Kousky, R. W. Higgins, S.-H. Yoo, J.-Y. Liang, A.-Y. Fan (2008), Simulations and seasonal prediction of the Asian summer monsoon in the NCEP climate forecast system, *J. Clim.*, 21, 3755–3775.

Ye, H. and T. Lu (2012), Dominant patterns of summer rainfall anomalies in East China during 1951-2006, *Adv. Atmos. Sci.*, 29, 4, 695–704.

Zhang, R.-H., A. Sumi and M. Kimoto (1996), Impact of El Nino one the East Asian monsoon: a diagnostic study of the “86/87” and “91/92” events. *J. Meteor. Soc. Jpn.*, 74, 49–62.

Zhang, R.-H., A. Sumi and M. Kimoto (1999), A diagnostic study of the impact of El Nino on the precipitation in China, *Adv. Atmos. Sci.*, 16, 2, 229–241.

Zhong, A., H. H. Hendon, and O. Alves (2005), Indian Ocean variability and its association with ENSO in a global coupled model, *J. Clim.*, 18, 3634–3649.

Zhu, C., C.-K. Park, W.-S. Lee, and W.-T. Yu (2008), Statistical Downscaling for multi-model ensemble prediction of summer monsoon rainfall in the Asia-Pacific region using geopotential height field, *Adv. Atmos. Sci.*, 25, 867–884.

Zorita, E., and H. von Storch (1999), The Analog Method as a Simple Statistical Downscaling Technique: Comparison with More Complicated Methods.  
*J. Clim.*, 12, 2474–2489.